HIGH-PRECISION MASS MEASUREMENT OF ^{24}SI AND THE DEVELOPMENT OF A COLLISION-INDUCED DISSOCIATION GAS CELL

By

Daniel Jesus Puentes

A DISSERTATION

Submitted to
Michigan State University
in partial fulfillment of the requirements
for the degree of

Physics - Doctor of Philosophy

2023

ABSTRACT

HIGH-PRECISION MASS MEASUREMENT OF ^{24}SI AND THE DEVELOPMENT OF A COLLISION-INDUCED DISSOCIATION GAS CELL

By

Daniel Jesus Puentes

Nuclear masses have been studied for over a century, with critical data providing important constraints in nuclear physics studies. Penning trap mass spectrometry (PTMS) is one of the most precise methods for measuring the masses of exotic nuclei at rare isotope facilities. PTMS is performed at Michigan State University's National Superconducting Cyclotron Laboratory (NSCL) at the Low Energy Beam and Ion Trap (LEBIT) facility, where both stable and rare isotope masses have been measured to high precision. The aim of this work was to measure the mass of ^{24}Si and investigate the impact of this mass on the competition between the rapid proton capture and αp capture at the ^{22}Mg waiting point.

These two nucleosynthetic processes take place on the surface of neutron stars in a binary system with another star when a critical point is reached during accretion of H/He-rich material from the companion star. An explosion will occur triggering a thermonuclear runaway where the two processes are initiated accompanied Type-I X-ray burst. The X-ray burst is the only observable, so nuclear physics data is needed to constrain observational data such as reaction rates for these nucleosynthetic processes. Variations within the uncertainty of the ^{23}Al$(p,\gamma)^{24}$Si reaction rate lead to significant shifts in simulated x-ray light curves, where the ground state mass of ^{24}Si is currently the dominant source of the reaction rate uncertainty (19 keV). The Penning trap measurement performed at LEBIT improved the mass uncertainty of ^{24}Si by a factor of 5 more precise than previous results. The atomic mass excess of ^{24}Si, 10 753.8(37) keV, substantially reduces the uncertainty of the ^{23}Al$(p,\gamma)^{24}$Si reaction

rate, which constrains the onset temperature of the (α, p) process at the ^{22}Mg waiting-point to a precision of 9%.

A key process needed to perform this measurement is stopping the beam in a gas stopper before extracting and injecting into a Penning trap to perform the measurement. An issue with stopped beam experiments is rare isotopes are often extracted as a molecule as well as the presence of contaminant molecules. The development of a gas catcher that would be used to perform collision-induced dissociation (CID) was pursued and investigated with a prototype CID gas catcher (CIDGC). The entrance membrane for the CIDGC is a 20 nm Si_3N_4 membrane with the gas catcher filled with ultrapure He at 2.5 mbar. Dissociated ions are extracted using an ion surfing technique facilitated by a circular RF carpet. The extracted ions are sent downstream using an RFQ ion guide and injected into a residual gas analyzer for analysis. The early results with online beam show that ions are successfully transported through the CIGDC, but no sign of ions delivered from the beam stopping facility were yet observed.

Esta obra está dedicada a mi esposa, mis padres, y el resto de mi familia, incluyendo mis abuelos que sacrificaron todo para llegar a los Estados Unidos y comenzar una nueva vida.

This work is dedicated to my wife, my parents and the rest of my family, including my grandparents who sacrificed everything to get to the United States and start a new life.

TABLE OF CONTENTS

LIST OF TABLES

LIST OF FIGURES

KEY TO SYMBOLS

Z Atomic Number
m_p Proton Mass
N Neutron Number
$B(A,Z)$ Nuclear Binding Energy
A Mass Number
c Speed of Light
Y_a Abundance of Initial Nucleus
Y_{a+1} Abundance of Final Nucleus
S_p Proton Separation Energy
Q Q-value reaction
k Boltzmann Constant
T Temperature
m_a Mass of Initial Nucleus
m_{a+1} Mass of Final Nucleus
N_A Avogadro's Number
$N_A\langle\sigma v\rangle$ Reaction Rate
E_i Resonance Energy
T_9 Temperature in GK
E_x Excitation Energy
A/Q Mass to Charge Ratio
ω_c angular cyclotron frequency
π Pi
ν_c cyclotron frequency
q charge
B Magnetic Field Strength
m mass
z trap length
ρ_o trap radius
E Electric Field Strength
ω_z angular axial frequency
ω_- angular magnetron frequency
ω_+ angular reduced cyclotron frequency
ρ^z axial amplitude
ρ^- magnetron amplitude
ρ^+ reduced cyclotron amplitude
k_0 quadrupolar excitation amplitude
$\Delta\phi$ Difference in RF and Radial Phases
γ Apparatus-Specific Parameter
T_{RF} Excitation Time
N Total Number of Ions Detected
F_z Axial Force Ions Feel Leaving the Magnetic Field
μ Magnetic Dipole Moment
E_r Radial Energy of an Ion
B_0 Magnetic Field Strength in the trap
V_{RF} RF Excitation Amplitude
β^+ Beta$^+$ decay
σ Uncertainty
u Mass Unit
$\bar{R}$ Weighted Cyclotron Frequency Ratio
m_e Electron Mass
m_{ref} Reference Mass
m_{interest} Mass of interest
M_0 Projectile Mass
M_1 Target Mass
$\omega\gamma$ Resonance Strength
J Total Angular Momentum
l Orbital Angular Momentum
C^2S Spectroscopic Factor
Γ_γ Radiative Width
Γ_p Proton Width
$S(E_0)$ Astrophysical S-factor
λ_i Mass Flow Rate
W Weight Factor
X_i Mass Fraction
ρ density
n_q quantum concentration
n_p proton density
$\hbar$ Reduced Plank Constant
Ω Resistance
y Height above the RF carpet
E_p Electric Push Field
$V_{\mathrm{eff,max}}$ RF Repelling & Damping Potential
a RF Carpet Pitch
F_p Push Force
F_{RF} RF Force
U Direct Current Potential
V Quadrupole RF Potential
K_0 Reduced Mobility
L Distance Ions Travel
t_D Flight time
P Pressure

KEY TO ABBREVIATIONS

AME Atomic Mass Evaluation
NSCL National Superconducting Cyclotron Laboratory
rp Rapid Proton Capture
s Slow Neutron Capture
r Rapid Neutron Capture
νp Neutrino Capture
αp Alpha Capture
CID Collision-Induced Dissociation
ISOL Isotope Separation On-Line
LEBIT Low Energy Beam and Ion Trap
BECOLA BEam COoler and LAser spectroscopy
EBIT Electron-Beam Ion Trap
PTMS Penning Trap Mass Spectrometry
ANL Argonne National Laboratory
ACGS Advanced Cryogenic Gas Stopper
BMIS Batched Mode Ion Source
RF Radiofrequency
RFQ RF Quadrupole
CIDGC CID Gas Cell
FRIB Facility for Rare Isotope Beams
TOF-ICR Time-of-Flight Ion Cylotron Resonance
FT-ICR Fourier Transform Ion Cyclotron Resonance
PI-ICR Phase-Imaging Ion Cyclotron Resonance
FFT Fast Fourier Transform
MCP Microchannel Plate
RIB Rare Isotope Beam
CCF Coupled Cyclotron Facility
HV High-Voltage
DC Direct Current
BOB Beam Observation Box
NICER Neutron Star Interior Composition Explorer
SID Surface-Induced Dissociation
ETD Electron-Transfer Dissociation
TITAN TRIUMF's Ion Trap for Atomic and Nuclear Science
MR-TOF Multiple Reflection Time of Flight
Printed Circuit Board PCB
AFG Arbitrary Function Generator
HF High Frequency
RGA Residual Gas Analyzer
PEEK Polyether Ether Ketone
SRIM Stopping and Range of Ions in Matter
CEM Channel Electron Multiplier

Chapter 1

Introduction

Masses are one of the most fundamental properties in science and they are critical for different fields such as chemistry, biology and metrology. In nuclear physics, masses provide critical benchmarks for different areas of study such as nuclear astrophysics, nuclear structure, tests of fundamental symmetries. The mass of a nucleus is a measure of the binding energy of a nucleus, and can be defined as

$$M_{nucl} = Zm_p + Nm_n - B(A,Z)/c^2 \tag{1.1}$$

where M_{nucl} is the mass of the nucleus, Z is the number of protons, m_p is the proton mass, N is the number of neutrons, m_n is the neutron mass and $B(A,Z)$ is the nuclear binding energy. The evolution of the binding energy as a function and proton and neutron number has been investigated using mass spectrometry techniques, with significant progress made with exotic nuclei outside the valley of stability at radioactive beam facilities around the world. Figure 1.1 shows the mass uncertainty as a function of proton and neutron number across the chart of nuclides, with the mass information taken from the Atomic Mass Evaluation (AME) 2020 [8]. Rare isotopes are created at Michigan State University using the National Superconducting Cyclotron Laboratory (NSCL). The NSCL consists of two coupled cyclotrons that produce rare isotopes via projectile fragmentation. The isotopes are

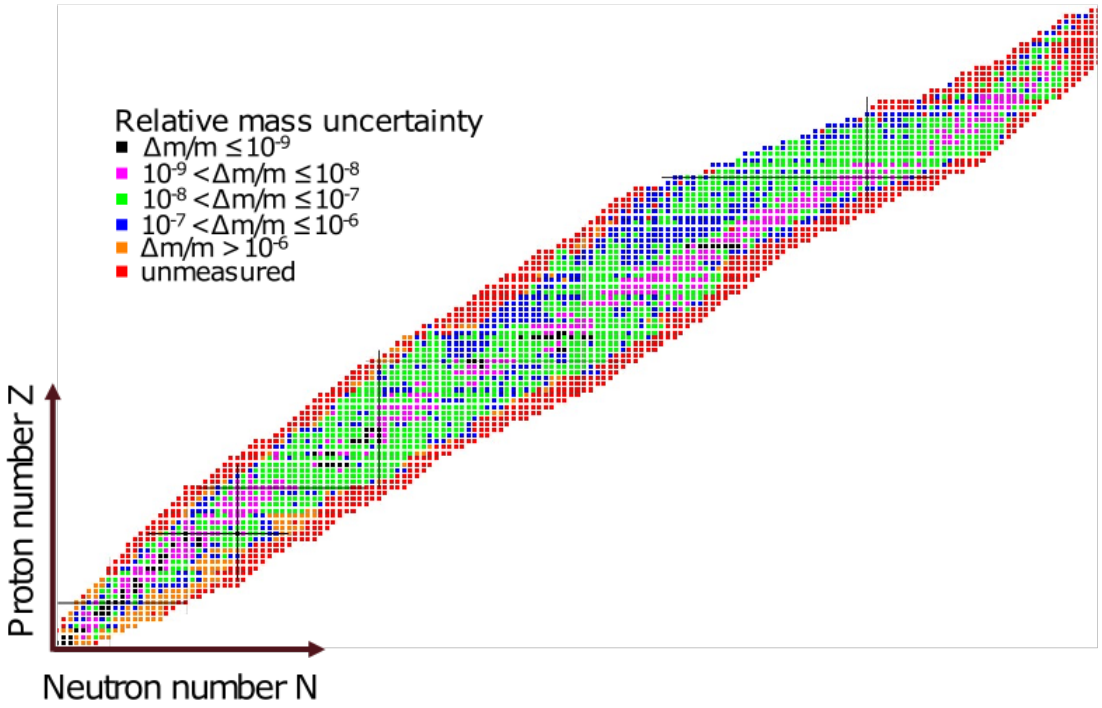

Figure 1.1: The chart of nuclides with mass uncertainties color coded. Information for the mass uncertainties was collected from the AME2020 [8]. The black lines represent magic numbers indicating shell closures for specific neutron and proton number.

then delivered to different experimental stations, where masses can be measured in a variety of ways. The NSCL is what allows researchers to probe the most exotic nuclei, and study their properties to answer questions like the evolution of elements in the universe.

1.1 Masses in Nuclear Astrophysics

Stellar environments can range from the cores of stars to explosive Type-1A supernovae. Several nucleosynthetic pathways have been theorized to explain the creation of elements in these stellar environments. A few pathways include the rapid proton (rp) capture process [30], slow neutron (s) capture process [31], the rapid neutron (r) capture process [32] and the νp-process [33]. Masses are important in nuclear astrophysics, and can have significant impacts on calculations for different astrophysical quantities. These calculations can suffer

from large mass uncertainties or unknown masses that can propagate into large uncertainty bands for the calculation of interest. One example is the role that masses play in determining abundance ratios [34] for two neighboring nuclei in isotopic/isotonic equilibrium,

$$\frac{Y_{a+1}}{Y_a} \propto e^{Sp/k_BT} \tag{1.2}$$

where Y_{a+1} and Y_a are the abundances of the initial (a) and final $(a+1)$ nuclei, S_p is the proton separation energy, k_B is the Boltzmann constant and T is the temperature. The proton energy is also the Q value of the reaction, but opposite in magnitude, as defined as

$$S_p = -Q = -(m_a + m_p - m_{a+1})c^2. \tag{1.3}$$

The reaction Q value is also the difference in binding energies of the parent and daughter nucleus, which in this case is a (p, γ) reaction. Another important astrophysics quantity of interest for developing pathway networks are reaction rates. Reaction rates calculations depend on a several factors including what type of reaction is happening (charged particle versus a neutral partical reaction) as well as whether the reaction a nonresonant (direct) or resonant reaction [35]. The size of the resonance can also impact the calculation, and make certain approximations necessary. The direction of the reaction will also guide how a reaction is calculated, such as a forward capture reaction of a photodisintegration [36]. In the resonance approximation, the reaction rate is,

$$N_A\langle\sigma v\rangle_r \propto \sum_i e^{-11.605E_i/T_9} \tag{1.4}$$

where all resonances in a reaction are considered based on E_i. The resonance energy E_i is simply the difference between the excitation energy E_x in an unbound state in the final nucleus and the reaction Q value,

$$E_i = E_x - Q. \tag{1.5}$$

These reaction rates can be used to calculate the competition of mass flows during specific points in a nucleosynthetic pathway. These critical points are located near nuclei with long effective half-lives relative to an astrophysical process in question, known as waiting point nuclei [37–40]. Sometimes, astrophysical events happen quicker than the β decay of a nucleus in a process chain, and requires other means to bypass this waiting point nucleus. A firm understanding of the competition between these bypassing pathways can provide more stringent constraints to different astrophysical models.

One of the models uses nuclear information paired with observational data to simulate Type-I X-ray bursts [41]. These astrophysical events take place when enough hydrogen-rich material accretes onto the surface of a neutron star in a binary star system. Precise nuclear information can be used to constrain the shape of these light curves, such as the pathway of the *rp* process. Nuclei related to Urca cooling [42] also provide information about Type-I X-ray bursts, and need nuclear physics information such as masses to understand the activities related to neutron star crusts and the reactions that take place within them. Urca cooling is thought to be one of the pathways responsible for the liberation of heat off of the neutron star surface via neutrinos. The focus of this dissertation will examine the impact of the ^{22}Mg waiting point on the *rp* and αp-process. The first direct mass measurement of ^{24}Si provides a constraint to understanding the competition between these two nucleosynthetic pathways at the $A = 22$ waiting point. .

1.2 Need for Collision-Induced Dissociation (CID) for Precision Measurements

The stopping of fast beams produced by projectile fragmentation is a key factor in performing laser spectroscopy, mass measurements, and reacceleration at the NSCL, which were originally the domain of ISOL facilities where the rare isotopes are produced at low energies. At the NSCL, stopped rare isotope beams are delivered to three different areas: Low Energy Beam and Ion Trap (LEBIT), BEam COoler and LAser spectroscopy (BECOLA) facility [43], and the electron-beam ion trap (EBIT) prior to injection into the reaccelerator [44]. These facilities have been used for a succcessful science program. However, sometimes it can be difficult to perform experiments at these areas if the ion of interest comes as a molecule or if the ion arrives accompanied by large amounts of stable or radioactive contamination. The formation of molecular ions and other contaminant ions results of low-level gas residuals, oil from pumps and surface outgassing with He-filled gas cells that are responsible for the stopped beams [45]. Sometimes the contamination can be so concentrated that contaminants will completely saturate the signal of interest. The formation of radioactive molecular ions can also lower the efficiency of measurements since ions can arrive at different A/Q values, some of which are lost when passing through a magnetic mass separator.

Contaminant ions have been identified using Penning trap mass spectrometry (PTMS). Some common contaminants that have been identified several times during mass measurement campaigns include CO_2, O_2, NO, and H_2O. During mass measurement campaigns, several ions produced during projectile fragmentation can come attached with hydrocarbons and or oxygen atoms. The A/Q range of masses has been measured from $A/Q = 6-114$ from beams created by the ANL gas cell [46], the Advanced Cryogenic Gas Stopper (ACGS) [47]

and the Batched Mode Ion Source (BMIS) [48]. The contaminants from these sources have been catalogued and are shown in Fig. 1.2.

Different solutions have been pursued to mitigate this issue. One of them is through the use of collision-induced dissociation (CID). CID is one of many techniques used in fields such as chemistry to dissociate molecular ions through converting their kinetic energy into internal energy [49,50]. At the NSCL, CID has been implemented in the beam stoping facility, where a potential bias offset is generated between the gas catcher and the extraction radiofrequency (RF) quadrupole (RFQ) ion guide [46, 51]. The collisions between the buffer gas and the molecular ions during extraction have shown to break up weakly bound molecules. Ions of interest have also shown to be extracted out with a higher charge state as well. Another location at the NSCL that CID can be implemented is using the RFQ cooler buncher in LEBIT as a winowless gas cell before injection into the Penning trap [52]. This technique motivated an effort to develop a gas catcher dedicated to performing CID following the beam stopping facility. The successful creation of a prototype device can be used as motivation to scale to CID gas catcher (CIDGC) that can be used in the future Facility for Rare Isotope Beams (FRIB).

A discussion of PTMS used at the LEBIT facility in the NSCL will be provided in chapter 2. Chapter 3 will focus on a high-precision mass measurement of ^{24}Si, which has led to a refined determination of the *rp*-process near the $A = 22$ waiting point. This mass measurement provides a necessary anchor for performing X-ray burst light curve modeling. The development of the prototype CIDGC being pursued at the NSCL will be explored in Chapter 4, and finally, chapter 5 will investigate on-line beam measurements that show CID with molecules that were identified in LEBIT using PTMS prior to delivery to the CIDGC.

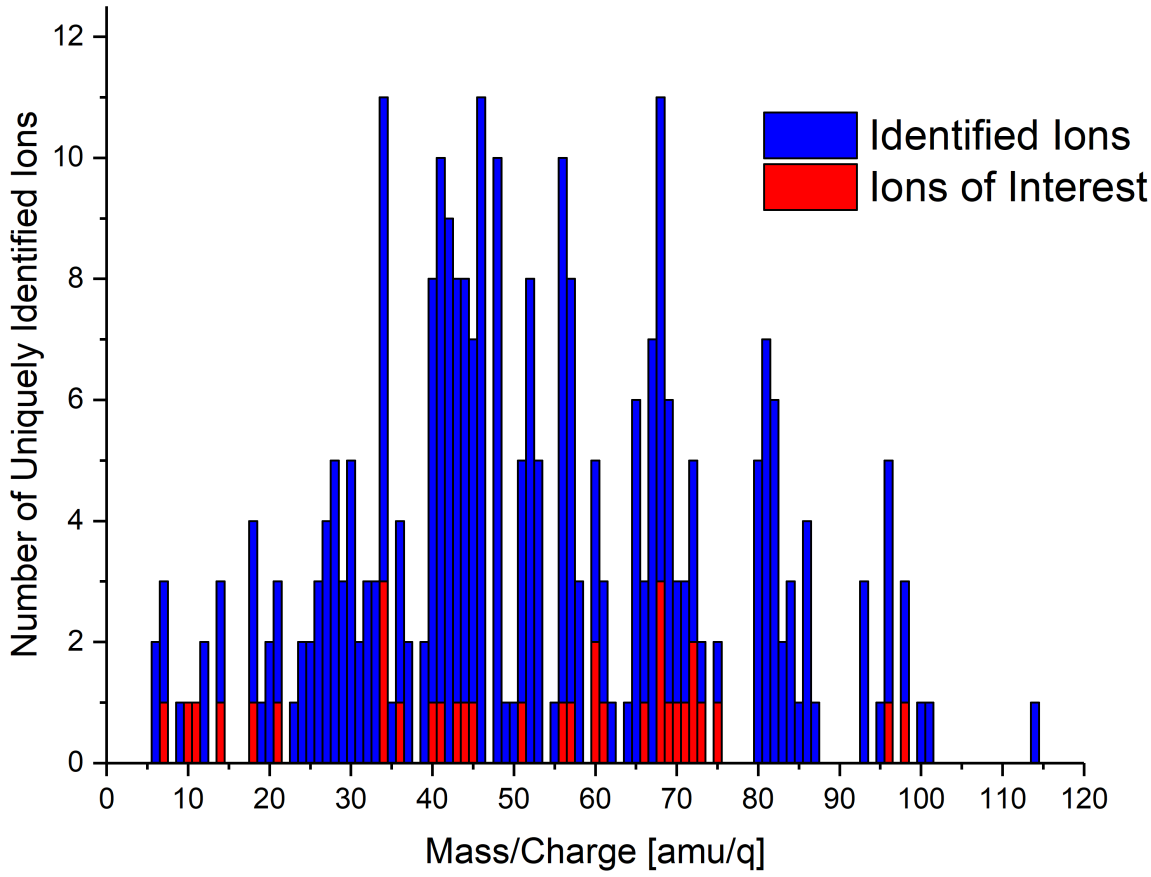

Figure 1.2: A hisotgram of ions that have been identified using PTMS after the LEBIT facility was recommissioned with beam from the beam stop facility in 2013 [9]. Ions of interest often came either as a bare isotope or a molecular ion, either singly or doubly charged. The red represents the ions that were measured and published via References [4, 10–22]. The histogram illustrates the potentially damaging impact contaminant ions can have during precision measurement campaigns.

Chapter 2

Penning Trap Mass Spectrometry and the LEBIT Mass Spectrometer Facility at NSCL

2.1 Penning Trap Basic Concepts

Penning traps were developed for several applications such as quantum information processing, optical spectroscopy and microwave frequency standard clocks [53]. However, they follow the same basic principles. Ions are confined axially via a quadrupolar electrostatic and radially by a uniform, solenoidal magnetic field oriented along the trap axis. These two fields result in the 3D confinement of charged particles in the trap. Charged particles in a magnetic field will undergo cyclotron motion. The frequency of that motion is related by

$$\omega_c = 2\pi\nu_c = \frac{qB}{m}, \tag{2.1}$$

where ω_c is the true cyclotron frequency of an ion, B is the magnetic field strength and q is the charge of an ion. Two types of electrode geometries are typically used for Penning traps: cylindrical and hyperbolic. At LEBIT, the hyperbolic configuration is chosen to minimize

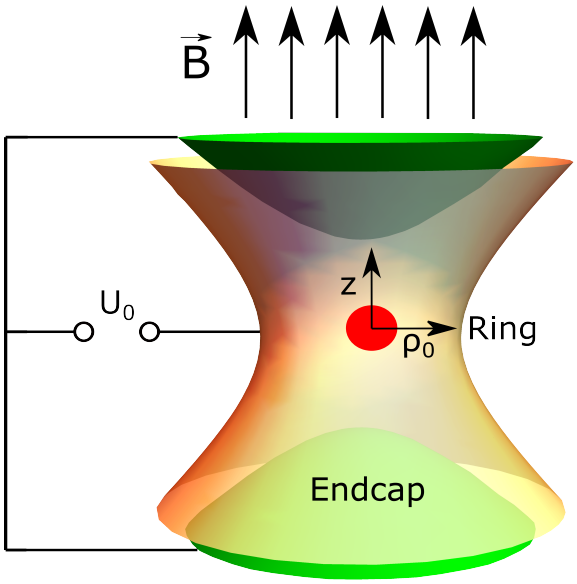

Figure 2.1: Illustration of a hyperbolic trap used at LEBIT. The uniform magnetic field is shown, as well as the three electrodes used to generate quadrupolar electric potential. The trap radius is defined by ρ_o, and z is the trap length.

higher-order electric-field contributions for ions at larger radii that need to be accounted for using the cylindrical open-ended configuration [54].

A 9.4 T superconducting magnet from Cryomagnetics houses the LEBIT Penning trap. An electrostatic field is generated by three hyperbolic trap electrodes, which consist of the ring electrode at the center of the trap and endcap electrodes on either side of the trap. In addition, there are two sets of correction electrodes to compensate for the fact that the main hyperbolic electrodes are truncated and that the endcaps have holes for ion injection and ejection. Analytical solutions exist for ion motion inside a Penning Trap [55–57]. The motion of stored ions in a trap can be decomposed into three eigenmotions: magnetron motion, axial motion and reduced cyclotron motion. An illustration of the three motions can be found in Fig. 2.2. The axial motion will undergo harmonic oscillation parallel to the magnetic field. The electrostatic field splits the true cyclotron motion into two radial motions: a slow $E \times B$ drift called magnetron motion and a faster, modified cyclotron motion.Each motion has a

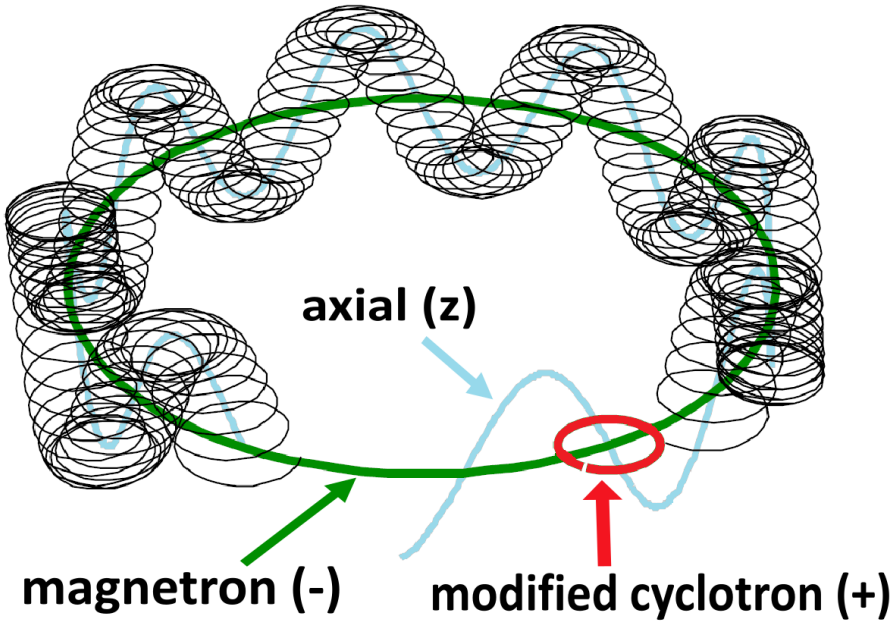

Figure 2.2: The three eigenmotions observed in an ideal trap.

characteristic frequency and amplitude. The true cyclotron frequency of an ion is related to all three eigenfrequencies by the following relation [57]

$$\omega_c = \sqrt{\omega_z^2 + \omega_-^2 + \omega_+^2}, \tag{2.2}$$

where ω_- is the magnetron frequency, ω_+ is the reduced cyclotron frequency, and ω_z is the axial frequency. Similarly, the amplitudes of the motions are given by ρ_-, ρ_+, and ρ_z. The sum of the magnetron (ω_-) and reduced cyclotron frequencies ($\omega+$) can be approximated by

$$\omega_c = \omega_- + \omega_+. \tag{2.3}$$

Azimuthal, multipolar electric RF fields are generated by applying RF signals to the segmented ring electrode in a trap [23] and can be used to manipulate ion motion. For contaminant ions, an RF dipolar excitation [23, 58] will be applied 180° out of phase of each

other between opposite halves of the segmented ring. In a radial dipolar excitation, one of the radial amplitudes, ρ^+ or ρ^-, can be driven until the ion is effectively removed from the trap. This excitation is typically used on contaminant ions, which are excited at ω_+ since it's strongly mass dependent. The other primary radial excitation is the quadrupolar excitation [54, 57]. Quadrupolar excitations at an ion's cyclotron frequency cause a periodic beating between the magnetron motion and reduced cyclotron motion, according to

$$\rho^{\pm}(t) = \rho^{\pm}(0)\cos\left(\frac{k_0}{2}t\right) \mp \rho^{\mp}(0)e^{\pm i\Delta\phi}\sin\left(\frac{k_0}{2}t\right). \tag{2.4}$$

This type of excitation is used for mass measurements using PTMS with LEBIT.

2.2 Penning Trap Mass Spectrometry

Penning traps currently provide one of the best techniques for performing high-precision mass measurement techniques using charged particles. PTMS takes advantage of measuring the cyclotron frequency of ions in controlled and confined environments. This high-precision technique takes advantage of the relations described in Eq. 2.3 and Eq. 2.2, where the mass can be determined by measuring these different frequencies. To perform the measurement, however, q and B must also be known. Cyclotron frequency measurements are performed using a reference ion known to higher precision than the ion of interest, through the ratio of their frequencies. The relative uncertainty attainable in Penning trap measurements is determined by

$$\frac{\delta m}{m} = \frac{\delta \nu_c}{\nu_c} = \frac{\gamma}{\nu_c T_{RF}\sqrt{N}}, \tag{2.5}$$

where γ is the apparatus-specific parameter, T_{RF} is the time for which an RF excitation is applied, and N is the total number of ions detected. γ has been experimentally determined to be 0.3 for standard excitation schemes [59].

Different techniques of PTMS have been developed over the years. This thesis makes use of the Time-of-Flight Ion Cyclotron Resonance (TOF-ICR) technique [56], which will be discussed in the following section. The other two methods are Fourier Transform Ion Cyclotron Resonance (FT-ICR) [60] and Phase-Imaging Ion Cyclotron Resonance (PI-ICR) [61]. All three methods are currently implemented at the LEBIT facility.

FT-ICR uses the image current produced by ions on the trap electrodes, which will look like an oscillatory signal of noise and signal currents [60]. The signal is transformed from the time-domain to produce a frequency spectrum via a Fast Fourier Transform (FFT) [62]. The signal can be fitted to determine the frequency of the ion of interest. At LEBIT, the Single Ion Penning Trap was developed to measure cyclotron frequencies of ions with low production cross sections [63] and uses narrowband FT-ICR to achieve a precision comparable to TOF-ICR [64].

PI-ICR uses the positions of ions on a position-sensitive microchannel plate (MCP) detector. The ions are ejected from a Penning trap, where their radial frequencies are determined based on the accumulated angular phase of an ion in the trap [61]. The benefit of PI-ICR is a more than ten-fold improvement in precision for the same number of ions used as compared to the TOF-ICR method. PI-ICR has recently been demonstrated at LEBIT and will be used in future experiments with beams from the FRIB.

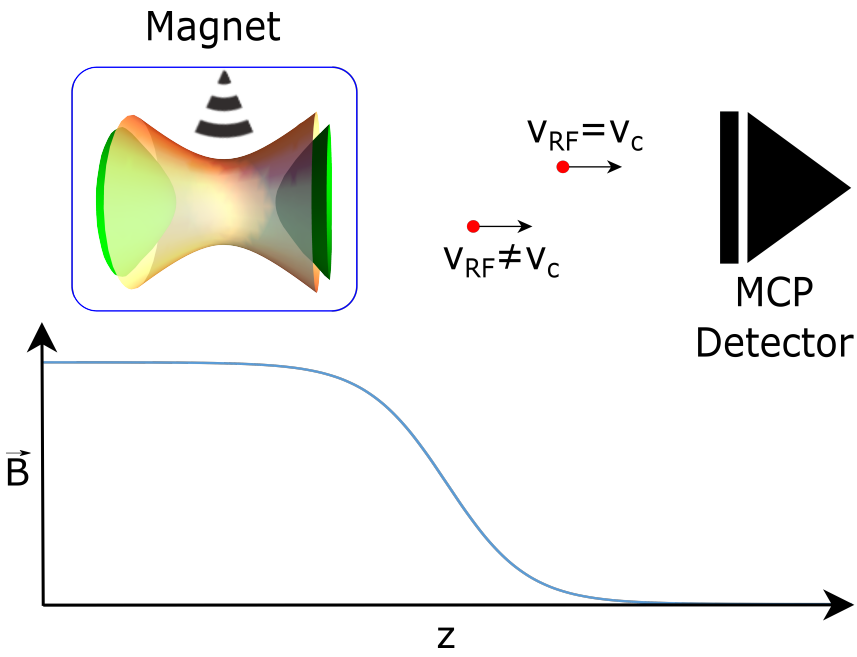

Figure 2.3: An illustration of the TOF-ICR measurement technique, which shows how the changing magnetic field can impact the radial energy ions gain during their TOF. When ions are excited at their cyclotron frequency, the TOF from the trap to the MCP detector is minimized.

2.3 TOF-ICR Technique

TOF-ICR has been the main technique for high-precision mass measurements with LEBIT. First, ions are injected into the trap off center using the Lorentz steerers, imparting an initial magnetron orbit [65]. Using a quadrupolar excitation, the slow magnetron motion is fully converted to reduced cyclotron motion to achieve the maximum gain in radial energy. After the conversion, the ions are ejected from the trap towards an MCP detector.

As the ions leave the trap, they will experience a force due to a changing magnetic field. Fig. 2.3 shows how the magnetic field strength changes as the ions move from the trap toward the MCP. The force that ions experience moving through this negative field gradient is

$$F_z = -\mu \left(\frac{\partial \vec{B}}{\partial z} \right) = -\frac{E_r}{B_0} \left(\frac{\partial \vec{B}}{\partial z} \right) \tag{2.6}$$

where μ is the magnetic dipole moment of the ion, E_r is the radial energy of the ion and B_0 is the magnetic field strength in the trap. The axial force causes ions with greater radial energy to reach the MCP in less time, translating into a reduction in the ion's measured TOF.

During a quadrupolar excitation, the magnetron motion converts to reduced cyclotron motion and back to magnetron motion in a periodic beating pattern. The RF amplitude V_{RF} and excitation time T_{RF} are tuned to achieve a complete conversion. The applied quadrupolar RF signal is then scanned around the expected cyclotron frequency of the ion of interest. This scan produces a TOF resonance curve, where the minimum at the cyclotron frequency of an ion. An example of such a resonance curve can be found in Fig. 2.4. The width of the measured resonance is proportional to $1/T_{\mathrm{RF}}$, which can be increased based on the scaling factor, $V_{\mathrm{RF}} \cdot T_{\mathrm{RF}}$. The longer the T_{RF}, the narrower the line width and the higher the precision achieved. The length of T_{RF} is limited by the half-life of the isotope, the initial mass uncertainty, and interaction with residual gases in the trap. Since the magnetic field strength decays over time, it's necessary to take a reference measurement before and after measuring the cyclotron frequency for the ion of interest. The magnetic field can then be interpolated to high precision for the ion of interest.

2.4 The National Superconducting Cyclotron Laboratory

The National Superconducting Cyclotron Laboratory (NSCL) is one of the premier facilities in the world for producing rare isotope beams (RIBs). Research performed at the NSCL has led to the discovery of new proton- and neutron-rich isotopes and a deeper understanding

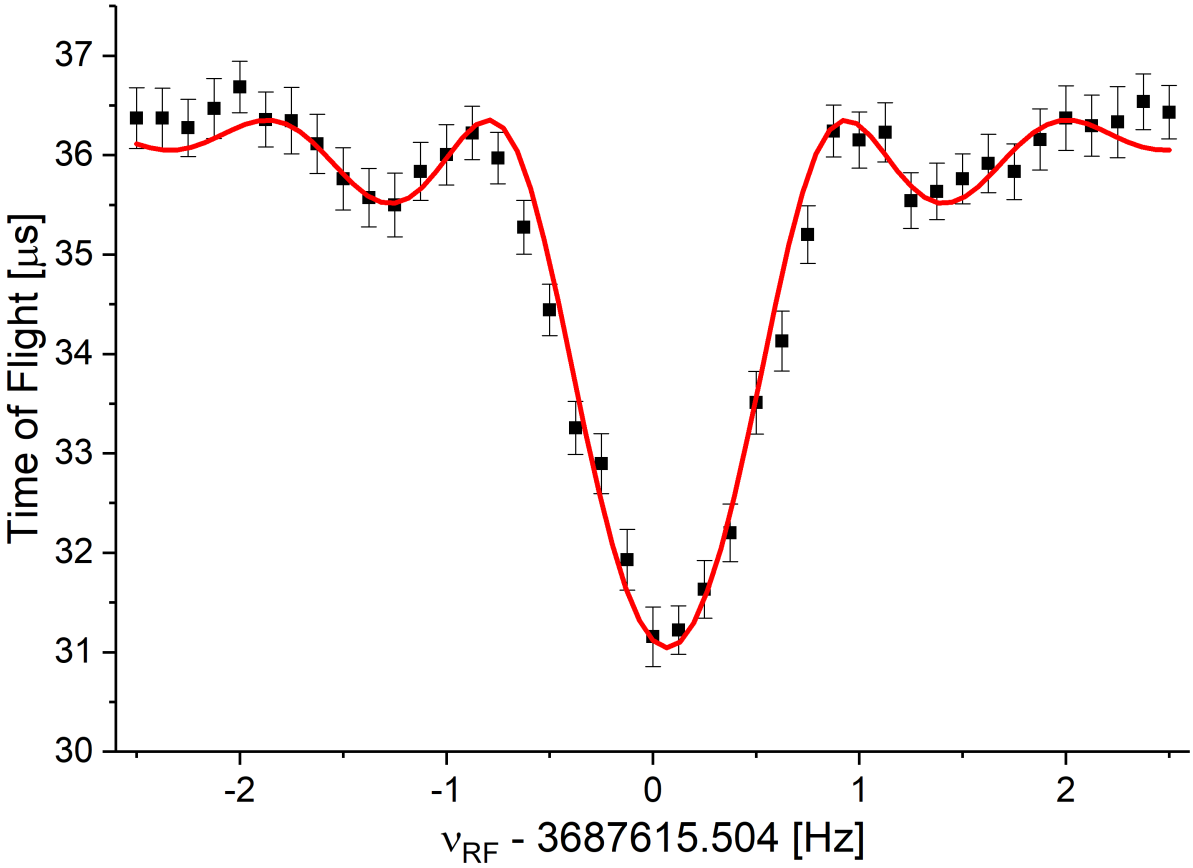

Figure 2.4: An example of a TOF response curve for a 1 s RF quadrupolar excitation of ^{39}K, with a fit to the line shape described in Ref. [23]. The minimum in the TOF provides a measurement of the cyclotron frequency of the ion.

of nuclear ground state properties such as beta decay, the evolution of nuclear structure and the role isotopes play in nuclear astrophysics [66]. The beams are then purified and stopped before delivering the beams to the LEBIT facility. The following subsections provide an overview of rare isotope production, delivery and how the LEBIT facility operates.

2.4.1 Rare isotope beam production

The primary beams, consisting of highly charged stable ions, are produced using electron-cyclotron resonance ion sources [67, 68]. The ions are accelerated to energies on the order

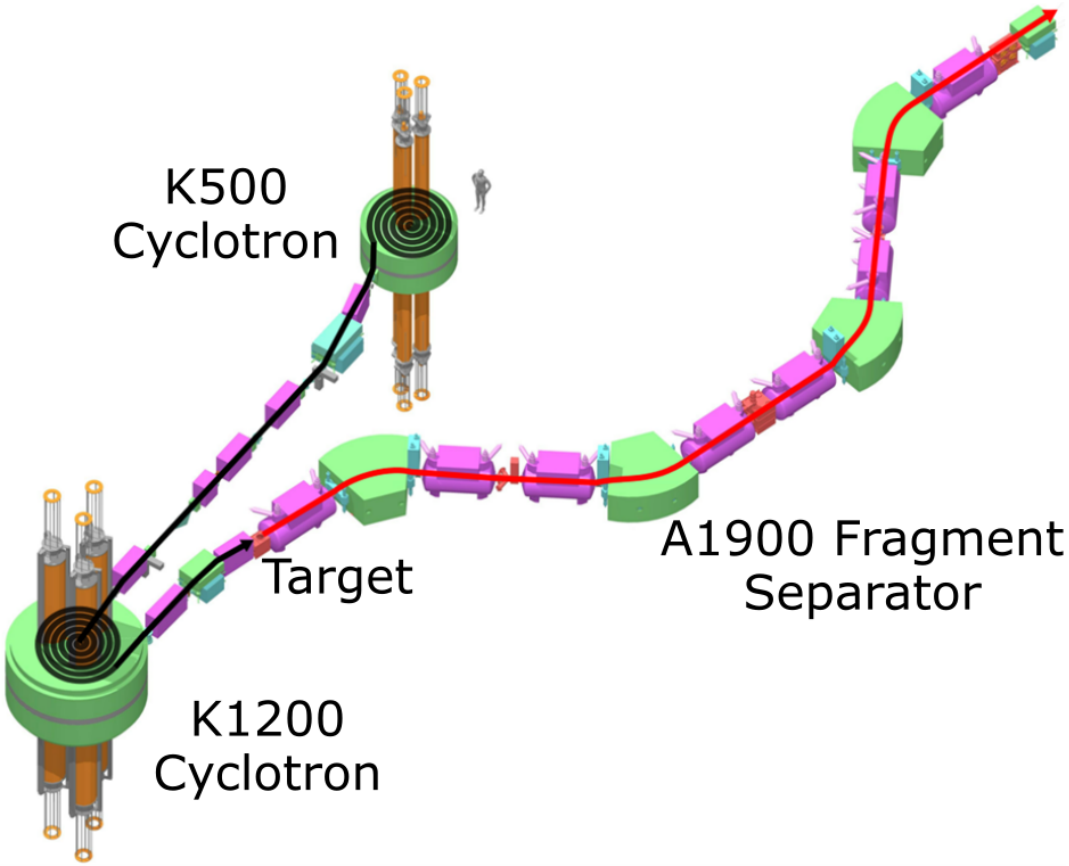

Figure 2.5: A diagram of the coupled cyclotron facility at the National Superconducting Cyclotron Laboratory, which shows the K500 and K1200 cyclotrons followed by the target. Then, the A1900 Fragment separator performs in-flight isotope purification and delivers fast rare isotope beams.

of 100 MeV/nucleon in the coupled cyclotron facility (CCF), which consists of the K1200 and K500 cyclotrons. Following the cyclotrons, the ions impinge on a thin beryllium target where rare isotopes are produced via projectile fragmentation.

The fragments are then separated in the A1900 Fragment Separator [69], where the beam is purified through two dispersive beamline sections separated by an energy-degrading wedge. An overview of the NSCL fast beam production site can be found in Fig. 2.5. The purification is based on the momentum change of the highly charged ions after passing through the degrader through the ion's magnetic rigidity. The combination of projectile fragmentation and in-flight isotope separation creates desirable high-intensity RIBs.

2.4.2 Low-energy beams from Beam Stopping Facility

For precision measurements with a Penning trap, the fast beams from the A1900 Fragment Separator must be converted to low-energy beams. This is achieved with the beam stopping facility, where currently two beam stopping devices are available, the ANL Gas Stopper [46] and the ACGS [47]. The RIBs are injected into the beam stopping devices after passing through Al degraders at an energy of approximately 1 MeV/nucleon. Both beam stoppers sit on a high-voltage (HV) platform, which defines the energy of the extracted beam.

Both gas stoppers operate on the same principle: ions are stopped by high-pressure Helium gas and transported along the length of the device using a combination of DC and RF guiding fields to an extraction point at the end of the system. A small orifice is located at the exit of the gas stopper where gas flow carries the ions through the orifice and into an RFQ system that confines the ions and provides differential pumping to return to an ultra-high vacuum for ion transport. An adjustable potential difference between the gas stopper and RFQ can be used to accelerate ions and break up molecular ions as a first stage of beam

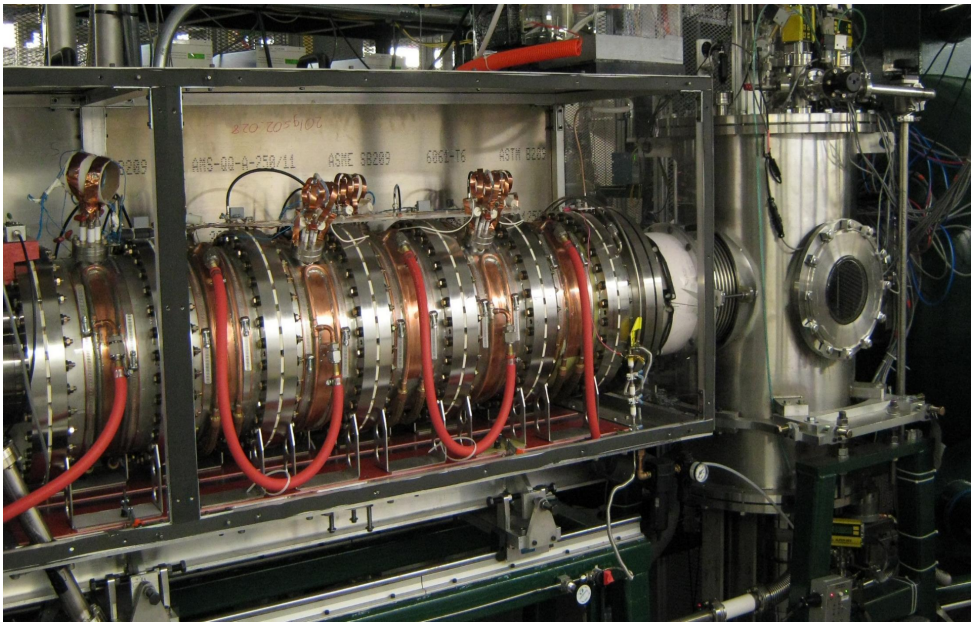

(a) The ANL Gas Stopper that was developed to facilitate beam stopping before delivery for precision measurements. The gas stopper was developed at Argonne National Laboratory (ANL).

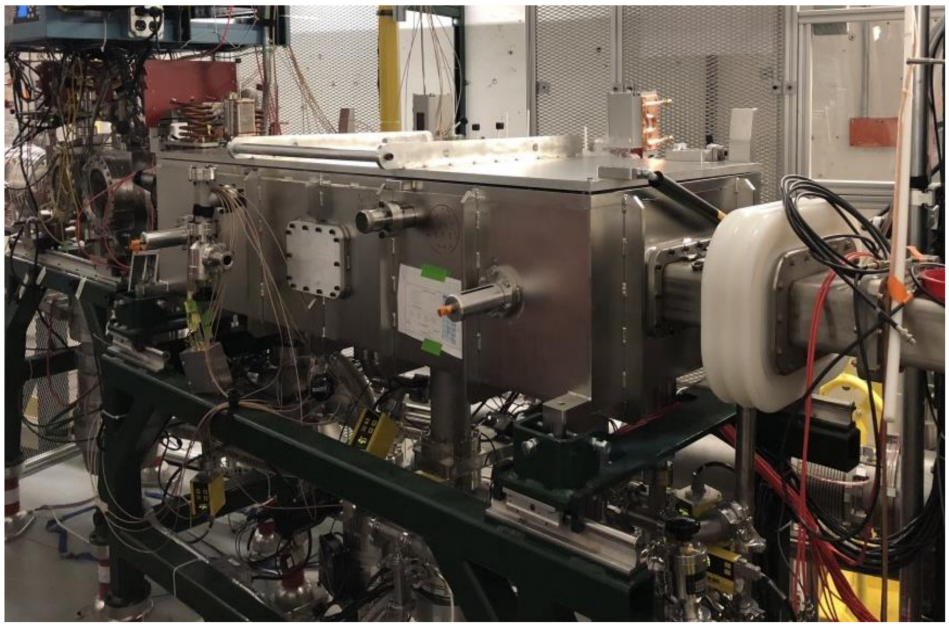

(b) The Advanced Cryogenic Gas Stopper (ACGS) that was developed to mitigate the contamination issues and increase the maximum ion throughput compared to the ANL Gas Stopper.

Figure 2.6: Photos of the ANL Gas Stopper and the Advanced Cryogenic Gas Stopper (ACGS) located in the beam stopping facility.

purification using CID. After transport through the RFQ system, the ions are accelerated to about 30 keV/Q and further purified using a magnetic dipole mass separator. The resolving power of the dipole mass separator is ≈ 1500. Finally, the rare-isotope beam is delivered to LEBIT.

2.5 Major Components of the LEBIT Facility

The LEBIT facility sits on an HV platform that shares a common power supply with the beam stopping facility. The beam energy can be fine-tuned with a separate DC HV source. In the LEBIT facility, two stable-beam ion sources are available for preparing the facility for online measurements: a Colutron plasma ion source and a laser ablation ion source [70]. After decelerating the ions, the beam is injected into the beam cooler/buncher for preparation into the Penning trap. Beam observation boxes (BOBs) exist along the LEBIT beamline for viewing the shape and location of the beam.

2.5.1 The Cooler/buncher

The cooler/buncher is a three-stage, gas-filled Paul trap [71] where the ions are injected from the beam stopping facility following deceleration. The ions are then converted from a continuous beam into pulsed beams. The first stage, the pre-cooler, uses a buffer gas to remove most of the ion energy and is guided by an axial DC field. The second stage is the μRFQ, serving as a differential pumping barrier. The third stage collects the ions and bunches them into ion pulses. The pressure in the final stage of the cooler/buncher is lower, by a factor of about 100 compared to the first stage, to minimize reheating of the ions during extraction.

2.5.2 The 9.4 T Penning Trap

After ejection from the cooler/buncher, ions pass through a TOF gate responsible for filtering out non-isobaric contaminants before entering the Penning trap [59]. Einzel lenses and injection optics are also optimized to inject ions into the Penning trap, which is housed inside the 9.4 T solenoid magnet. The Penning trap used at LEBIT and the superconducting solenoid magnet it is housed in are shown in Fig. 2.7.

The Penning trap consists of the elements described in Sec. 2.1. In addition to the endcaps and the ring electrodes, a correction ring and tube electrodes are also used to compensate for imperfections in the electrostatic field due to the truncated trap electrodes and holes in the endcap electrodes. When ions are injected into the trap, the upstream end cap potential is lowered and raised to capture the ions inside. After applying the RF quadrupole excitation via the ring electrodes, the downstream end cap potential is lowered and the ions are ejected toward the MCP detector to measure their TOF.

Figure 2.7: The Penning trap used at the LEBIT facility to perform high-precision cyclotron frequency measurements of rare isotopes. The Penning trap is housed in the 9.4 T superconducting solenoid magnet.

Chapter 3

Mass Measurement of ^{24}Si

The results for this chapter were published in Physical Review C as a Letter [4]. Some figures from the manuscript were altered from the manuscript for this document, and additional details are included.

3.1 Motivation for a mass measurement of ^{24}Si

3.1.1 Type-I X-ray Bursts

Type-I X-ray bursts occur at astrophysical sites consisting of a binary star system where a neutron star accretes H/He-rich matter from a companion star, leading to nuclear burning on the neutron star surface [34, 72]. As the temperature increases, the hot CNO cycle proceeds until the triple-α process is initiated with an ensuing thermonuclear runaway. The thermonuclear runaway explosion consists of multiple competing reaction sequences including the rapid proton (rp) [73] and (α, p) [74] processes. The rate at which the runaway occurs, as well as the reaction sequence competition, depends on factors such as accretion rate and fuel composition. The accretion cycle can last anywhere from several hours to days while the fuel is burned up in 10-100 s [75]. The only observable from these explosions, however, is the X-ray burst light curve, which can be recorded with telescopes like the *Neutron Star Interior Composition Explorer* (NICER) [76]. Future possible observables could include

measurements of spectroscopic signatures from X-ray bursts, which would provide insight into the ash composition of the small amounts of ejected material [77] and composition of the neutron star crust.

In addition to the astrophysical conditions, the main determinant of the shape of the light curve is the nuclear physics involved [78]. The nuclear physics input consists of the fast (p,γ), (α,γ) and (α,p) reaction rates and slow β^+ decays. Single-zone [79] and multi-zone [80, 81] X-ray burst models have been used to study the impact of the uncertainties derived from these nuclear physics inputs [24,82]. Through these analyses, it was shown that only a few reactions play a large role in the uncertainties of the simulated light curves, ash compositions and reccurrence times [24]. The uncertainties come from a few masses with insufficient precision, modifications to terrestrial half-lives needed for high-temperature and high-density environments, as well as continuum electron capture. The dramatic variations in the simulated light curve due to these reaction rate uncertainties can make it difficult to extract astrophysical parameters from comparisons with observed bursting events.

3.1.2 The ^{23}Al$(p,\gamma)^{24}$Si reaction

One of the previously mentioned influential reactions is the ^{23}Al$(p,\gamma)^{24}$Si reaction. Variations within the uncertainty of this reaction rate lead to significant shifts in the simulated X-ray light curve. The impact of this reaction on simulated X-ray bursts is shown in Fig 3.1. In single-zone models, varying the reaction rate up by a factor of 100 generated a sensitivity of 4.8 10^{17} erg s^{-1}. Multi-zone models showed that varying the reaction rate down by a factor of 100 generated a sensitivity of 4.6 10^{38} erg s^{-1}. The ^{23}Al(p,γ) reaction has shown to impact inferred surface gravitational redshift of these binary star systems [83]. Any constraints on this reaction can reveal information about the compactness of the neutron star in

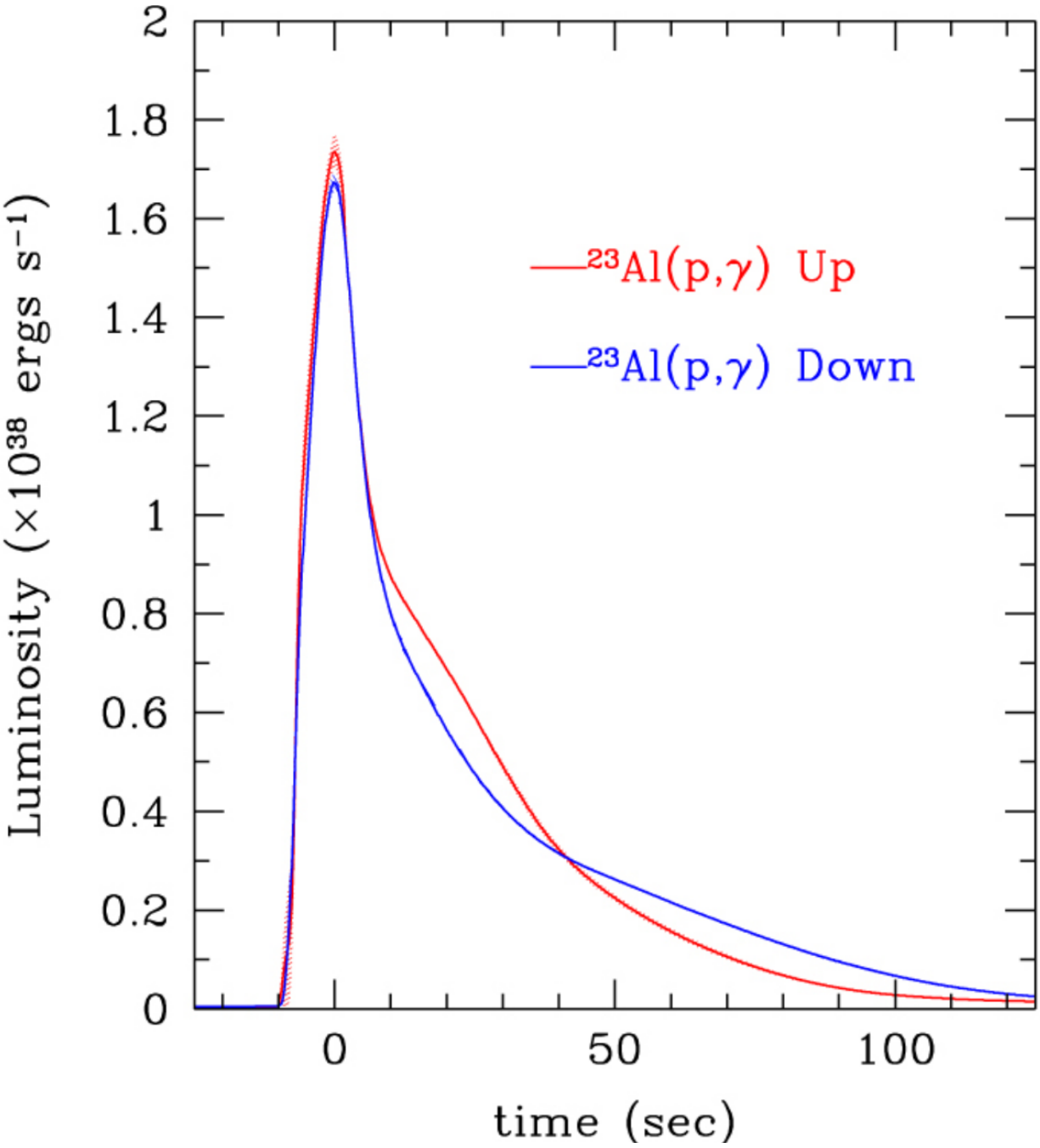

Figure 3.1: A multi-zone X-ray burst model light curve simulation while varying the $^{23}\mathrm{Al}(p,\gamma)$ reaction up and down between a factor of 30 to 100. The variation factor depended on temperature and the resonant uncertainty known at the time. The line width of the simulations represents a 1σ uncertainty of the light curve. The figure was adapted from [24].

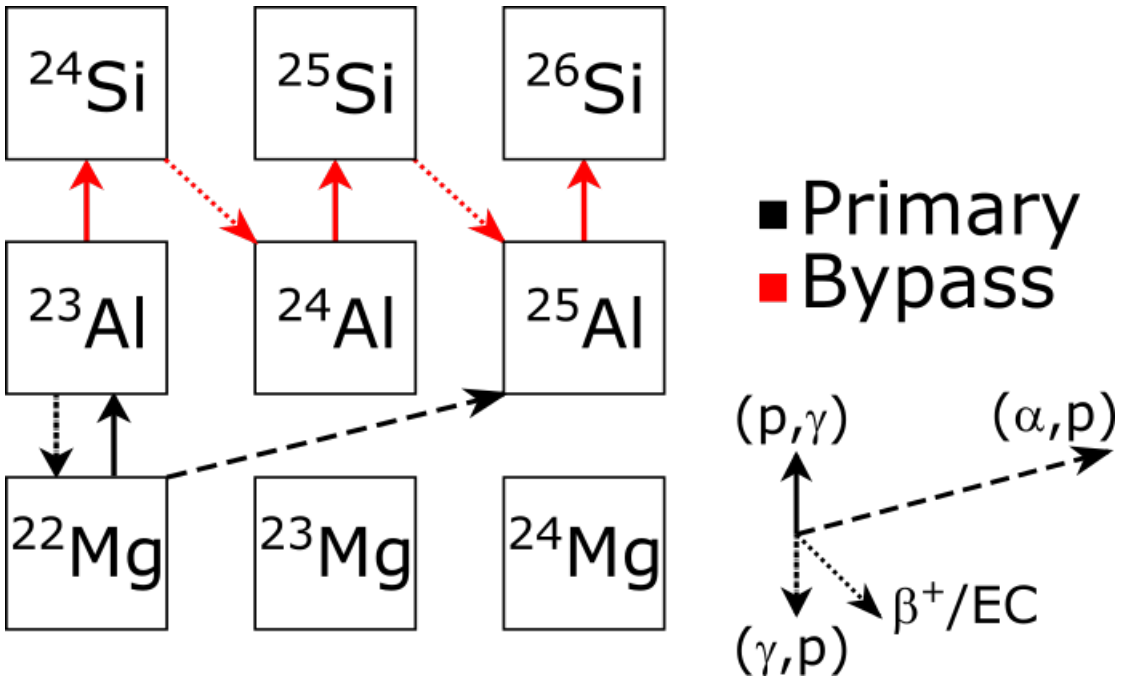

Figure 3.2: The competition between the (α, p) and rp process near the A= 22 waiting point. The ^{22}Mg waiting point forms an equilibrium of proton capture and photodisintegrations due to the low Q value of the reaction.

this binary system [84]. The importance of this reaction stems from its direct connection to the ^{22}Mg waiting point along the rp process [85]. The Q value for $^{22}\mathrm{Mg}(p,\gamma)$ (0.141 MeV) [8] is small enough to establish a (γ, p)-(p, γ) equilibrium [86], which makes it difficult for the rp process to proceed in this mass region. There is evidence [86] that the ^{22}Mg waiting point can be bypassed via the $^{22}\mathrm{Mg}(\alpha, p)$ reaction. However, it is also possible for the $^{23}\mathrm{Al}(p,\gamma)$ reaction to undergo resonant capture to only a few low-lying states in ^{24}Si when certain conditions are assumed for X-ray bursts. The network of reactions that the nucleosynthetic pathway can proceed through is visualized in figure 3.2. This network competition in the reaction flow has been investigated in previous experiments, providing constraints on when $^{22}\mathrm{Mg}(\alpha, p)$ becomes significant during X-ray burst events [29]. However, uncertainties in the $^{23}\mathrm{Al}(p,\gamma)$ reaction need to be resolved in order to confirm the flow of the rp process at this waiting point.

A recent experiment measured γ rays from ^{23}Al(d,n) [1] to identify unbound states in ^{24}Si. This experiment clarified the situation created by previous measurements [87, 88], where there were discrepancies in the unbound level of ^{24}Si. A precise determination of this new level was important because it is expected to make the largest contribution to the ^{23}Al(p,γ) reaction at temperatures relevant for X-ray bursts. The measurement also provided the first constraints on the spectroscopic factors in unbound levels in ^{24}Si, which, in turn, constrained the resonance strengths in ^{24}Si. With the current progress made on this reaction, the uncertainty in the mass of ^{24}Si (19 keV [8]) is now the dominant source of uncertainty for the ^{23}Al(p,γ) reaction rate. A high-precision mass measurement of ^{24}Si would constrain the *rp* process in this mass region by precisely quantifying the bypass of the ^{22}Mg waiting point.

3.2 Experimental Setup

A beam of ^{24}Si was produced from a ^{28}Si^{14+} beam, at an energy of 160 A MeV, with a 1530 mg/cm^2 thin beryllium foil target as described in Ch. 2 Sec. 2.4. The resulting cocktail beam was purified using the A1900 Fragment Separator [69]. Afterwards, the beam was sent through a momentum compression beamline, passing through aluminum degraders and an Al wedge to degrade the beam energy before entering the gas stopper [46]. Following extraction from the beam stopping facility, in conjunction with a silicon detector located after the mass separator, a mass scan can be performed by adjusting the magnetic field strength of the separator and measuring the decays of radioactive isotopes that were transported to the detector. Due to contamination in the gas stopper, the thermalized beam showed activity at different A/Q values. Mass scans performed for ^{27}Si since the chemistry is in the gas cell

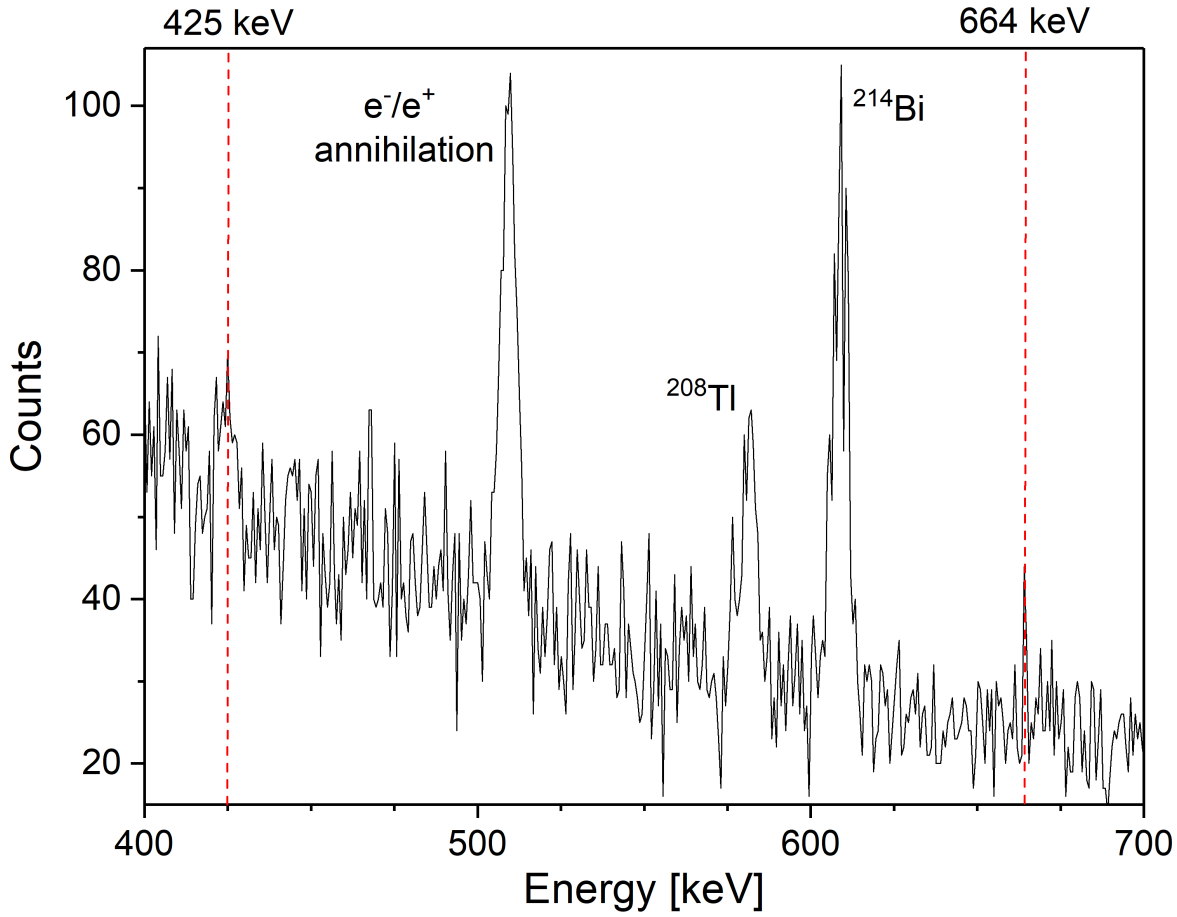

Figure 3.3: The measured gamma-rays that were measured using a high-purity germanium detector. Two low energy β-delayed gamma-rays were identified at $E = 425$ and 664 keV. Since the count rates were so low, seeing their signature was necessary for verifying ^{24}Si was present in the beam during a mass measurement.

is primarily dependent on the chemical element, and the higher rates of the ^{27}Si make the mass scans faster. The results of the mass scan are shown in figure 3.4. Several peaks were identified at different A/Q values from 44 to 98, with ^{27}Si extracted in a molecular form.

To improve the efficiency of extraction for stopped beams, collision-induced dissociation (CID) was used to break up the weakly bound water adducts by creating a potential difference between the gas cell nozzle and extraction RFQ [49, 50]. After applying CID, the mass scan showed that the efficiency improved with less molecular contaminant mass peaks as observed in figure 3.4. After changing the transmitted A/Q of the dipole mass separator for $A/Q = 24$, contaminants were analyzed at $A/Q = 24$, 41 and 57. After contamination identification was performed, the $A/Q = 57$ peak was identified as optimal for performing the cyclotron frequency measurements. Since the rates were low, gamma rays were also measured using a high-purity germanium detector to provide evidence of ^{24}Si in the extracted beam. The β-delayed gamma rays for ^{24}Si were observed in competition with background and the spectrum can be found in figure 3.3. Following the beam stopping facility, ^{24}Si was delivered as a molecular ion, $[^{24}SiO_2H]^+$ at $A/Q = 57$. The beam was then transported to the LEBIT [9] facility where the mass measurements were performed.

The major contaminants identified at $A/Q = 57$ during the experiment were $[C_3H_2F]^+$, $[C_2HS]^+$ and $[C_3H_5O]^+$. The TOF-ICR technique was then used to measure the mass of the ion of interest, with the TOF resonance curve observed in figure 3.5a. An overview of the TOF-ICR technique is described in Chapter 2 Section 2.3. Another excitation scheme used in TOF-ICR, known as a Ramsey excitation [25], was also performed in this experiment. This generates a TOF pattern visible in figure 3.5b and described by Ref [25], which allows superior precision versus the continuous RF excitation scheme for the same ion trapping times. 18 measurements of $[^{24}SiO_2H]^+$ were performed, consisting of 6 normal continuous

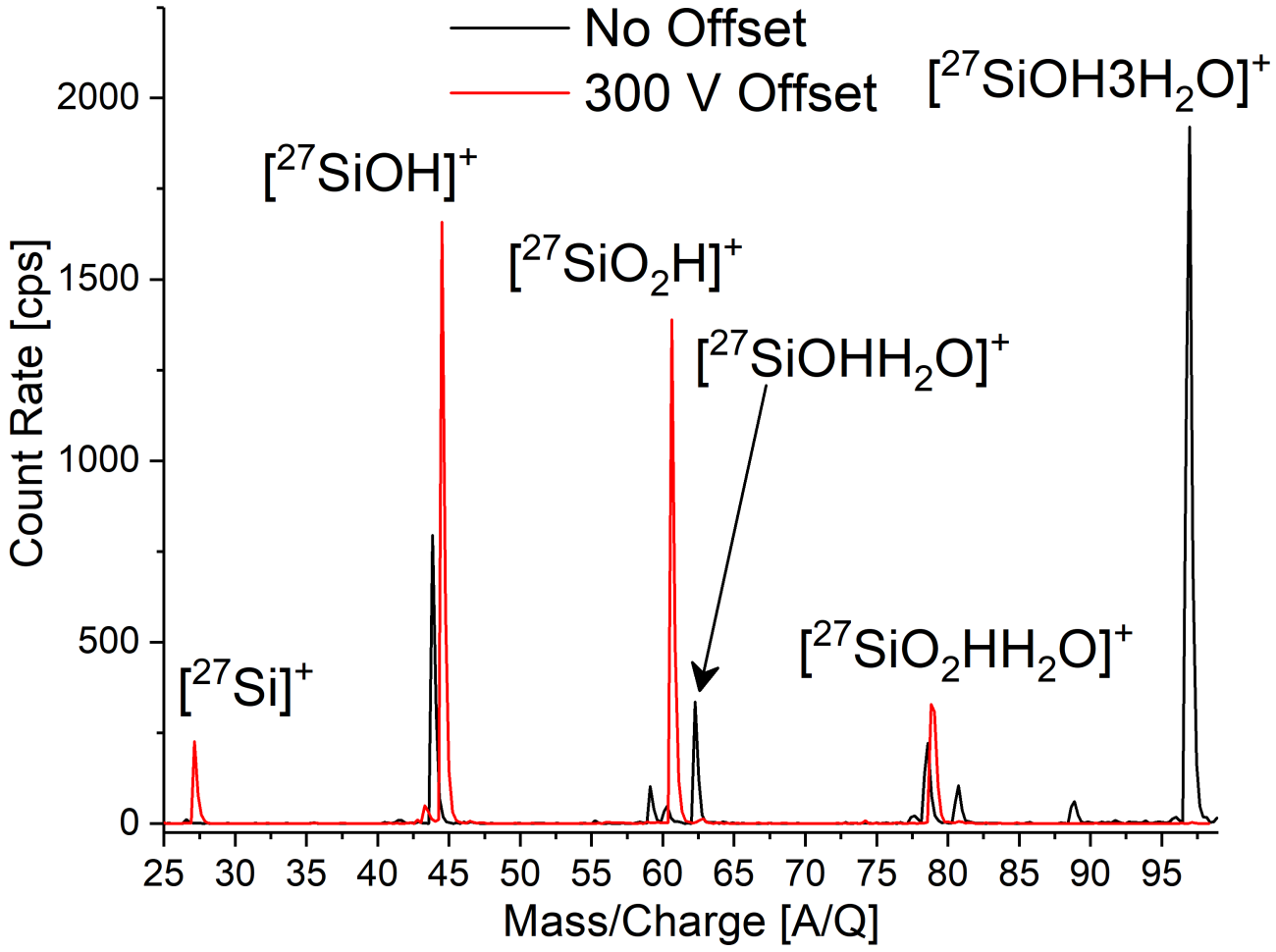

Figure 3.4: A mass scan performed for ^{27}Si, which saw radioactivity at $A = 44$, 60, 62, 78, and 98. After creating a 300 V offset between the gas cell nozzle and extraction RFQ, the mass scan consolidates the ion of interest to $A = 27$, 44 and 60.

excitation measurements and 12 Ramsey excitation measurements. The normal quadrupolar excitation measurements were performed with 50 ms and 75 ms excitations. The Ramsey measurements were performed with 25 ms, 50 ms, 75 ms, 100 ms and 150 ms excitations.

3.3 Results

Cyclotron frequency measurements of $[^{24}SiO_2H]^+$ were bracketed between two reference measurements of $[^{12}C_3H_2F]^+$ to track variations in the magnetic field strength. The weighted average of the ratio for $\nu_c([^{24}SiO_2H]^+)/\nu_c([^{12}C_3H_2F]^+)$ was determined to be $\bar{R} = 1.000085151(71)$ with an associated Birge Ratio [89] of 1.03. Most systematic uncertainties in $\bar{R}$ scale linearly with the mass difference between the ion of interest and the reference ion [56]. This mass-dependent shift has been measured to be $\Delta\bar{R} = 2 \times 10^{-10}$/u [90], which is negligible for isobaric species. Other systematic uncertainties include relativistic effects, ion-ion interactions, and non-linear magnetic field fluctuations. Relativistic effects are negligible compared to the statistical uncertainty [57]. Ion-ion interactions were limited by excluding shots with more than 5 ions. The non-linear fluctuations in the magnetic field are on the order of $\Delta\bar{R} = 10^{-9}$/hour [91]. The longest single measurement was 2.5 hours making these fluctuations negligible as well. As a result, the uncertainty of our averaged frequency measurement is statistical.

The mass excess of ^{24}Si is extracted directly from $\bar{R}$, and was determined to be 10 753.8(37) keV. The value was obtained using

$$m_{\text{interest}} = \frac{1}{\bar{R}}(m_{\text{ref}} - m_e) + m_e, \tag{3.1}$$

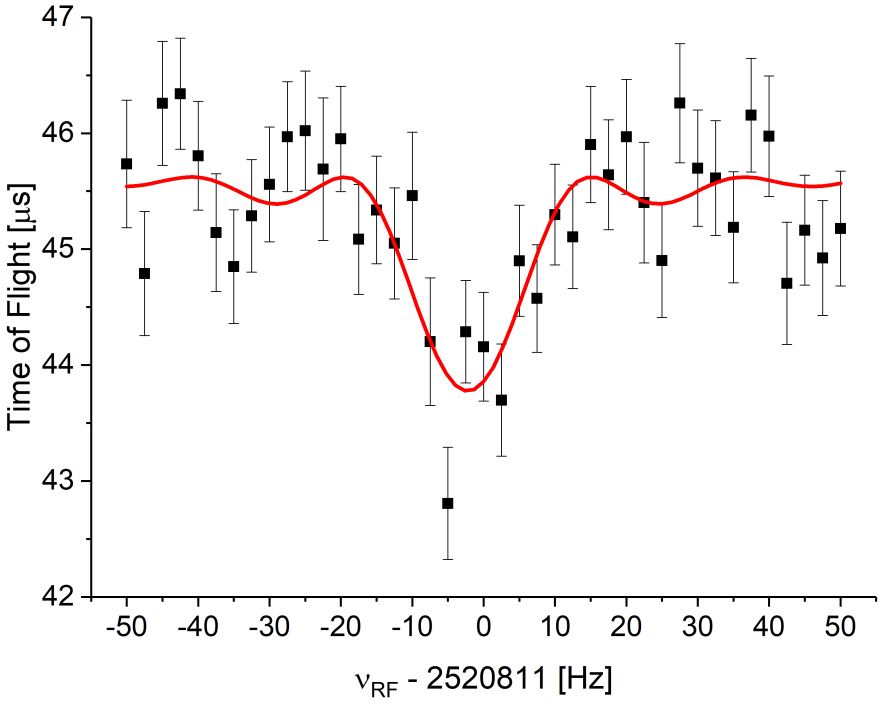

(a) An example of a 50-ms quadrupolar resonance of $[^{24}SiO_2H]^+$.

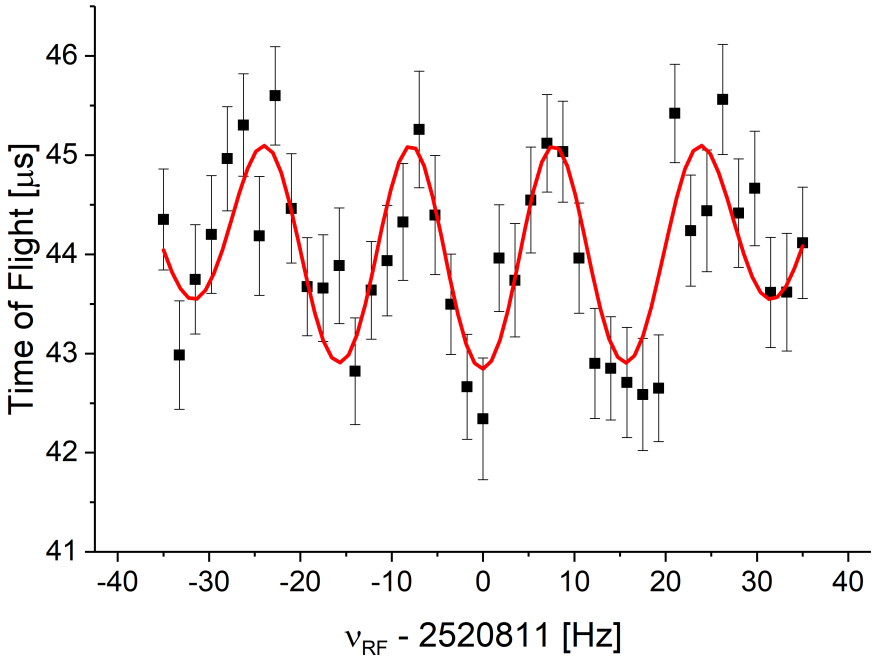

(b) An example of a 75-ms Ramsey resonance of $[^{24}SiO_2H]^+$.

Figure 3.5: The line shape for a quadrupolar excitation is a theoretical curve described in [23]. For Ramsey excitations, the description for the theoretical line can be found in [25].

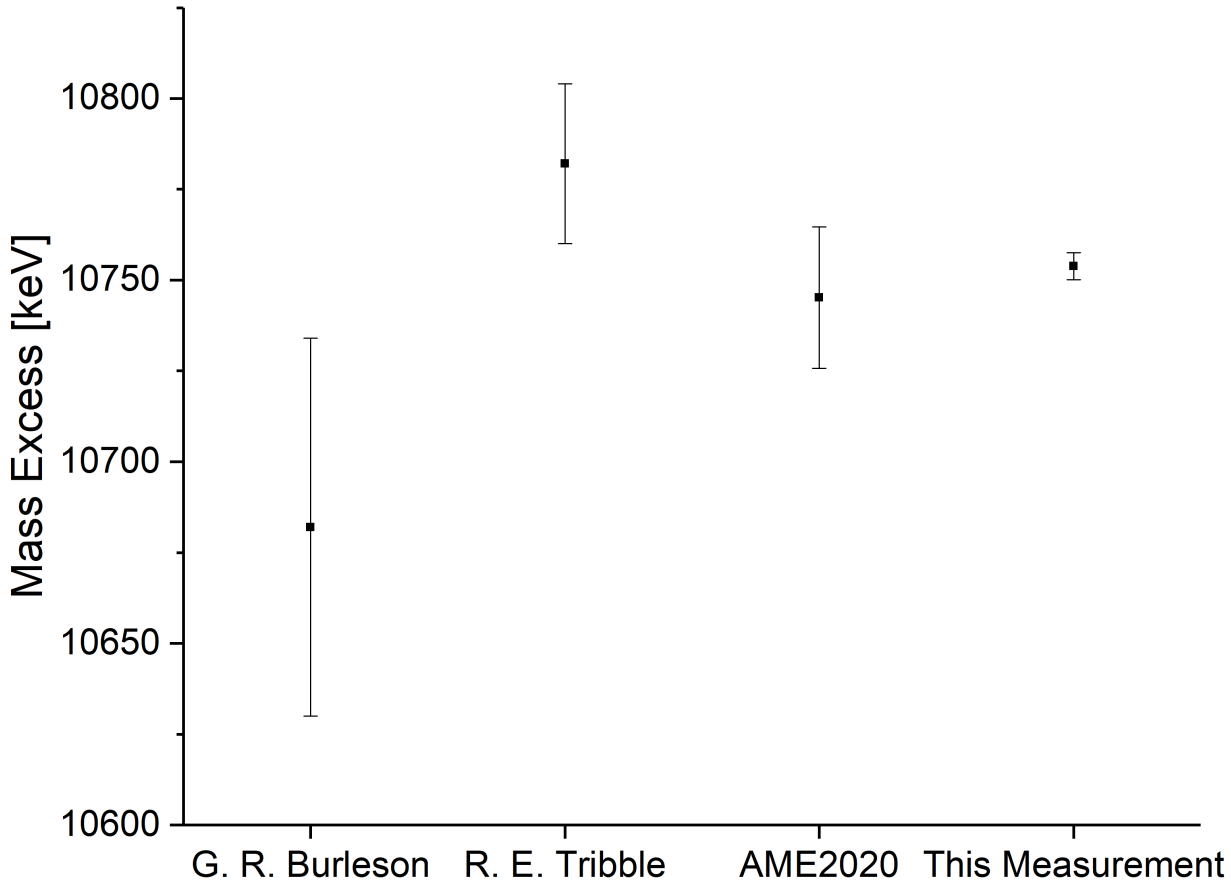

Figure 3.6: The experimental measurements of ^{24}Si performed that contributed to the AME2020 value compared to this measurement. Experimental values can be found in Ref. [8, 26, 27].

where m_{interest} is the mass of $^{24}SiO_2H$, m_{ref} is the mass of $^{12}C_3H_2F$ and m_e is the mass of the electron. The mass values for the reference ion were derived from the AME2020 [8] while the molecular binding energy and ionization energy were on the order of eV and do not impact the final uncertainty. Our mass is in good agreement with the AME2020 (10 745(19) keV), and a factor of 5 more precise. The AME2020 value is primarily based on a pion double-charge exchange reaction ($^{24}Mg(\pi^+, \pi^-)^{24}Si$) measurement [26]. Another measurement that contributed to the AME2020 value was a Q value measurement from the $^{28}Si(\alpha,^8 He)^{24}Si$ reaction [27]. The improvement on the mass value can be understood visually in figure 3.6. With our measurement, a new proton separation energy for ^{24}Si was calculated to be 3 283.2(37) keV.

3.4 Astrophysical Analysis

With a precisely known Q value, the flow following the ^{22}Mg waiting point in the rp process is strictly constrained based on nuclear physics information. Figure 3.7 displays the impact of the new Q value on the uncertainty of the $^{23}Al(p, \gamma)$ reaction rate. Also shown in Figure 3.7 are the $^{22}Mg(p, \gamma)$ reaction rate, which is represented by the black band, based on information from Ref. [28], and the reaction rate experimentally determined for the $^{22}Mg(\alpha, p)$ reaction represented by the blue band from Ref. [29]. We estimate the $^{22}Mg(\alpha, p)$ reaction rate uncertainty to be $\pm 80\%$ based on the uncertainty for the lowest-energy cross section measurement from Ref. [29].

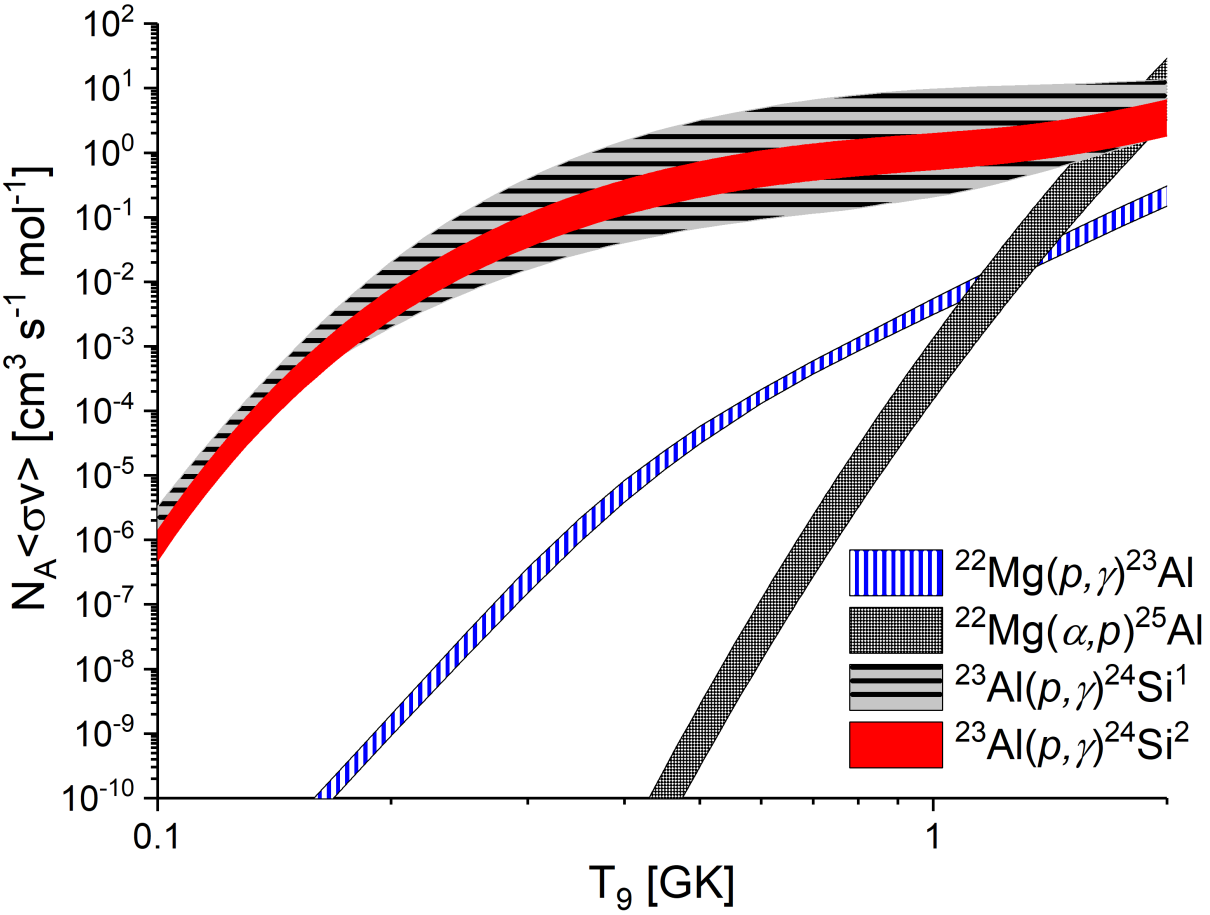

Figure 3.7: The reaction rates for ^{23}Al(p,γ) (Wolf et al. 2019 [1], denoted by the superscript 1, and this work, denoted by the superscript 2), ^{22}Mg(p,γ) (Iliadis et al. 2010, [28]) and ^{22}Mg(α,p) (Randhawa et al. 2020, [29]) from 0.1 to 2 GK. Our calculations show a dramatic reduction in the 1-σ reaction rate uncertainty for ^{23}Al(p,γ) as a result of our new mass measurement and the corresponding resonance energies.

3.4.1 ^{23}Al$(p,\gamma)^{24}$Si reaction rate calculation

The ^{23}Al(p,γ) reaction rate was calculated using the narrow resonance approximation [92], with the following equation below,

$$N_A\langle\sigma v\rangle_r = \frac{1.5399\times10^{11}}{\left(\frac{M_0M_1}{M_0+M_1}T_9\right)^{3/2}}\sum_i(\omega\gamma)_i e^{-11.605E_i/T_9} \tag{3.2}$$

M_0 and M_1 are the masses of the projectile and target nucleus in a reaction in atomic mass units. The resonance strengths of a narrow resonance are represented by $\omega\gamma$. E_i is the resonance energy of an unbound level in units of MeV and T_9 is the temperature of the environment this reaction is taking place in in units of GK. The information that contributed to this calculation can be found in Table 3.1, based on experimental information [1], and, for higher lying states, on calculations with NuShellX@MSU [2] that were included in the reaction rate calculation of Ref. [1]. Based on a previous measurement of longitudinal momentum distributions of ^{24}Si states [93], we assigned the 3471 state with J=0 and used the information from Ref. [1].

The reaction rate properties varied using a Monte Carlo random sampling approach. The excitation energies in the unbound states of ^{24}Si and the Q value for the ^{23}Al(p,γ) reaction were varied, assuming a normal distribution. The impact of the proton penetration factor was also included in the reaction rate calculation [94] as a result of the Coulomb wave function, which can impact the particle photon widths of the reaction based on the temperature and contribution of a resonance. The excitation energies derived from NuShellX@MSU calculations were defined with uncertainties of 150 keV [3]. The radiative widths and spectroscopic factors were varied with a Log-normal distribution [95]. While a gaussian distribution assumes μ and σ are the mean value and its uncertainty, the Log-normal distribution defines

E_x (MeV)	J	l	C^2S	Γ_γ (eV)	Γ_p (eV)
3.449(5)	2	0	0.7(4)	1.9×10^{-2}	1.0×10^{-4}
		2	0.002(1)		
		2	0.3(2)		
3.471(6)	0	2	0.8(4)	1.6×10^{-3}	6.2×10^{-5}
4.256(150)*	3	0	0.59	1.3×10^{-2}	9.0×10^{3}
		2	0.17		
5.353(150)*	3	0	0.0012	2.8×10^{-2}	3.6×10^{3}
		2	0.11		
5.504(150)*	2	0	0.044	2.2×10^{-1}	2.8×10^{4}
		2	0.068		
5.564(150)*	4	2	0.048	2.2×10^{-2}	2.2×10^{3}
6.004(150)*	4	2	0.28	6.5×10^{-3}	2.8×10^{4}
6.056(150)*	0	2	0.053	3.4×10^{-3}	5.6×10^{3}
6.072(150)*	2	0	0.012	5.0×10^{-2}	2.4×10^{4}
		2	0.093		

Table 3.1: Resonance levels used in the narrow-resonance approximation for the reaction rate calculation. Experimental information is taken from Ref. [1]. Other levels were calculated with the NuShellX@MSU package with their corresponding spectroscopic factors, radiative widths and proton widths [2], as denoted by *. Excitation energies from NuShellX@MSU calculations were defined with uncertainties of 150 keV [3]. The reaction rate was calculated with a Monte Carlo program to determine a robust rate uncertainty. A complete description of the reaction rate calculation can be found in the text.

μ and σ differently, as shown below,

$$\mu = \ln E[x] - \frac{1}{2}\ln\left(1 + \frac{V[x]}{E[x]^2}\right), \quad \sigma = \sqrt{\ln\left(1 + \frac{V[x]}{E[x]^2}\right)}. \tag{3.3}$$

The equations above apply when the quantities of interest have been measured. If a quantity is not known, then the median value $E[x]$ of the theoretical prediction is used for $\mu = \ln E[x]$ and a factor uncertainty is $V[x]$ for $\sigma = \ln V[x]$. All radiative partial widths assumed a factor uncertainty of 2 [96]. The same factor uncertainty was used for all theoretical spectroscopic factors. Experimental spectroscopic factors and uncertainties were varied using relations found in Ref. [95]. The proton partial widths were scaled, based on the impact of the

spectroscopic factor variation.

T_9	$N_A\langle\sigma v\rangle$ (cm^3/s/mole)		
	Recommended	Lower	Upper
0.1	8.195×10^{-7}	4.777×10^{-7}	1.402×10^{-6}
0.15	2.754×10^{-4}	1.640×10^{-4}	4.642×10^{-4}
0.2	4.481×10^{-3}	2.602×10^{-3}	7.761×10^{-3}
0.3	6.168×10^{-2}	3.432×10^{-2}	1.114×10^{-1}
0.4	2.022×10^{-1}	1.099×10^{-1}	3.746×10^{-1}
0.5	3.834×10^{-1}	2.052×10^{-1}	7.212×10^{-1}
0.6	5.594×10^{-1}	2.967×10^{-1}	1.064
0.7	7.096×10^{-1}	3.745×10^{-1}	1.360
0.8	8.328×10^{-1}	4.392×10^{-1}	1.601
0.9	9.381×10^{-1}	4.950×10^{-1}	1.801
1.0	1.034	5.482×10^{-1}	1.979
1.5	1.707	9.329×10^{-1}	3.303
2.0	3.222	2.010	6.553

Table 3.2: The recommended reaction rate based on information from Ref. [1] and this work. Also included are the lower (16th percentile) and upper (64th percentile) uncertainties of this reaction rate.

The direct capture component of the reaction rate was calculated using the formula below

$$N_A\langle\sigma v\rangle_{nr} = 7.83 \times 10^9 \left(\frac{Z(M_0+M_1)}{M_0 M_1 T_9^2}\right)^{1/3} S(E_0) e^{-4.29\left(Z^2 M_0 M_1/(M_0+M_1)T_9\right)^{1/3}} \quad (3.4)$$

with the spectroscopic factors for each astrophysical S-factor reported in Ref. [97] varied with a Log-normal distribution as well. The experimental ground state spectroscopic factor was varied with its experimental uncertainty while the three theoretical values calculated for the first excited state assumed a factor uncertainty of 2. After varying the spectroscopic factor, the corresponding astrophysical S-factors $S(E_0)$ were scaled to calculate the new S-factor before summing all four contributions in the direct capture component calculation. Finally, the mass uncertainty no longer limits the uncertainty of the ^{23}Al(p,γ) reaction rate.The results for the calculated rate for the ^{23}Al(p,γ) rate can be found in Table 3.2.

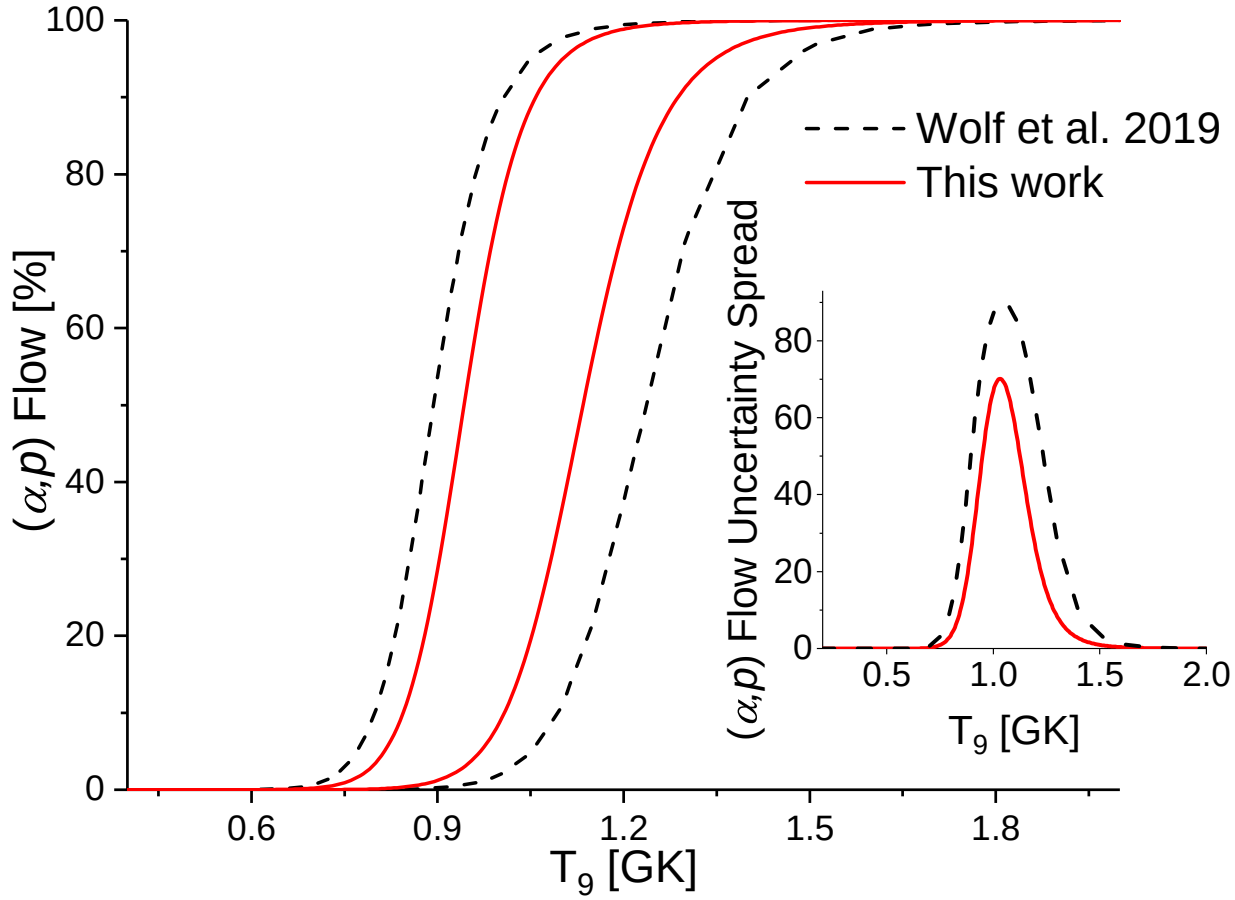

Figure 3.8: Flow through $^{22}\mathrm{Mg}(\alpha, p)$ for the temperature range of relevance for X-ray bursts, where the solid black lines assume the $^{23}\mathrm{Al}(p, \gamma)$ reaction rate uncertainty of Ref. [1] and the dashed red lines correspond to the uncertainty from this work. The inset shows the uncertainty spread in the (α, p) flow, which peaks at temperatures reached during the light curve rise in X-ray burst model calculations.

3.4.2 Mass Flow Competition Analysis from ^{22}Mg waiting point

We assessed the impact of the new ^{24}Si mass on the onset of the αp-process by calculating the flow at the ^{22}Mg bottleneck. To first order, at this point in the reaction network, there is a competition between $^{23}\mathrm{Al}(p,\gamma)$ and $^{22}\mathrm{Mg}(\alpha,p)$, given the rather long half-life of ^{22}Mg, 3.88 s [98], and low proton separation energy S_p of ^{23}Al, 0.141 MeV [8]. The flow into the αp-process is defined as $\lambda_{\alpha,p}/\left(\lambda_{p,\gamma}+\lambda_{\alpha,p}\right)$. The rates are

$$\lambda_i = W\left(X_i/A_i\right)\rho N_{\mathrm{A}}\langle\sigma v\rangle, \tag{3.5}$$

where X_i and A_i are the mass fraction and mass number of hydrogen and helium for the $^{23}\mathrm{Al}(p,\gamma)$ and $^{22}\mathrm{Mg}(\alpha,p)$ reactions, respectively [99]. W is a weight factor, which is the equilibrium abundance of the nuclide as determined by the Saha equation [78, 100]. The weight factor can be evaluated for ^{23}Al with

$$W_{^{23}\mathrm{Al}} = \frac{1}{2}\left(2+f(T)-\sqrt{(f(T))^2+4f(T)}\right), \tag{3.6}$$

where,

$$f(T) = 2\frac{n_q}{n_p}e^{-Q/k_BT},\ \ n_q = \left(\frac{m_p k_B T}{2\pi\hbar}\right)^{3/2}. \tag{3.7}$$

The quantities involved in the weight factor calculation are the quantum concentration n_q, proton density n_p, $^{22}\mathrm{Mg}(p,\gamma)$ reaction Q value, Boltzmann constant k_B and the temperature of the stellar environment T. The weight factor for ^{22}Mg is simply $W_{^{22}\mathrm{Mg}} = 1 - W_{^{23}\mathrm{Al}}$. Since the ^{22}Mg β^+-decay rate is too slow to compete, only strong and electromagnetic interactions are involved in the flow, and the density dependence ρ cancels. For X_i, the H and He mass-fractions in the ignition region depend on the adopted astrophysical conditions.

In order for flow through ^{22}Mg(α, p) to be significant at temperatures usually found in X-ray burst model calculations, $X_{\rm H}$ has to be relatively low and $X_{\rm He}$ has to be relatively high. As referenced by [101], we take the conditions determined for the X-ray burst ignition region as where $X_{\rm H} = 0.03$ and $X_{\rm He} = 0.31$. Results are shown in Figure 3.8 over the range of temperatures of relevance for X-ray bursts.

For the following discussion, we adopt 10% of flow through ^{22}Mg(α, p) as the point when the αp-process becomes significant. Previously, using the ^{23}Al(p, γ) reaction rate uncertainty from Ref. [1], the uncertainty band for when the αp-process becomes significant is $T_9 = 0.94\pm$ 0.15 GK. With the new ^{24}Si mass, this uncertainty band becomes 0.93 ± 0.08 GK, precisely pinpointing the onset of the αp-process in X-ray bursts. A hotter envelope (achieved with a larger accretion rate or higher base heating flux) will enable thermonuclear runaway via the triple-α process to occur for smaller $X_{\rm He}$ (and therefore larger $X_{\rm H}$). Adopting other ignition conditions shifts the temperature for significant αp-process flow, e.g. 0.99 ± 0.09 GK for the $X_{\rm H} = 0.06$ $X_{\rm He} = 0.19$ ignition conditions from the calculations of Ref. [99], the precision remains 9%. Therefore, we firmly establish the relevance of the αp-process in powering X-ray burst light curves by determining under which conditions there is (α, p) breakout from the ^{22}Mg waiting-point. Further refinement would require more precise resonance strength determinations for ^{23}Al(p, γ), which has recently been published after the completion of this work by Ref. [102]. Another area of improvement is through a measurement of the ^{22}Mg(α, p) cross section to lower center-of-mass energies.

Chapter 4

Development of a Collision-Induced Dissociation Gas Catcher (CIDGC) For Purification of Stopped Beams

4.1 CIDGC Motivation and Introduction

The motivation for developing the CIDGC technique is to find a better way to mitigate performance-limiting effects caused by the stopping of high-energy ions in gas stoppers as they are applied at FRIB and other high-energy RIB facilities [46, 47, 103–107]. Experience gained throughout the past two decades [45–47, 107, 108] points at three challenges that continue to be addressed. These are space charge effects, charge exchange, and chemical reactions.

When high-energy ions are stopped in the helium used in present gas stoppers they create $\sim 10^6$ He^+/e^- pairs by every ion [109–111]. This has different effects due to the electric field created by space charge and a neutral plasma region: decreased transport/extraction efficiencies and a reduced effective extraction volume. An additional important effect is the creation of both stable and radioactive molecules that occur during the stopping process in a high-pressure gas cell. The copious abundance of He^+ created by ions stopping leads

to the production of molecular ions via charge exchange with contaminants present in the stopping gas. Even a constituent with relative abundance below one part per million can result in an ion current exceeding the picoampere level. Such intense stable molecular ions can overwhelm ion cooler/buncher systems used to create the brilliant ion pulses required for mass measurements and some laser spectroscopy studies, while even low-intensity stable molecular ion currents can interfere with Penning trap mass spectroscopy. Similarly, the formation of radioactive molecular ions, such oxides or lightly bound adducts [45, 112, 113] will preclude the use of these RIBs in laser spectroscopy studies, which tends to require elemental species.

This issue was also observed during the ^{24}Si experiment [4] described in the previous chapter. Table 4.1 lists the different ^{24}Si molecules identified during scans using the magnetic mass separator and contaminant molecules identified at each A/Q using PTMS. As a result, the creation of ^{24}Si ions at different masses reduced the quantity of ^{24}Si delivered to LEBIT and thus reduced the efficiency of the measurement. The identification of $[^{24}SiO_2H]^+$ as the molecule with contamination low enough for in-trap cleaning cost about 24 hours of beam time. The ^{24}Si case is only one of many that motivate the development of gas catcher techniques that lead to cleaner beams, for example, by utilizing CID [49, 50] to reduce the distribution of the rare isotope across multiple molecular sidebands and to also break down stable molecular ions.

4.1.1 Overview of CID

CID is a common analytical chemistry technique, and there are also other forms of dissociation techniques are employed. Similar to CID, surface-induced dissociation (SID) can be used via scattering off an incident surface but suffers from more degrees of freedom [114–117].

m/q (A/Q)	Ion of Interest	Contaminant
24	$^{24}Si^{+}$	$^{12}C_2^{+}$
41	$[^{24}SiOH]^{+}$	$[C_2OH]^{+}$, $[N_2CH]^{+}$
57	$[^{24}SiO_2H]^{+}$	$[C_3H_2F]^{+}$, $[C_2HS]^{+}$, $[C_3H_5O]^{+}$

Table 4.1: Contaminants identified during the ^{24}Si mass measurement campaign [4]. Each contaminant was cleaned out using a combination of RF dipolar excitations and broadband SWIFT excitations. Purification was not always successful if the level of contamination was too high.

Electron-transfer dissociation (ETD) and other forms of electron fragmentation are also available [118–122], with an overview provided in Ref. [123].

CID is considered an approach that may most effectively remove molecular contaminants. CID involves colliding molecular ions with neutral gas to excite rotational and vibrational modes in the energetic molecule leading to the molecule's dissociation [124]. There is also a difference between low energy (1-100 eV) and high energy (1 - 10 keV) CID, depending on the interest of the researcher [49]. Based on the energetics of stopped beam experiments, high-energy CID will be the only method available at FRIB. An illustration of CID using gaseous He is given in Fig. 4.1.

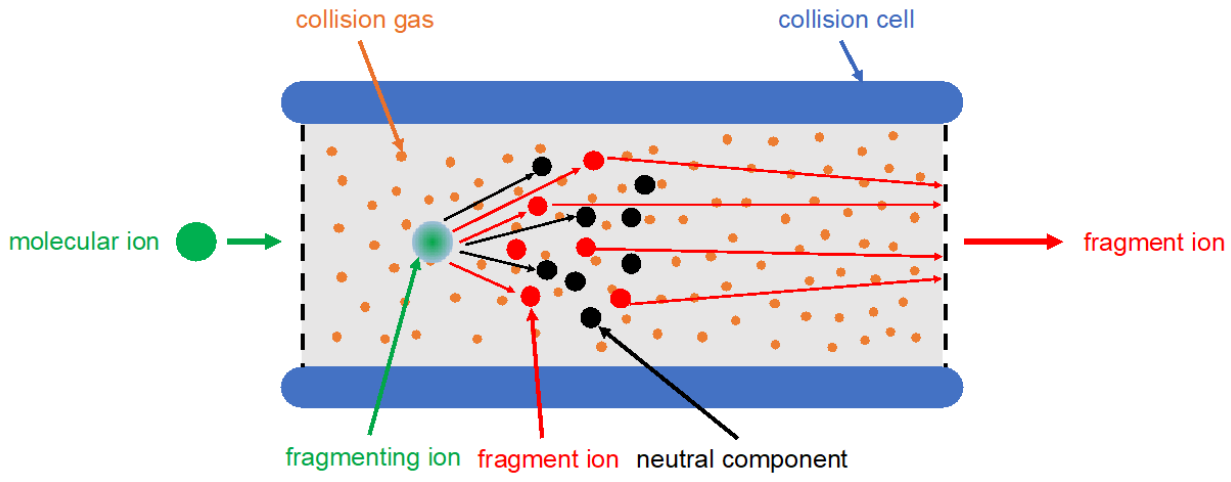

Figure 4.1: An illustration of the CID mechanism. The collisions with the He atoms are responsible for the eventual dissociation of the incoming molecular ion.

At several facilities worldwide, CID is being studied with regard to providing cleaner beams from RFQ cooler/bunchers and after gas stoppers. Most recently, CID has been implemented at GSI with their RFQ cooler buncher [125]. CID has also been studied at TITAN with their RFQ cooler/buncher [126] and with molecular fragments measured using a multiple reflection time of flight (MR-TOF) mass spectrometer to clean out molecular hydrocarbon contaminants. The same technique has been used with the LEBIT cooler/buncher [52]. CID is also performed after the FRIB gas stoppers by putting a potential difference between the extraction RFQs and the gas cells.

As part of this thesis work, a prototype called the CID Gas Catcher (CIDGC) has been developed to investigate and perform high-energy CID. The advantage of high-energy CID is the ability to break up strongly bound molecules, like those with covalent triple bonds. Examples are carbon monoxide and dinitrogen; their covalent bond energies are 11.11 eV and 9.75 eV, respectively. This is because high-energy CID causes vertical electronic excitation, and using He reduces the scattering length of the field-free drift region [127]. Increasing the pressure of the He also increases the fragmentation efficiency.

4.2 CIDGC Prototype Overview

An overview of the CIDGC design is shown in Fig. 4.2. The CIDGC uses a novel CID technique with a solid membrane followed by a gaseous volume, which differs from traditional CID, where the molecular ion collides solely with a neutral gas. The membrane is installed on a nipple that is biased separately from the rest of the system. To demonstrate CID with the gas catcher, tests will be performed at 30 keV. The following subsections break down the different components and describe their operation.

For the tests, the CIDGC has been installed at one branch of the beam-line, called the d-line, in the stopped beam experimental area at FRIB. The beam is delivered using a bender, followed by a set of electrostatic quadrupoles to focus the beam. After passing through a set of electrostatic steerers, a Faraday cup, MCP and camera are available for performing beam diagnostics before injection into the CIDGC. See Fig 4.3 for an overview of the d-line extension and the location of the CIDGC in the low-energy area.

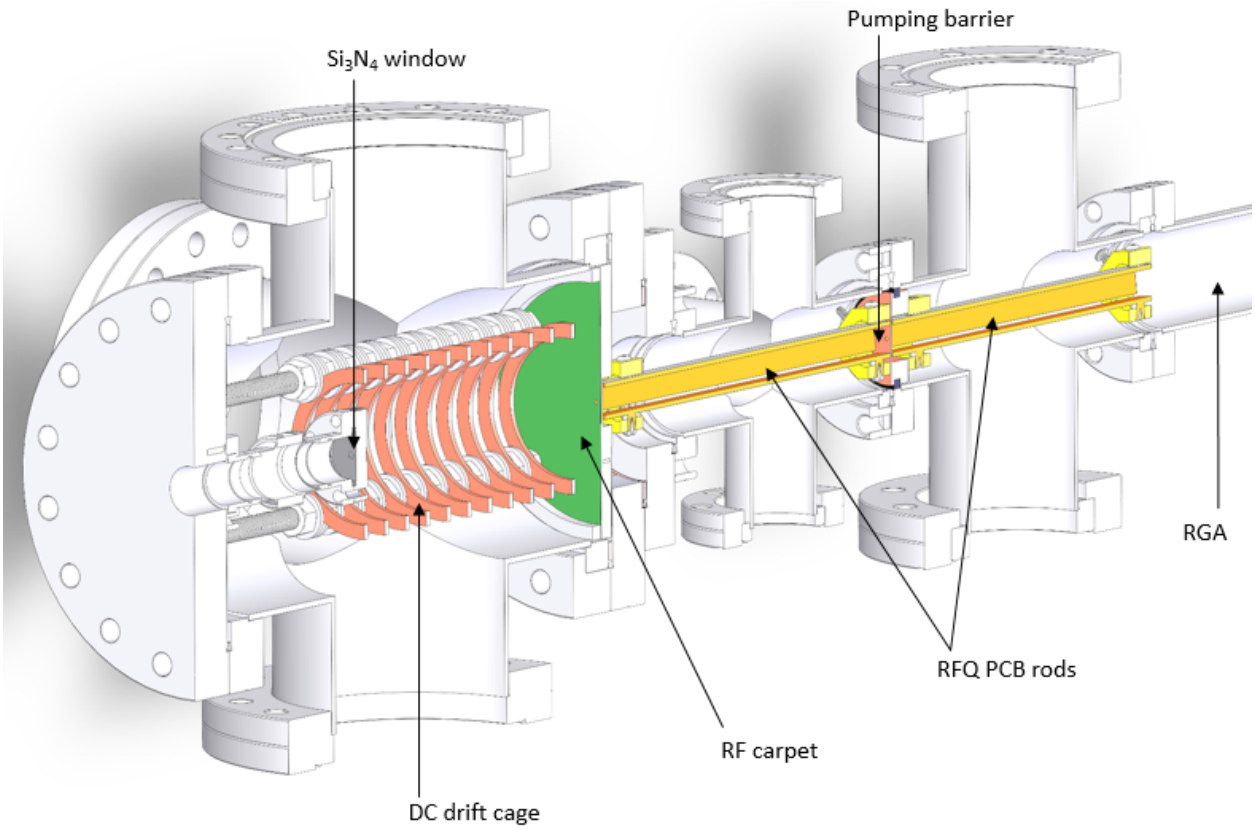

Figure 4.2: A 3D cross-section of the CIDGC prototype developed to perform CID of incoming high-energy molecular ions.

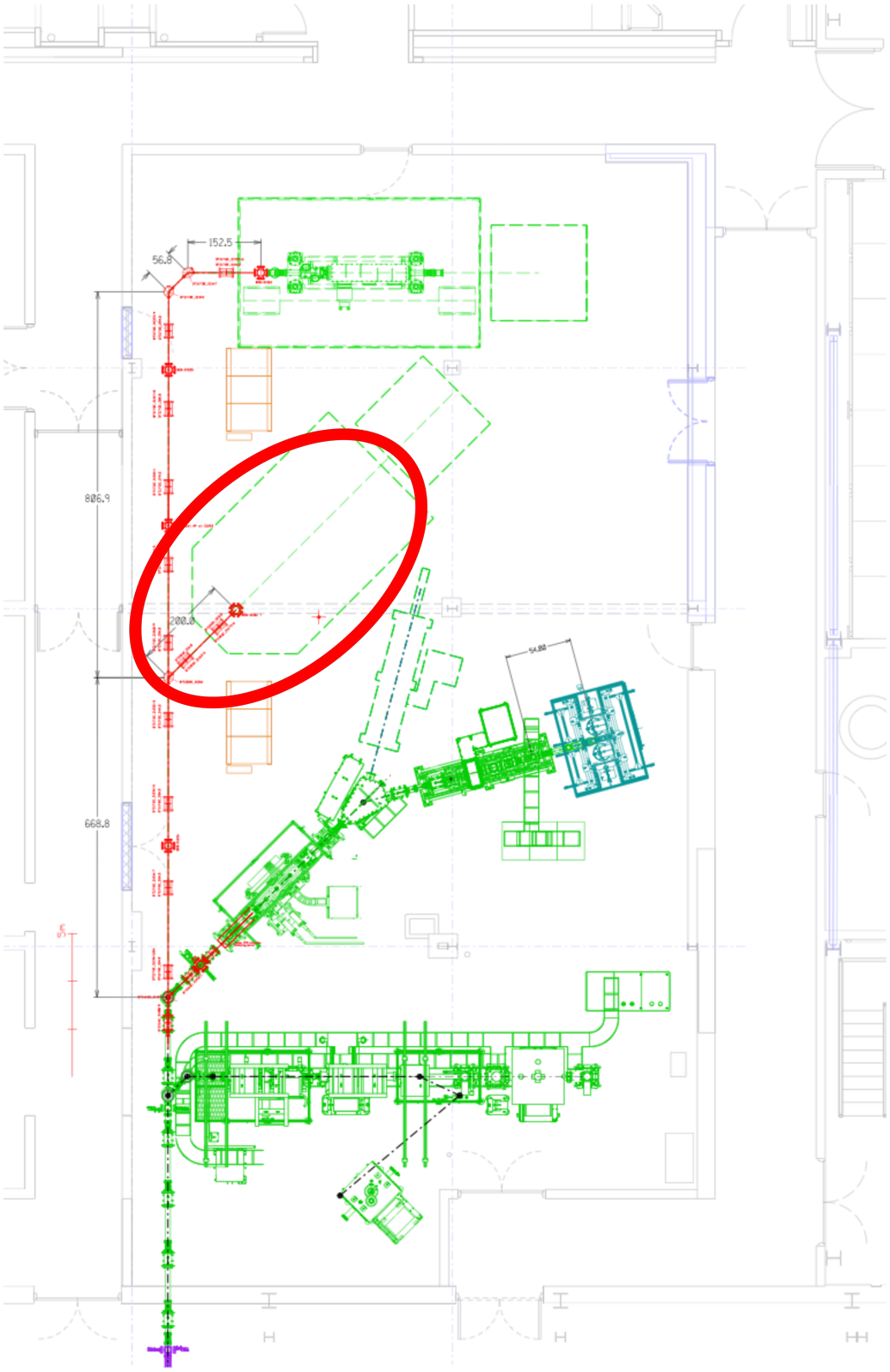

Figure 4.3: An overview of the low-energy area (LEBIT and BECOLA) and the d-line extension. The parts of the beamline colored red represent the d-line extension. The red-bordered ellipse highlights where the location of the CIDGC prototype is installed.

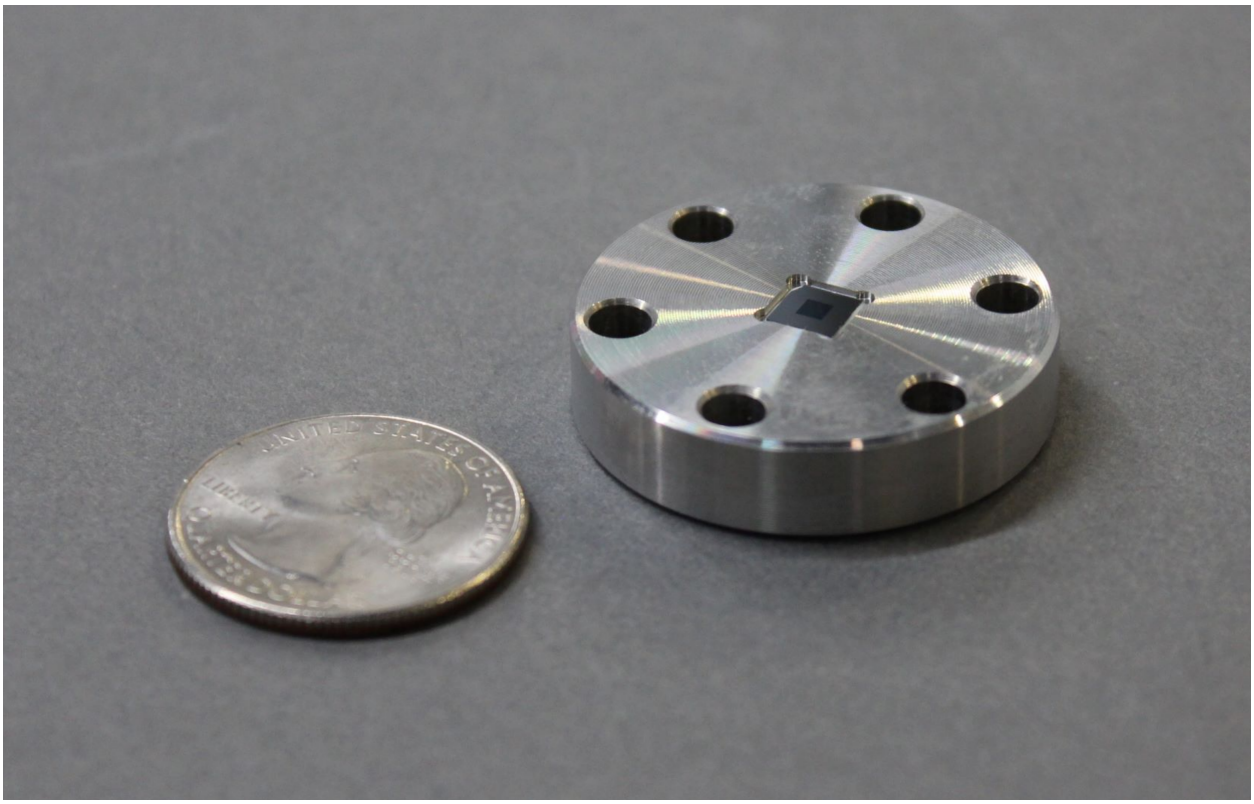

Figure 4.4: The Si_3N_4 installed on a mini-CF flange, with its size compared to a quarter.

4.2.1 The CIDGC Design and Features

4.2.1.1 The Si_3N_4 membrane

The entrance for the CIDGC is a 2 mm x 2 mm Si_3N_4 with a thickness of 21 nm. The Si_3N_4 membrane, along with the He buffer gas inside the cell, will be responsible for performing CID. The presence of the Si_3N_4 serves as a gas barrier and is thin enough to be penetrated by low-energy ions with kinetic energies of a few 10's of keV. The Si_3N_4 is created by Silson Ltd. and is mounted with a Loctite 9492 low-outgassing adhesive on custom machined mini ConFlat (CF) flanges. Figure 4.4 shows an example of a Si_3N_4 membrane on a mini CF flange, which is installed on a nipple at the entrance of the CIDGC.

The Si_3N_4 membranes are created on silicon wafers using a low-pressure chemical vapor deposition system [128]. Si_3N_4 membranes were originally designed to perform transmission

electron microscopy and X-ray microscopy. However, due to its high transmission at this thickness, it's an ideal candidate for CID. Another advantage to using Si_3N_4 membranes is the pressure differential that these membranes can manage. Si_3N_4 membranes 20 nm thick and with the size of the one used here can handle a pressure up to 200 mbar before the window begins to deteriorate, which is much larger than what will be used in the CIDGC.

4.2.1.2 Gas Catcher

Following transmission through the Si_3N_4 membrane, the ions enter a cell filled with ultra pure helium. The helium buffer gas will be responsible for stopping any beam after transmission through the membrane. At the same time, the ions experience a drag force created by a potential difference applied across a set of copper rings, forming a cage. The rings are connected through a series of 1 MΩ glass UHV-compatible resistors, as shown in Fig. 4.5. The Si_3N_4 membrane and cage are biased together and optimized for transport across the cell.

On the opposite side of the Si_3N_4 membrane is a circular RF carpet. The RF carpet was manufactured by Flexible Circuits Inc. as a double layer Printed Circuit Board (PCB) on flexible Kapton material, as shown in Fig. 4.6. Each concentric copper trace on the top layer of the PCB is connected to one of the four electrodes (named A, B, C and D) at the bottom layer using a via, a copper channel that connects the top and the bottom layers of the PCB. The outermost thicker copper trace is electrically isolated from the rest of the traces. By relying on the electrode legs extending from the body and an aluminum retaining ring, the carpet is wrapped around a backing plate as shown at bottom of the figure 4.6. The retaining ring is placed on the outermost copper trace such that they are electrically connected. The backing plate is made out of a hybrid material by combining Aluminum

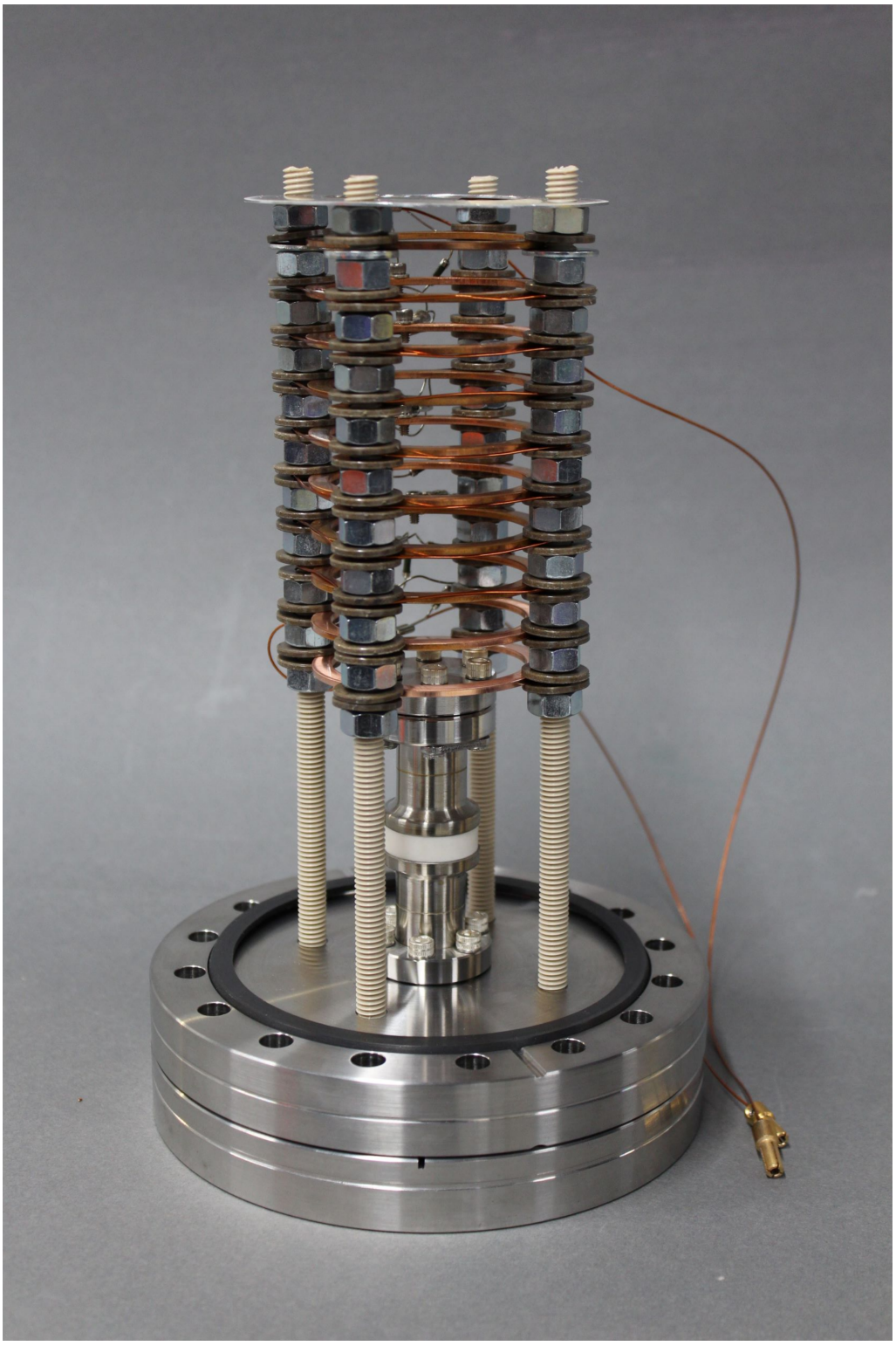

Figure 4.5: The ring electrodes that drag the ions across the length of the cell toward the RF carpet. The window can be seen installed at the start of the ring system.

Nitride with Boron Nitride, also known as Shapal Hi M Soft™ [129]. This particular material was chosen due to its high thermal conductivity and exceptional machinability as opposed to the traditional Aluminum Nitride. The material also has a low thermal expansion and high mechanical bonding strength. Due to the properties of the backing material, silver aquadag paint is added to the other side of the extraction orifice to prevent charging up. Dual-channel arbitrary function generators (AFGs) create the RF signal, and the signals are sent through RF amplifiers. The signals are then sent into a driver circuit that isolates the signal through a transformer and splits it into two phases. The RF voltages travel through variable inductors while connected in parallel via a variable capacitor. The RF voltage is also supplied with a DC bias. The RF voltages are then applied to the carpet copper traces to manipulate ion motion as ions are transported to the extraction orifice. By tuning the variable capacitance and inductance of the circuit to achieve equal reactance, resonance can be achieved, and the RF carpet can surf ions effectively at the resonant frequency. The driver circuitry for the RF carpet can be found in Fig. 4.7.

RF carpets [130], as well as RF funnels [131] and RF walls [132], have been used to transport ions across surfaces and have been traditionally used in gaseous environments. Ion surfing [130] was investigated as an alternative to transporting ions without a DC gradient. The necessary ingredients for ion surfing are a buffer gas to provide adequate damping, a push field to push ions onto the surface, an RF potential 180° out of phase on adjacent electrodes that repels ions from the surface, and a high frequency (HF) 4-phase traveling wave. The overall potential that ions experience is

$$V(x,y,t) = V_{\text{eff,max}} \cdot e^{-2\pi\frac{y}{a}} + E_p \cdot y + V_w \cdot \cos\left(\frac{2\pi}{\lambda}(v_w \cdot t - x)\right) \cdot e^{-2\pi\frac{y}{\lambda}}. \tag{4.1}$$

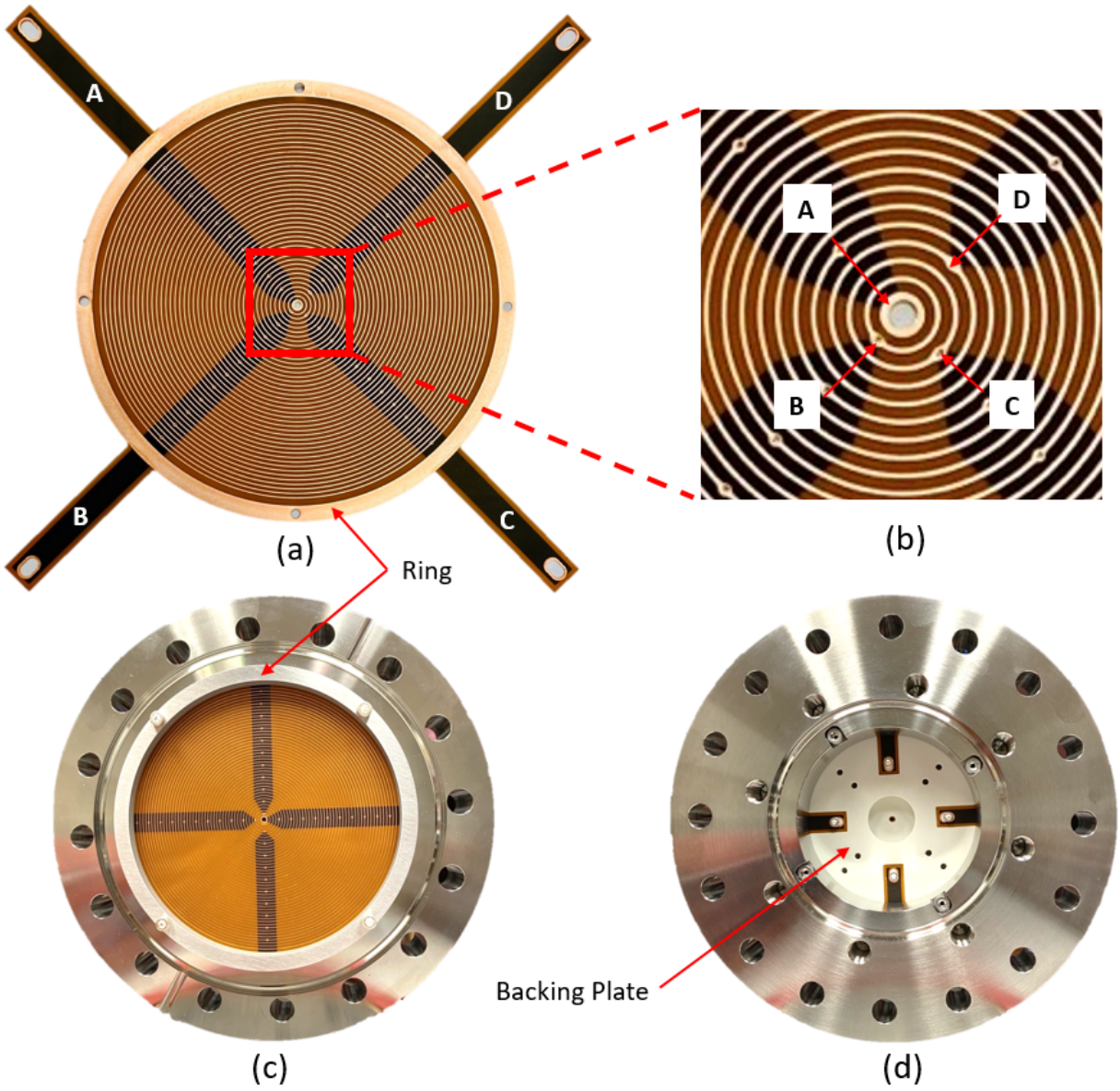

Figure 4.6: The RF carpet printed on a Kapton backing. The RF carpet is then attached to a backing made of Shapal. The RF carpet is responsible for transporting ions from the gas cell into the RFQ ion guide section.

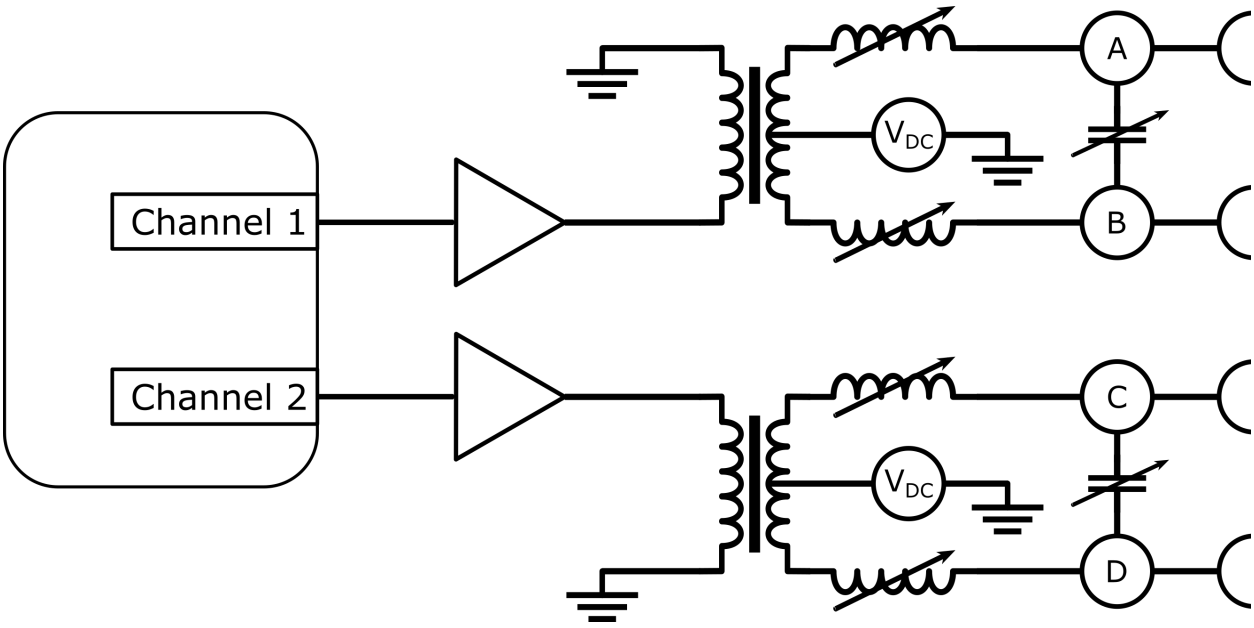

Figure 4.7: A circuit diagram for the RF carpet that is designed to resonantly drive the RF carpet based on the inductance and capacitance of the circuit.

The potential is described by multiple parameters, where a is the pitch of the carpet, y is the distance ions are above the surface, v_w is the speed of the traveling wave, E_p is the strength of the electric field an ion feels above the surface of the carpet from a push force, and $V_{\text{eff,max}}$ contains terms related to damping by the buffer gas and the repelling force generated by the RF. Depending on the amplitude and frequency of the traveling wave, ions will move in either locked or slipping mode.

In our apparatus, the RF carpet operated using a 4-phase RF traveling wave. This ion surfing method is illustrated in Fig. 4.8. This form of ion surfing is also used at the ACGS at the NSCL [47]. The RF carpet in the CIDGC is a circular RF carpet with 4-phase ion surfing installed on the other side of the gas catcher. In the CIDGC, ions are collected and transported toward the extraction orifice using the 4-phase ion surfing in slipping mode. The ions are then injected into an RFQ ion guide section described in the next subsection.

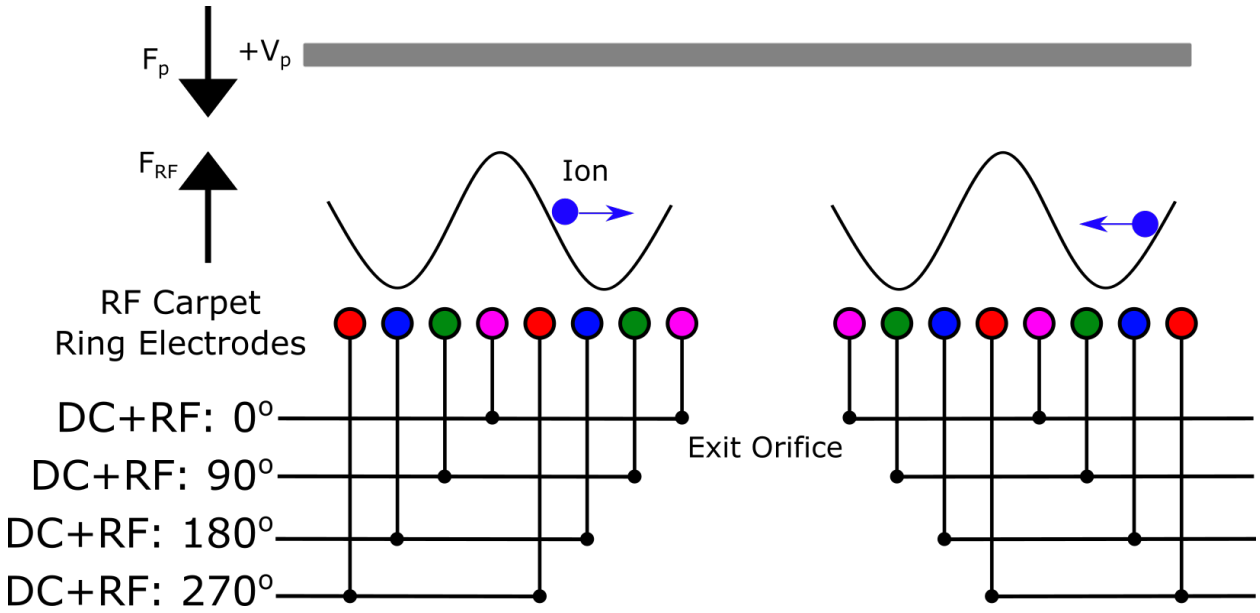

Figure 4.8: A conceptual drawing of how 4-phase ion surfing works.

4.2.1.3 RFQ Ion Guide

After extraction through the RF carpet, the ions are injected into a series of two RFQ ion guides, separated by a differential pumping barrier. The RFQ ion guides are constructed from rectangular PCBs made of Rogers 4003 material by Advanced Circuits. Each rectangular rod is 148.92 mm long, 8 mm wide and 1.57 mm thick. The conceptual drawing for the RFQ ion guide can be found in Fig. 4.9. Fig. 4.11 shows an example of the RFQs installed on the back face of the Shapal material. RFQs have historically been used in mass spectrometry, such as in SID. Similarly to RF carpet operation, RF signals are generated by AFGs and sent through RF amplifiers and resonant driver circuits before applying them to the RFQ. The driver circuit diagram can be found in Fig. 4.10. A DC potential difference is also applied along the four RFQ legs to transport ions from one end to the other.

The theory behind RFQ operation is based on Mathieu stability, governed by two Mathieu parameters a_z and q_z, defined in Ref. [133]. These parameters depend on the RF frequency, mass/charge (A/Q) ratio of the ions, size of the ion trap, RF amplitude and DC amplitude.

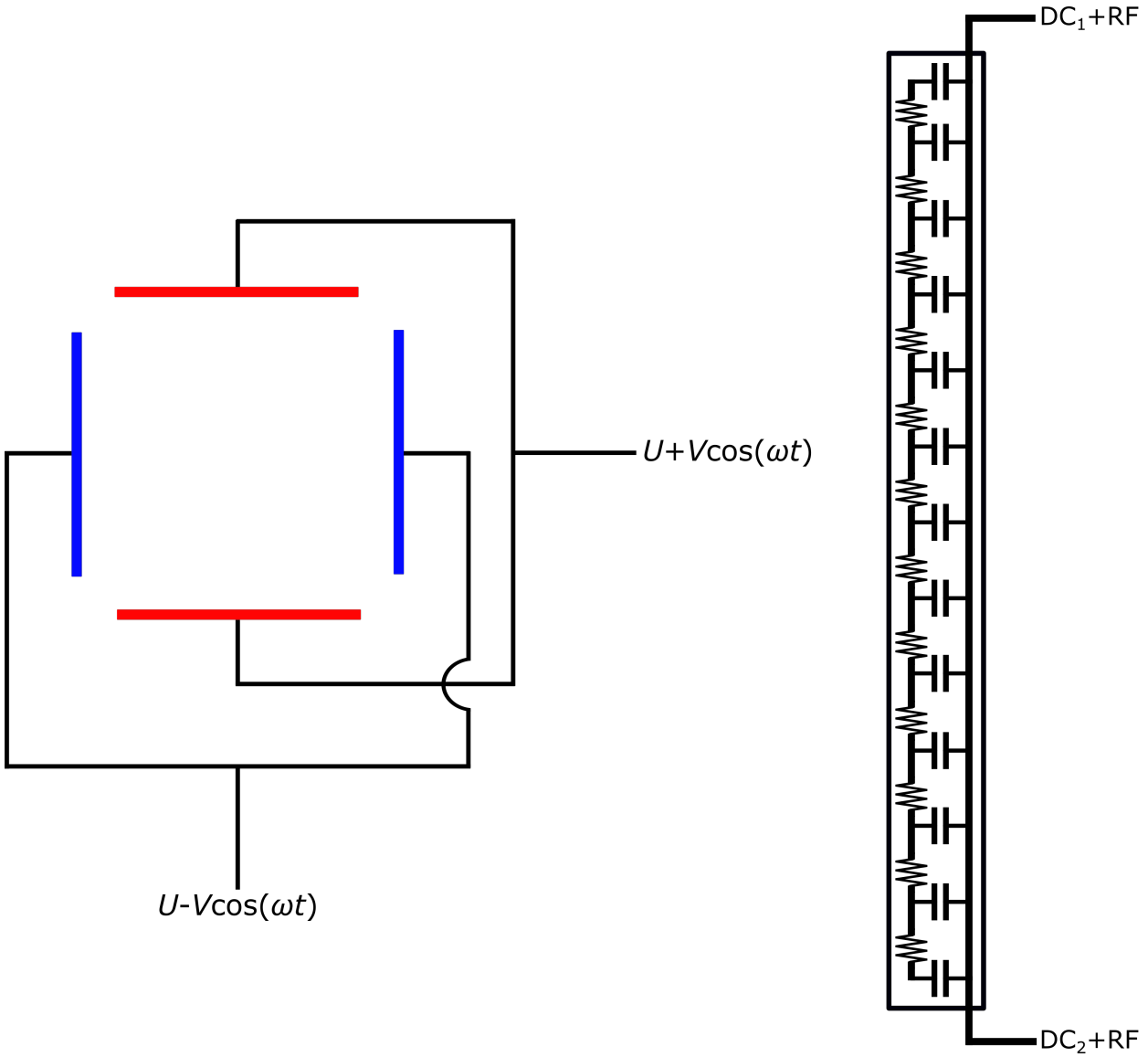

Figure 4.9: A conceptual drawing of the voltages applied to the RFQ and the circuit diagragm for the segmented flat RFQ. U is the DC potential applied across the length of the RFQ, V is the RF amplitude and ω is the angular RF frequency.

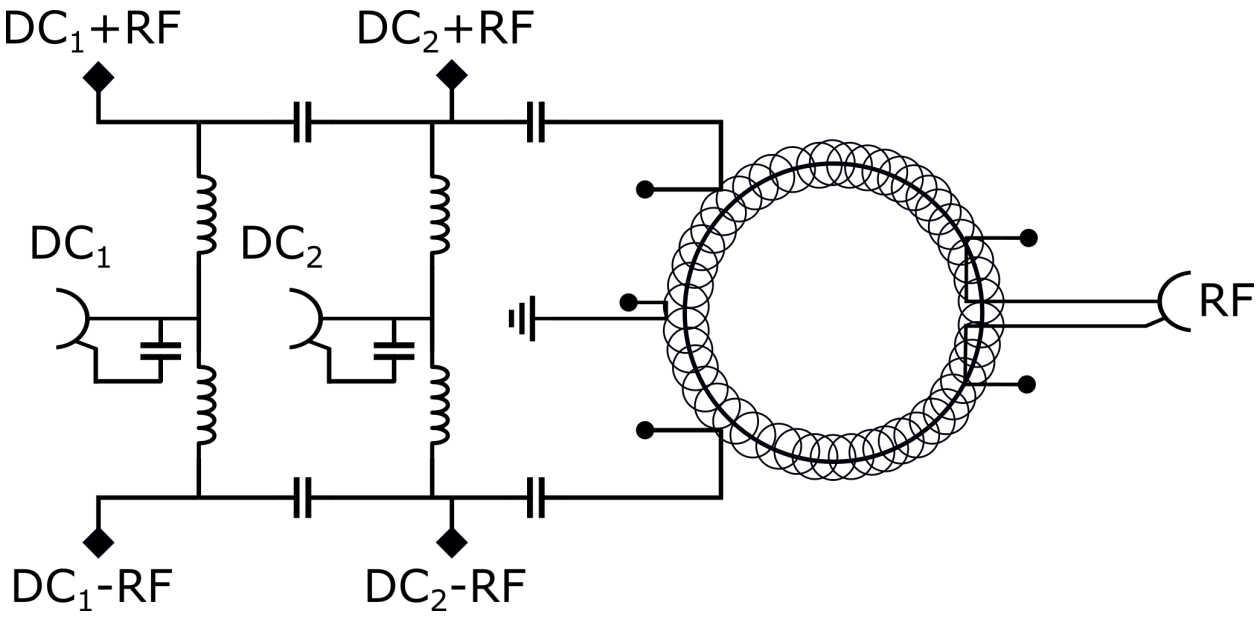

Figure 4.10: A circuit diagram for the RFQ ion guides. The RF and DC voltages are fed and mixed in together before supplying the signal to the RFQs via a toroid. The circuit can turn the RFQ into a trap by applying a third DC potential where the ground is.

For the purposes of this setup, the a_z parameter is 0 since the RFQ is not being operated as a mass filter, and a large range of different ions with unique A/Q can traverse the length of the RFQ ion guide. The RFQ ion guides were optimized for potassium ion transport during commissioning tests. The diameter of the pumping barrier is 1.5 mm and creates a pressure differential by two orders of magnitude (mbar vs $10^{-}3$ mbar). The differential vacuum is necessary for the proper operation of the residual gas analyzer, which sits after the second RFQ ion guide.

4.2.1.4 Residual Gas Analyzer (RGA)

A commercial Residual Gas Analyzers (RGAs) SRS 300 amu RGA was used for measuring the intensity of different ions either in the residual background or those that are injected into the CIDGC. The RGA comes with an ionizer for creating ions from the gas to be analyzed. For the purposes of our measurement, however, the ionizer was removed to install the RGA

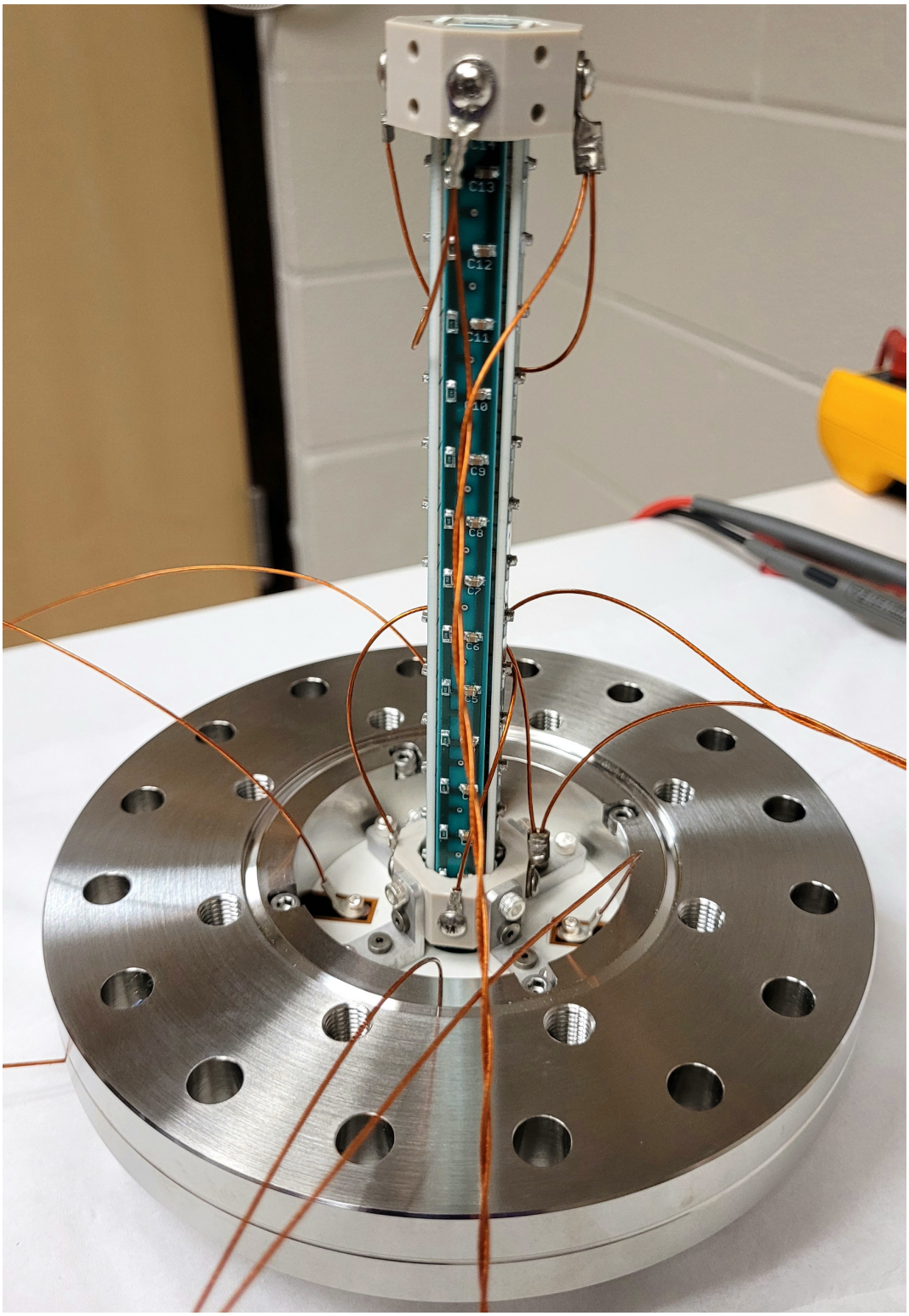

Figure 4.11: The first section of the RFQ ion guide installed on the other side of the RF carpet. The RFQs are held together with custom PEEK housing.

in the beamline. The utilities provided by the SRS RGA are as a mass spectrometer, a single gas monitor and a total pressure gauge. The RGA operates as a single gas monitor by measuring the pressure (or current) of a specified A/Q as a function of time. This is useful for tuning elements upstream the beamline, such as the RFQ ion guides and the ring electrode system in the cell, to optimize cations entering the RGA for analysis.

4.2.1.5 Final Installation and Vacuum System

The CIDGC setup has been constructed. Fig. 4.12 shows the gas cell installed at the end of the first d-line extension port. The pressure in the cell is measured with a manometer that controls the flow of gas into the main chamber. Pirani gauges were also used to measure the pressure as well, where they measured both the pressure in the main cell and the second RFQ ion guide section. The CIDGC sections were pumped down using scroll pumps and a molecular turbopump to provide the necessary pressure to operate the RGA with single mass resolution in the mass filtering mode with up to 5 mbar in the stopping cell.

4.3 Simulations

4.3.1 Si_3N_4 Membrane SRIM Transmission Simulations

An important aspect of the CIDGC is the transmission through the Si_3N_4 membrane, which is responsible for dissociating the incoming molecular beam (molecular ion of interest and other contaminants) and separating the gas cell from upstream vacuum systems. The efficiency with which ions transmit through Si_3N_4 membranes will be impacted by several parameters such as membrane thickness, beam energy, and the size and atomic number of the ion or molecule. These transmission studies can be estimated using a simulation program

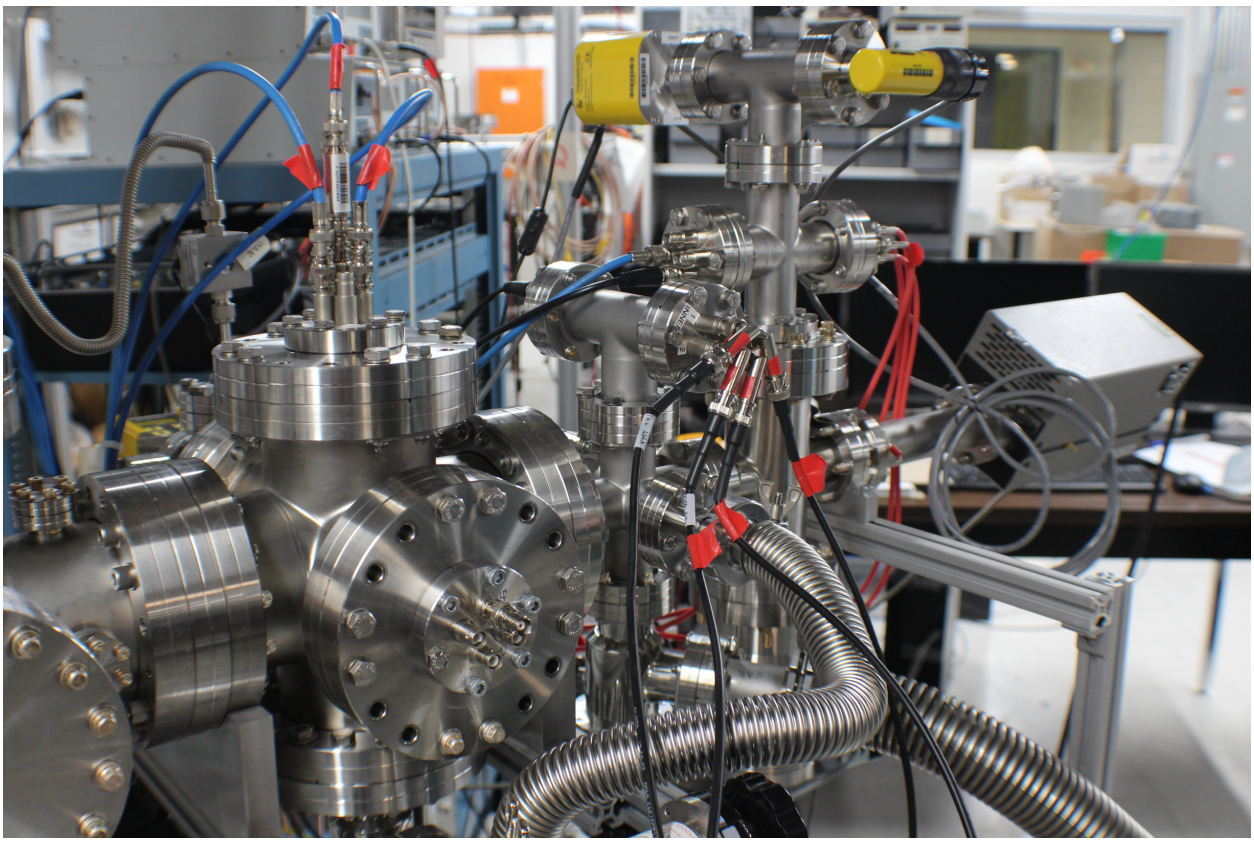

Figure 4.12: The complete CIDGC installed at the end of the first port in the d-line extension. The gas catcher, two RFQ sections and the Residual Gas Analyzer. Vacuum gauges are also observable as well as the wires that connect to DC power supplies and the RF driver circuits.

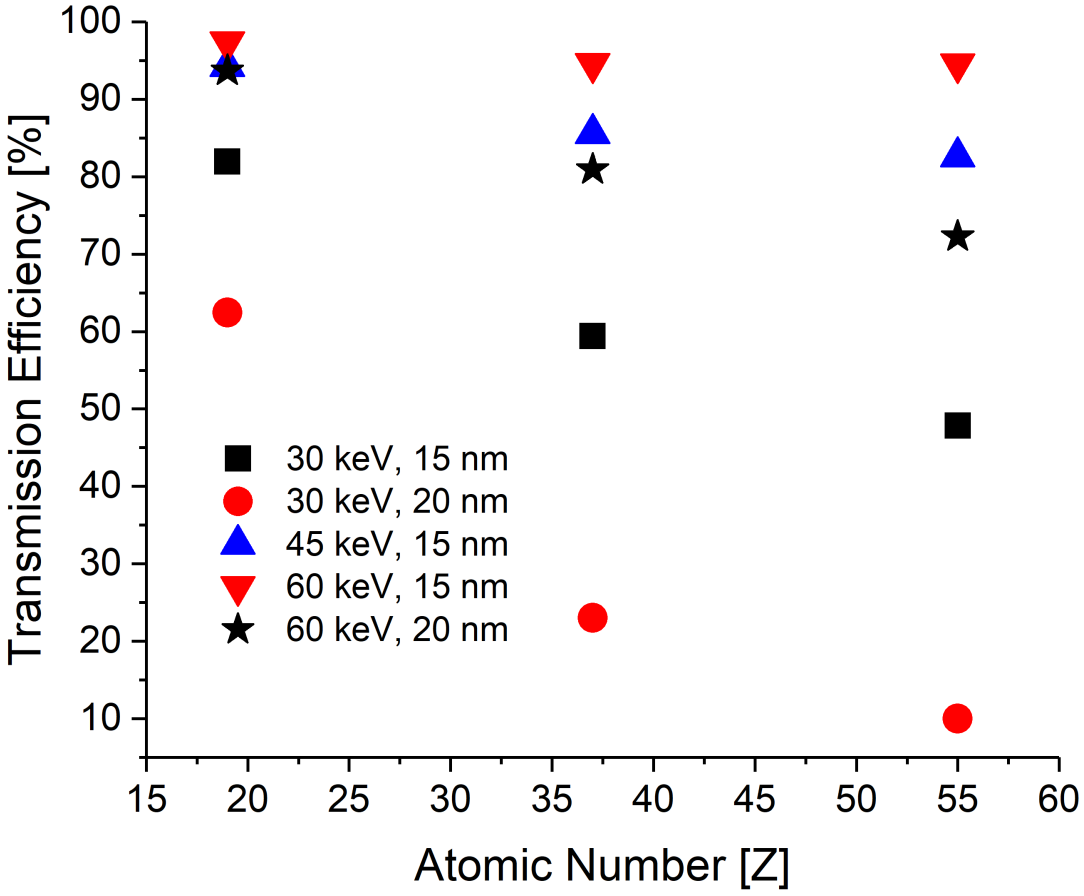

Figure 4.13: Results of SRIM calculations showing the stopping efficiency in 10 mbar helium of $^{39}K^{+}$, $^{85}Rb^{+}$, and $^{133}Cs^{+}$ for various Si_3N_4 window thicknesses and beam energies.

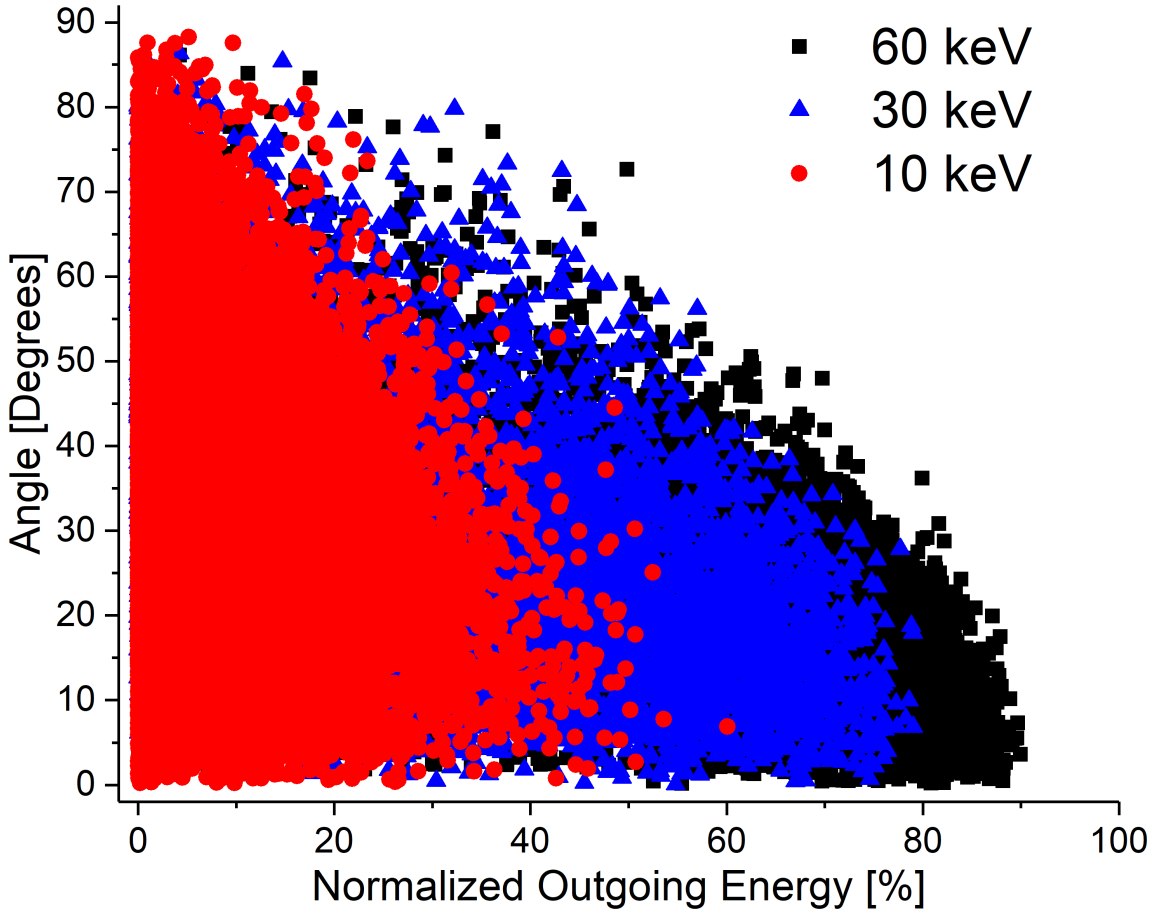

Figure 4.14: The scattering angle of transmitted ions as a function of outgoing energy of $^{39}K^{+}$ ions following transmission through a 20 nm Si_3N_4 membrane. The energy is normalized to the incoming beam energy of the ions. The different incoming beam energies show a dependence on scattering, where 10 keV highlights larger scattering with a smaller maximum amount of energy ions transmit with compared to 60 keV.

called SRIM, short for Stopping and Range of Ions in Matter [134,135]. The impact of mass, energy and membrane thickness on the transmission of atomic ions is shown in Fig. 4.13 for several cases.

Another quantity important to understand is the positions where the ions are stopped within the gas volume. The correlation that transmitted ions had with their scattering angle was examined, which will impact the losses observed in the gas volume. The results of these studies are found in figure 4.14. The larger scattering angle correlates with lower energy and

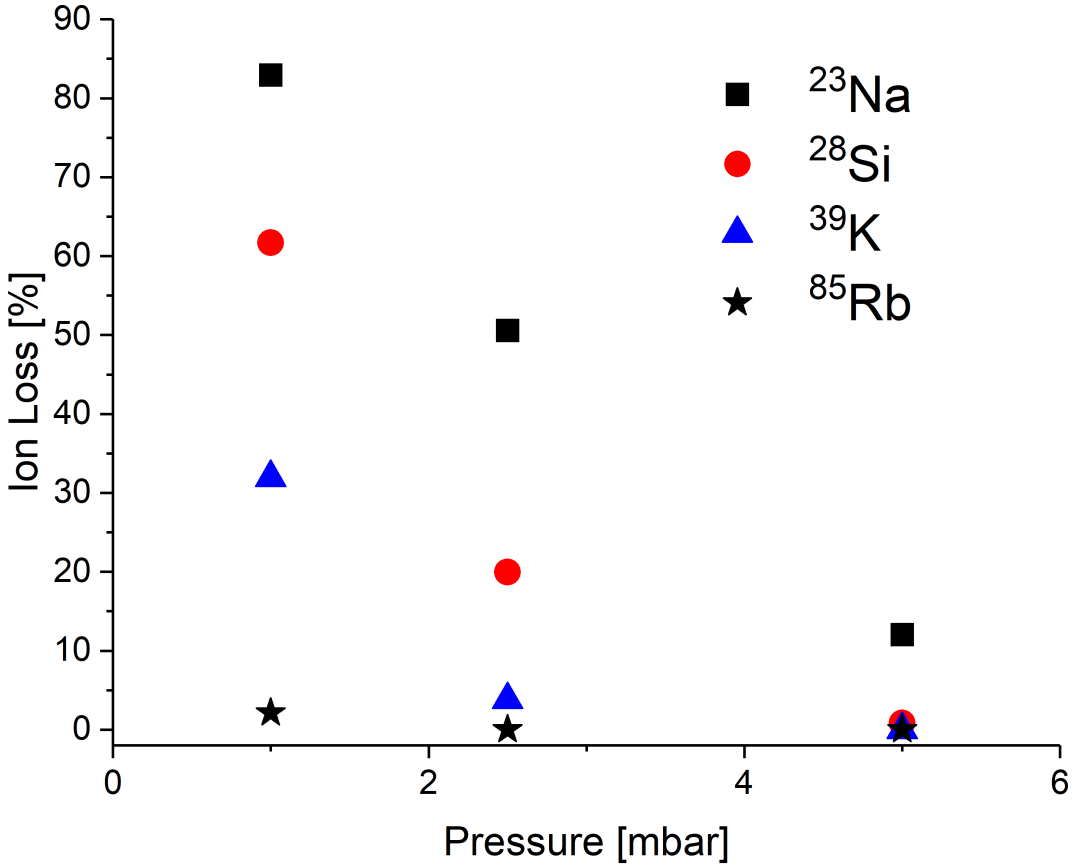

Figure 4.15: The ion losses as a function of pressure from simulated ions after transmitting through 21 nm of Si_3N_4 and getting stopped in He gas. The losses were defined the ratio of ions that are stopped beyond the dimensions of the inner diameter of the ring electrodes and the length of the cell between the Si_3N_4 membrane and the RF carpet to the total number of ions generated.

shorter stopping distance in the gas volume. This information can be used in subsequent simulations that explore how the ions travel after being stopped in the He gas. The results of the expected losses as a function of pressure for different masses can be found in Fig. 4.15. This is important to understand because the masses of some common contaminants are $A = 28$ (N_2), $A = 30$ (CO), and $A = 32$ (O_2). Even more, the dissociation products will have a lower mass, meaning the losses can be even more dramatic. This issue can be mitigated by increasing the volume of the cell in the future, as well as lining the internal wall with an RF carpet to prevent ions from being lost on the internal walls.

One of the drawbacks of SRIM is that only atomic ion beams can be used in simulations. This limits the applicability of SRIM for studying the transmission of molecules through the membrane. The program can still be used to understand different mechanisms, such as energy loss. Energy loss studies can inform what energies transmitting ions experience and used to predict the probability of dissociation for different ions. An example of predicted energy loss spectra from SRIM can be found in FIG. 4.16. Another aspect to consider is that SRIM was developed based on bulk material properties, not the microscopic level at which these membranes are fabricated. Therefore, the calculated transport efficiency can be understood to be of first order. Experimental information will be needed to verify the results obtained using SRIM.

4.3.2 Gas Catcher Ion Transport SIMION simulations

Simulations were performed to estimate the transport efficiency from where the ions stop in the gas to RF carpet. The electric field is created by biasing the copper rings using a resistor chain with two channels of a DC power supply connected to the first and last ring. The electric field is calculated numerically using the program SIMION [136] as ions travel

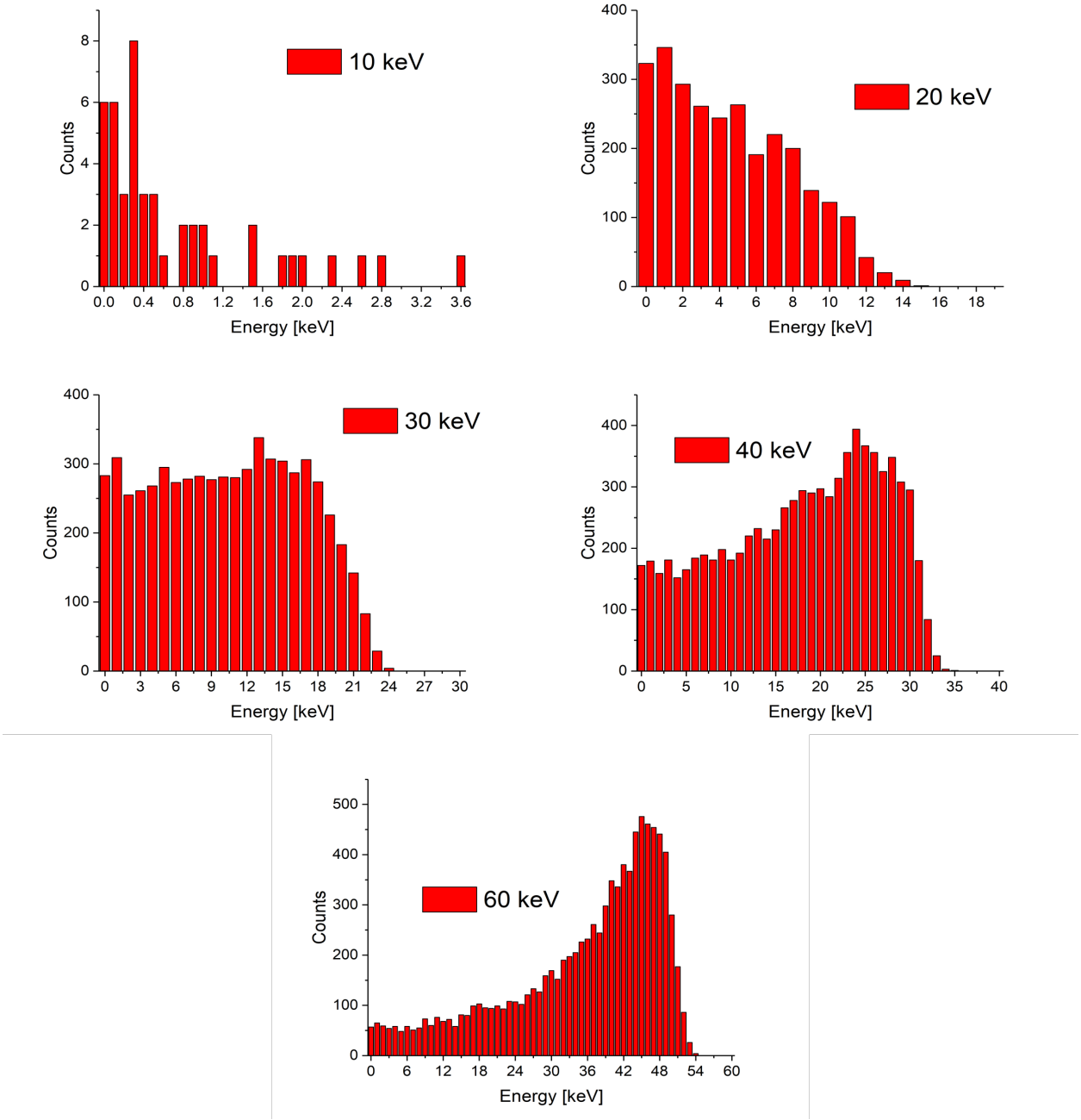

Figure 4.16: The energy distributions of $^{39}K^{+}$ ions generated and transmitted through a 20 nm thick Si_3N_4 membrane. As the energy of the incoming beam increases, the energy distribution of ions changes from a Poisson-like to a skewed Gaussian-like distribution. This data highlights the amount of energy deposited into the Si_3N_4 membrane during transmission.

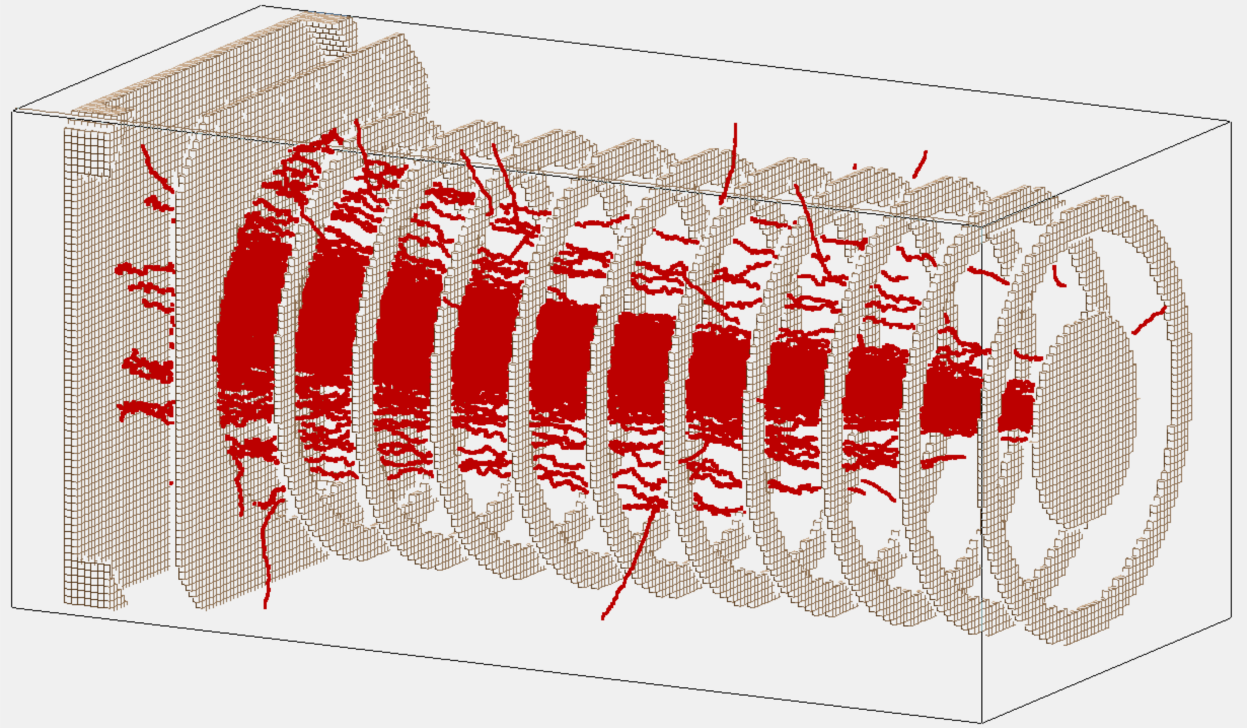

Figure 4.17: An example of the transport of $^{23}Na^{+}$ ions at a pressure of 5 mbar. As shown, most ions are successfully transported to the RF carpet.

through the simulated gas catcher. SRIM was used to determine the positions of stopped ions, with a sample of the ion's 3D positions imported into the ion workbench in SIMION. Ions whose final positions fell outside of the radius of the DC cage were considered lost on injection and were not included in the SIMION simulation. For reference, the fraction of ions that are lost during the stopping process can be found in Fig. 4.15.

The theoretical model for ion-neutral gas collisions used in these SIMION simulations was the hard-sphere model due to the low-pressure regime these studies were performed at [137]. In the hard-sphere model it is assumed that collisions are elastic between the ions and He gas. The motion of the He gas is treated as a neutral atom with no charge, where the velocity distributions for the He is given by a Maxwell-Boltzmann distribution. The model was calibrated using available reduced mobilities for ions that are well known [5–7] to ensure

that the collision cross-section was set at the appropriate value, using

$$K_0 = \frac{L^2}{V t_d} \frac{P}{760} \frac{273}{T} \text{ cm}^2 \text{ V}^{-1} \text{ s}^{-1}, \tag{4.2}$$

where L is the length the ions travel, the potential difference V applied across L, the time of flight t_d, and the pressure P and temperature T of the gas. Table 4.2 shows the calculated cross-sections determined by the reduced mobility simulations performed using SIMION. An example of the model used to measure the gas transport efficiency can also be found in Fig. 4.17. Results for these simulations can be found in Fig. 4.18. The results of the simulations show that there is no dependence on the mass of the ion as the transport efficiency is 86.2%(12) on average.

Species	Reduced Mobility (cm^2/V s)	Cross-section (m^2)
^{23}Na	22.35	3.14×10^{-19}
^{28}Si	20.527	3.48×10^{-19}
^{39}K	21.24	3.49×10^{-19}
^{85}Rb	19.75	3.16×10^{-19}

Table 4.2: Collision cross-sections for different species based on the calculated reduced mobilities found in Ref. [5–7]. The cross-sections were then used in the SIMION calculations for gaseous environments to recreate realistic environments.

4.3.3 RFQ Ion Guide SIMION simulations

The RFQ Ion Guide simulations aimed to understand the losses experienced for different diameters for the differential pumping diaphragm installed. Similar to the simulation described in the previous subsection, the model was created using SIMION, and the hard-sphere model was used to simulate gas collisions in both RFQ ion guide sections. The two sections were set to different pressures based on measured values. For example, if the gas catcher was at

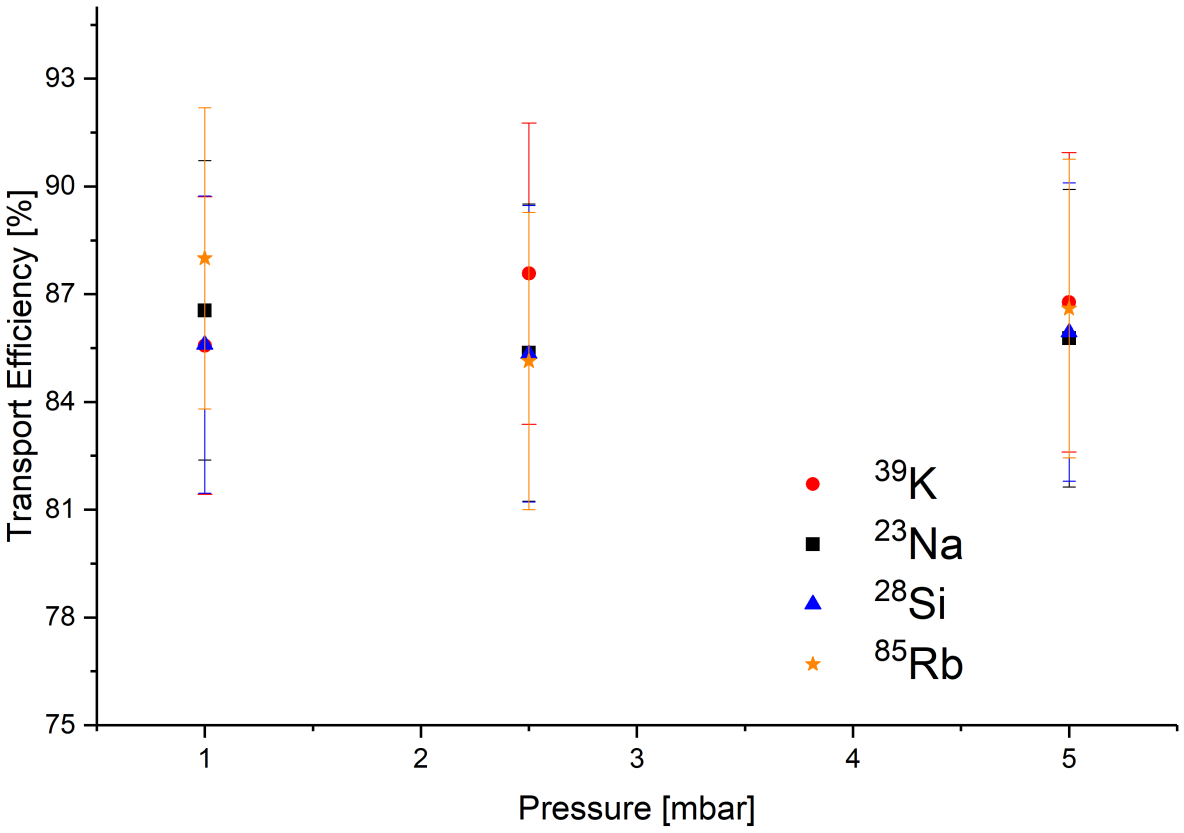

Figure 4.18: The transport efficiency of ions as a function of the gas cell pressure. No clear dependence is observable for different masses simulated based on the final positions calculated by SRIM.

2.5 mbar, the first RFQ section was calculated to be 0.25 mbar and the second RFQ section pressure was measured at 10^{-3} mbar. The pressure in the first section was calculated using the flow rate through the RF carpet orifice and the pumping speed of the vacuum pump. Based on the calculation, the pressure is calculated to be an order of magnitude smaller than the pressure in the gas cell due to the small aperture in the RF carpet extraction hole. In the simulations, the RF was scanned to understand the impact of different diameters on the transport efficiency. Generally, the parameters showed an improvement for deeper trap depth and larger orifice diameter. The diaphragm potential between the two RFQs was also investigated to optimize ion transport.

4.4 CIDGC Experimental Studies and Characterization

4.5 Si_3N_4 Transmission Studies

While SRIM can make quite reliable predictions about transmission through bulk materials, there is very little experimental data that SRIM can base its microscopic range computations on. This limitation of SRIM motivated transmission measurements of the Si_3N_4 membranes, which also provides a measure of the thickness as well. A test stand was developed to take beams from BMIS, consisting of three plates for electron suppression and current measurements followed by a Channel electron multiplier (CEM), or channeltron by Photonis known as the MAGNUM™ Electron Multiplier [138]. The channeltron counts the number of ions that transmit through the Si_3N_4, and was measured with an Agilent 53131A 225 MHz Universal Counter. The test stand can be found in Fig 4.19.

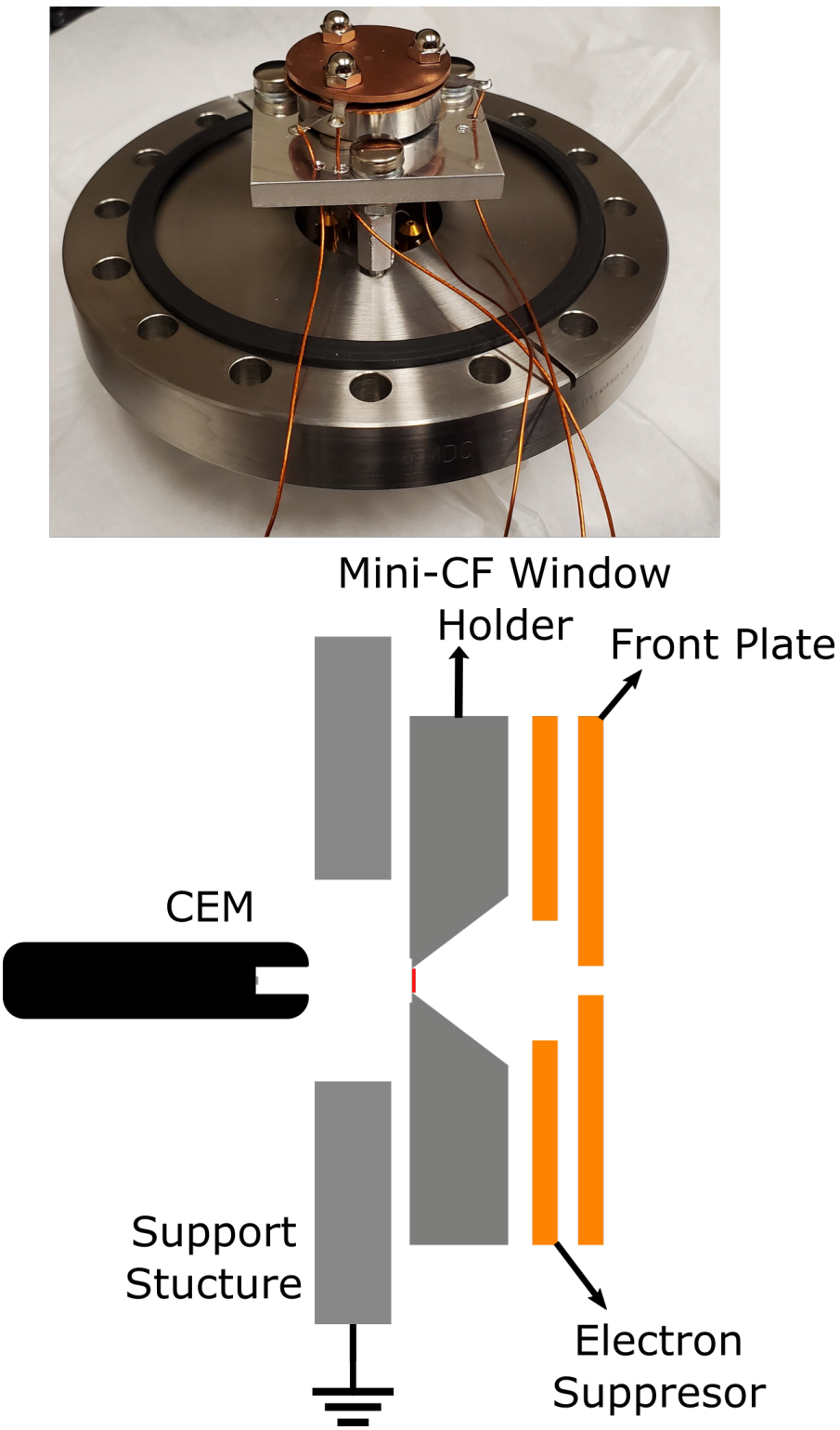

Figure 4.19: A photo and illustration of the test stand used to measure the experimental transmission efficiencies of the Si_3N_4 membrane. The elements were isolated using PEEK screws and PEEK washers. The three front plates were biased while the support structure was held at ground while the CEM was operated at 2450 V.

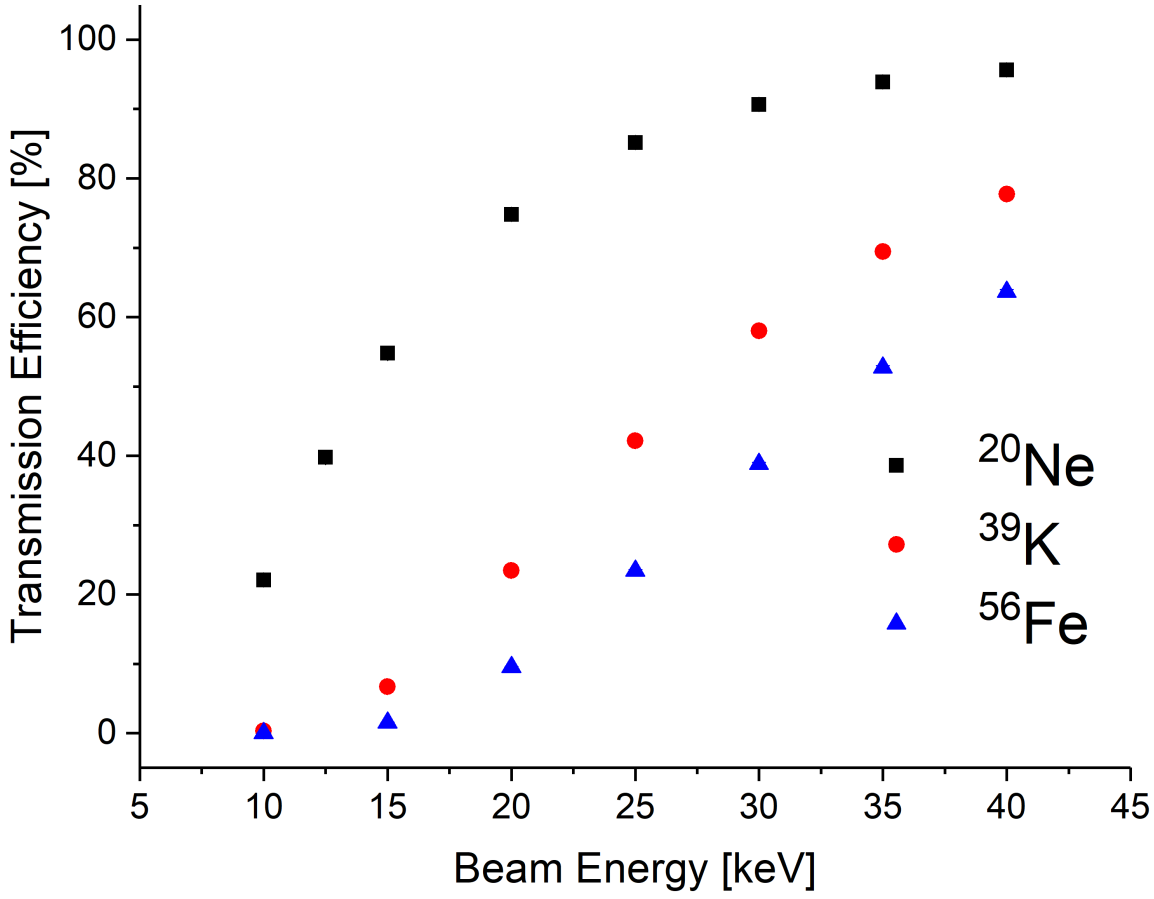

Figure 4.20: Transmission efficiency calculations for multiple species as a function of incoming beam energy performed through a 21 nm thick Si_3N_4 membrane.

The tests involved measuring the current on the first plate. Beam current was adjusted to be in the nanoampere to picoampere range using attenuators in the beam line. Even with only a few picoamps of beam, the CEM was still sensitive to current directly entering the counter since ions that didn't enter the CEM at an angle didn't produce an electron shower. This meant that some of the beam could only be measured on the CEM while the other portion of the current was measured on the first plate. To minimize ions striking the mini-CF that housed the window and electron suppresor, the aperture of the first plate was only 1 mm in diameter. A scaling factor was then extracted from the attenuators to translate the ions counted in the CEM into a current to compare to the measurement performed on the front plate. Several measurements were taken with $^{9}Be^{+}$, $^{20}Ne^{+}$, $^{23}Na^{+}$, $^{39}K^{+}$ and $^{56}Fe^{+}$. The energies investigated were between 10 - 45 keV based on what was simulated in SRIM as observed in figure 4.20.

All beam species that were measured using the CEM showed increased transmission through the membrane with increased beam energy. A separate scaling factor for the CEM was assumed for the raw efficiency based on initial measurements of $^{20}Ne^{+}$, as observed in figure 4.21, since the transmission efficiency didn't increase after 35 keV. This scaling factor was applied to the other species measured during the experiment campaigns to identify what the transmission efficiencies were for other species. Initial results show how the trend for the transmission efficiencies followed an expected behavior and also agreed with the SRIM calculations. However, in subsequent online measurements, measurements for the same species on different occasions did not yield consistent results. Issues that could have contributed to these inconsistencies could contribute from either deformations forming in the Si_3N_4 or a change in the beam optics between measurements. Additional investigations will be needed to understand this findings.

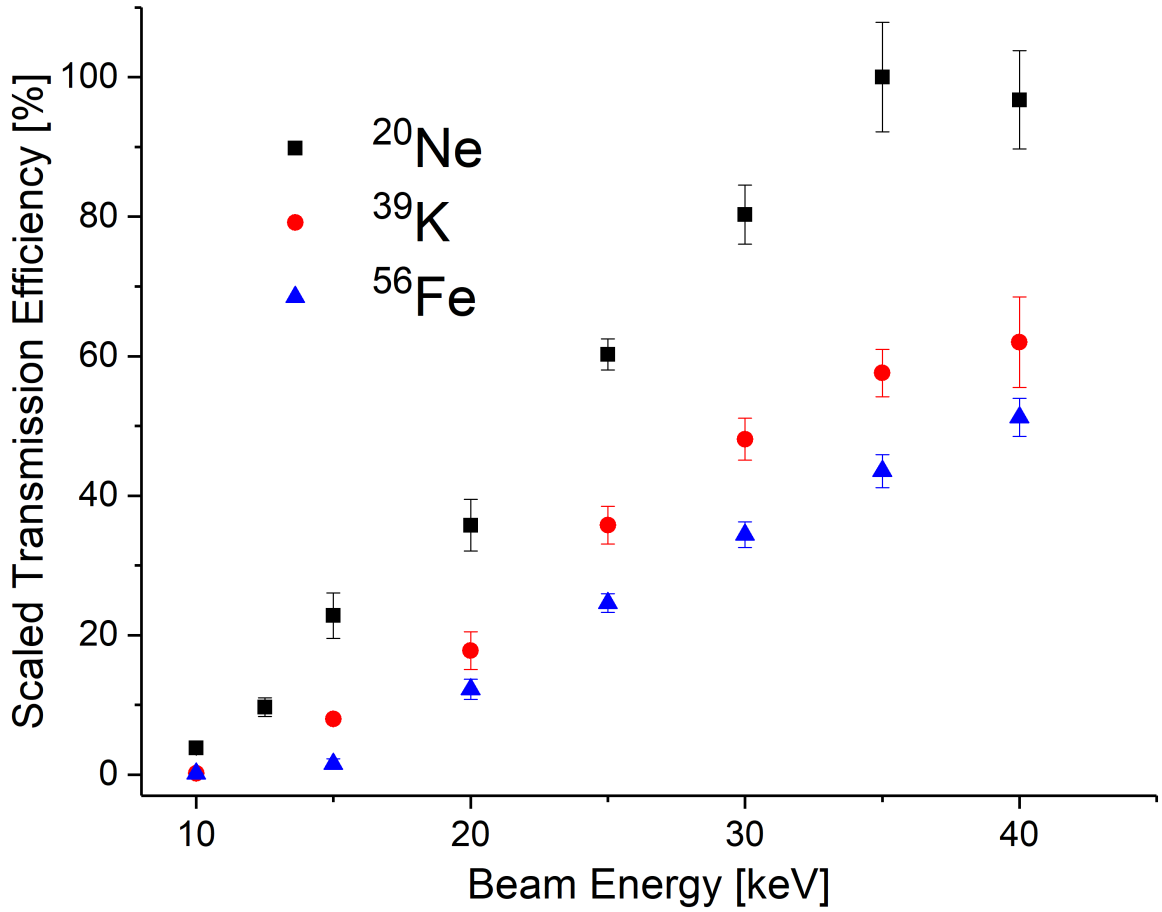

Figure 4.21: Scaled transmission efficiencies for different species delivered from BMIS. The $^{20}Ne^{+}$ data shows a plateau beginning at 35 keV while $^{39}K^{+}$ and $^{56}Fe^{+}$ continue to increase.

4.5.1 RF Carpet Characterization

The transport efficiency of the RF carpet was investigated. For these tests, the Si_3N_4 window was replaced with a potassium ion source [139] and the RFQ ion guides were replaced with a collector plate that acts as a Faraday cup. An illustration of the internal structure with the Potassium ion source can be found in Fig. 4.22. After verifying that the RF carpet was operating as expected, the collector plate was replaced with the RFQ ion guide rods to perform the characterization tests. The parameters investigated were the RF frequency and amplitude, the helium buffer gas pressure, push plate potential, and incident ion current. The incident ion current that reached the RF carpet from the ion source was determined by switching the direction of the traveling wave so that ions were transported to the retaining ring where the current was measured.

The pressure was investigated to understand the RF amplitude needed to surf ions effectively since lower pressures can lower the damping effect of ion motion. The 1-5 mbar pressure regime is ideal since most ions will be stopped in the volume and low pressure will also provide faster transport. The results for the pressure studies can be found in Fig. 4.23. Based on the results, the RF carpet can be operated down to a pressure of 0.75 mbar before ion surfing efficiency starts to suffer at the given parameters.

As discussed before, one of the parameters that can directly impact the efficiency of ion surfing is the push field generated to push the ions toward the surface of the RF carpet. The results of two push field studies are found in Fig. 4.24. As expected, a larger push field generated by the potential on the last ring required more RF to effectively transport the ions to the extraction orifice.

The RF frequency can also impact how efficiently an RF carpet can transport ions to the

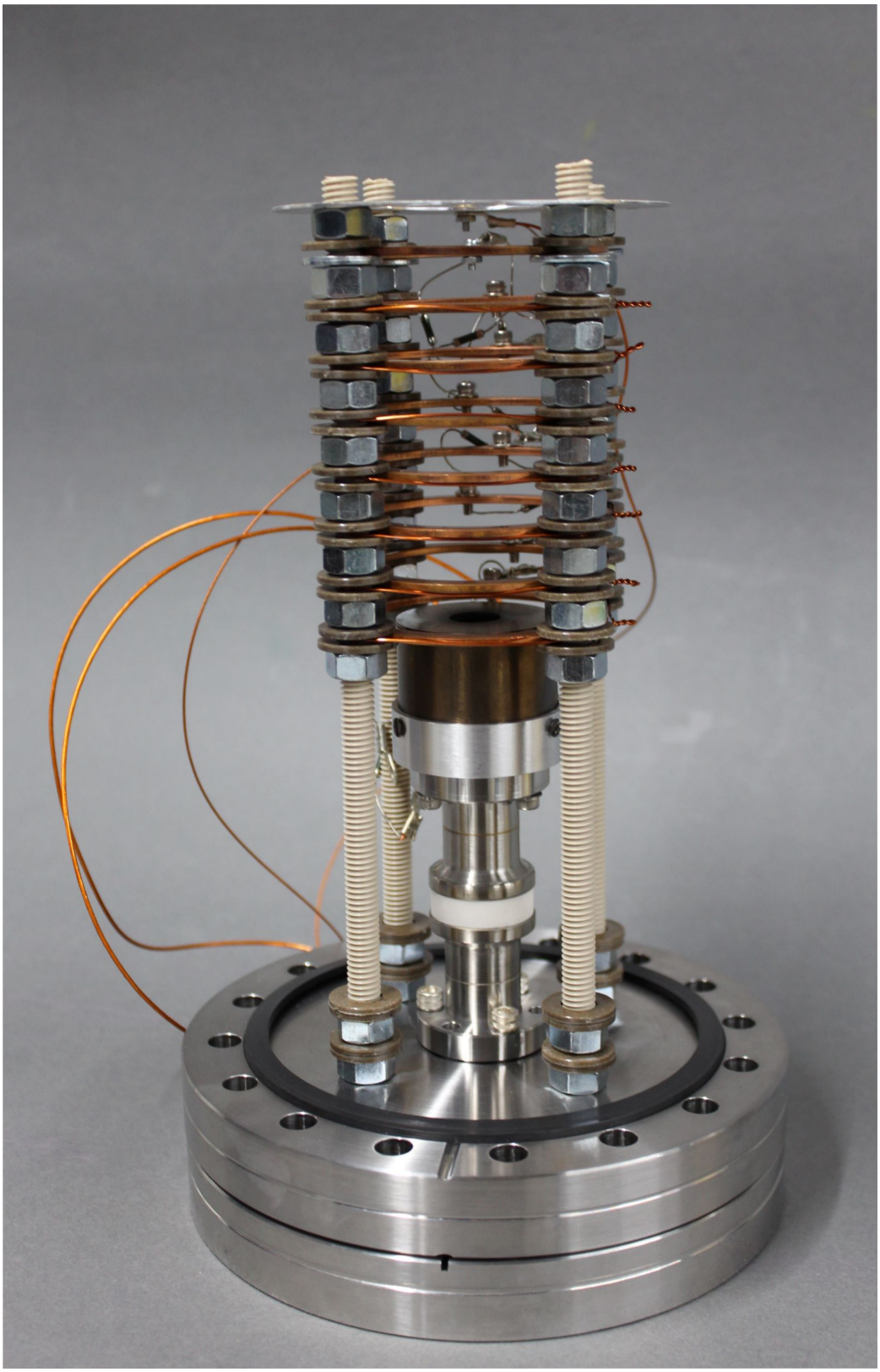

Figure 4.22: The internal structure of the gas cell that was configured for characterizing the CIDGC using a ^{39}K ion source.

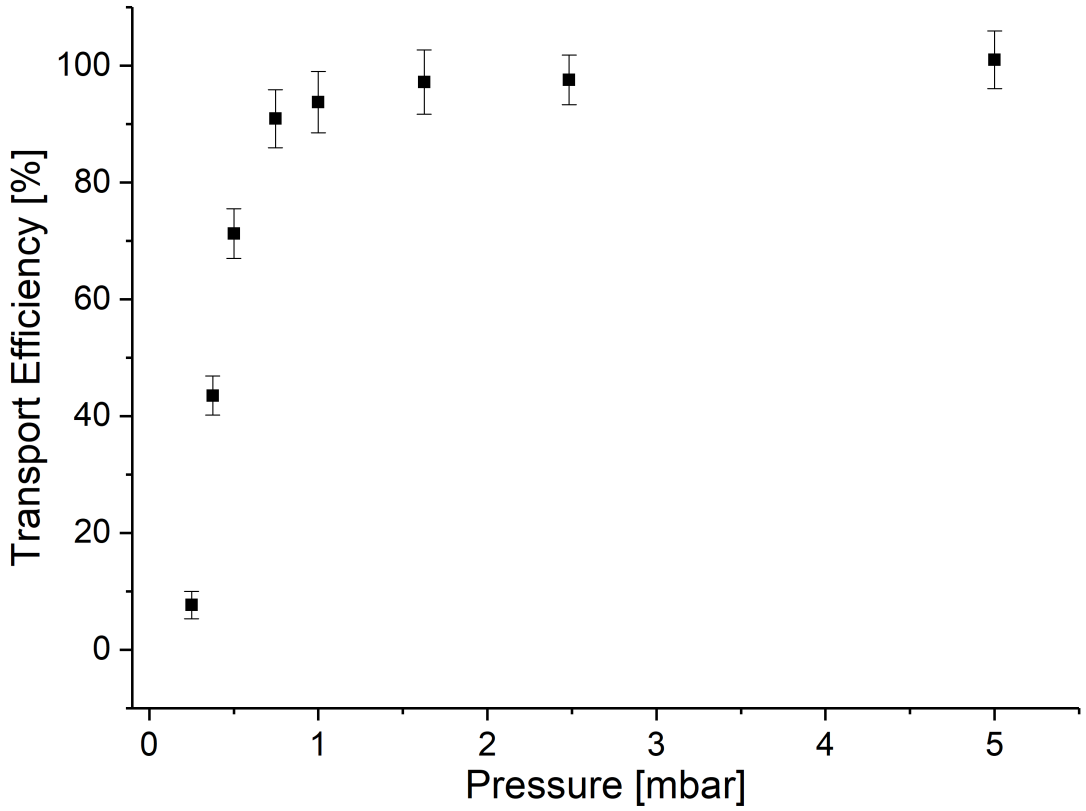

Figure 4.23: The transport efficiency as a function of the pressure for 4-phase ion surfing. The RF carpet was operated at 3 MHz with an amplitude of 90 Vpp at a current of 150 pA.

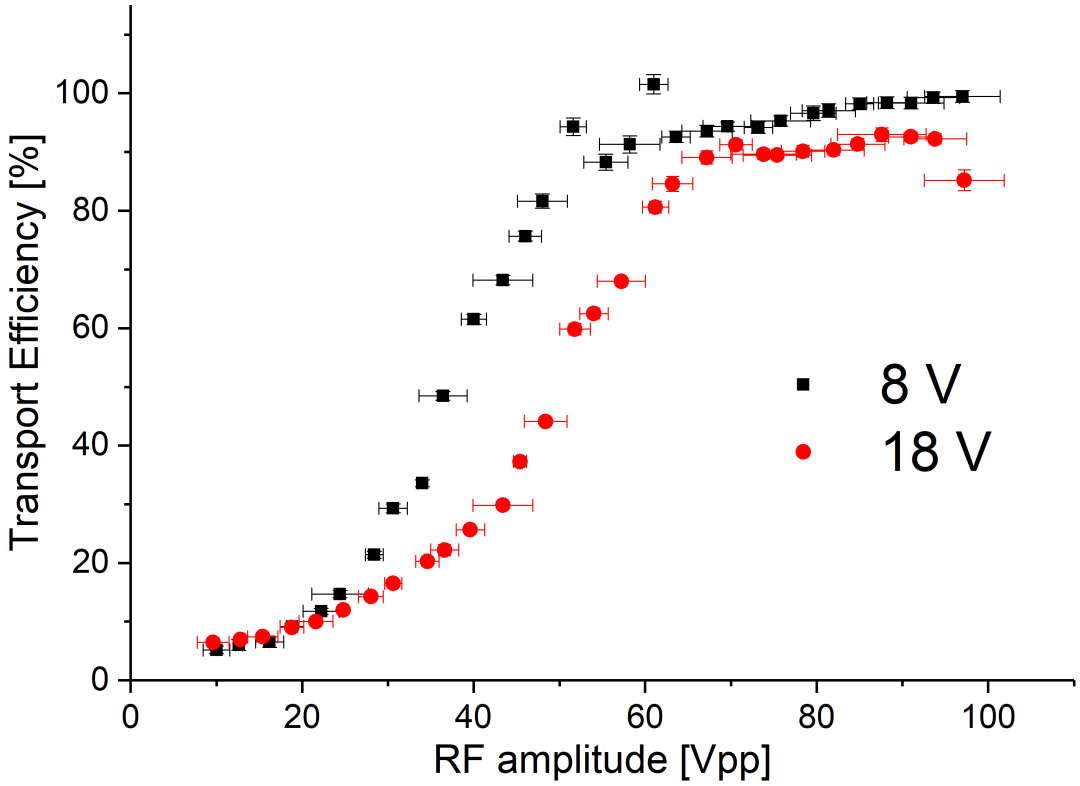

Figure 4.24: The dependence of the push plate voltage on the transport efficiency of the RF carpet. Higher push plate values translate into higher RF amplitudes necessary to transport the ions to the extraction orifice. The measurements were performed at 3 MHz with a current of 1.5 nA at 1 mbar.

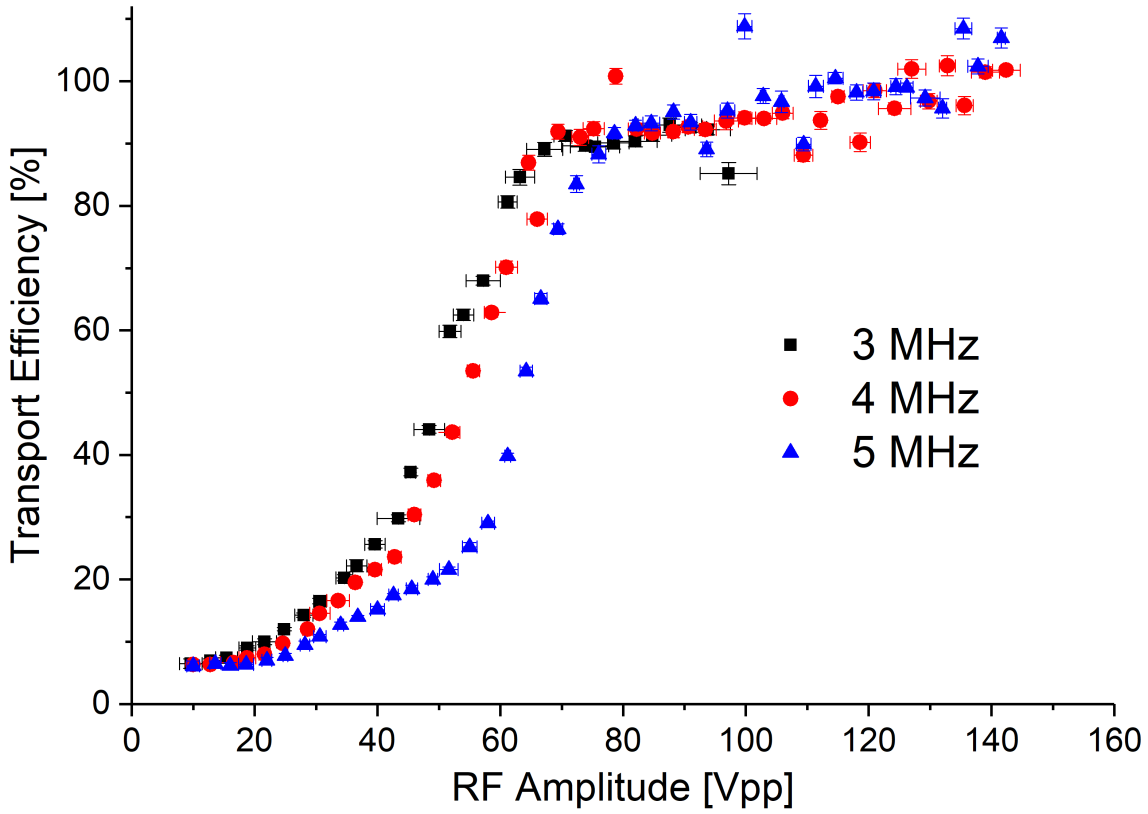

Figure 4.25: Transport efficiency measurements performed with the circular RF carpet at a pressure of 1 mbar and a current of 1.5 nA. The efficiency needed to transport ions shows a frequency dependence, with 3 MHz being more efficient than 5 MHz.

extraction orifice. The results for such frequency measurements can be found in Fig. 4.25. For higher RF frequencies higher RF amplitudes are necessary to transport the ions efficiently. One of the limitations of these measurements has been the range in frequency available to investigate this dependence due to the resonance width of the driver circuitry. In the future, studies should be conducted at lower frequencies by adding capacitance to the system

The current measured outside the carpet can provide information on how space charge impacts the carpet's ability to surf ions. Space charge effects increase with larger beam currents, which translates to a larger RF amplitude necessary to transport ions. Space charge also increases with increasing pressure in a gas catcher [140]. The impact space

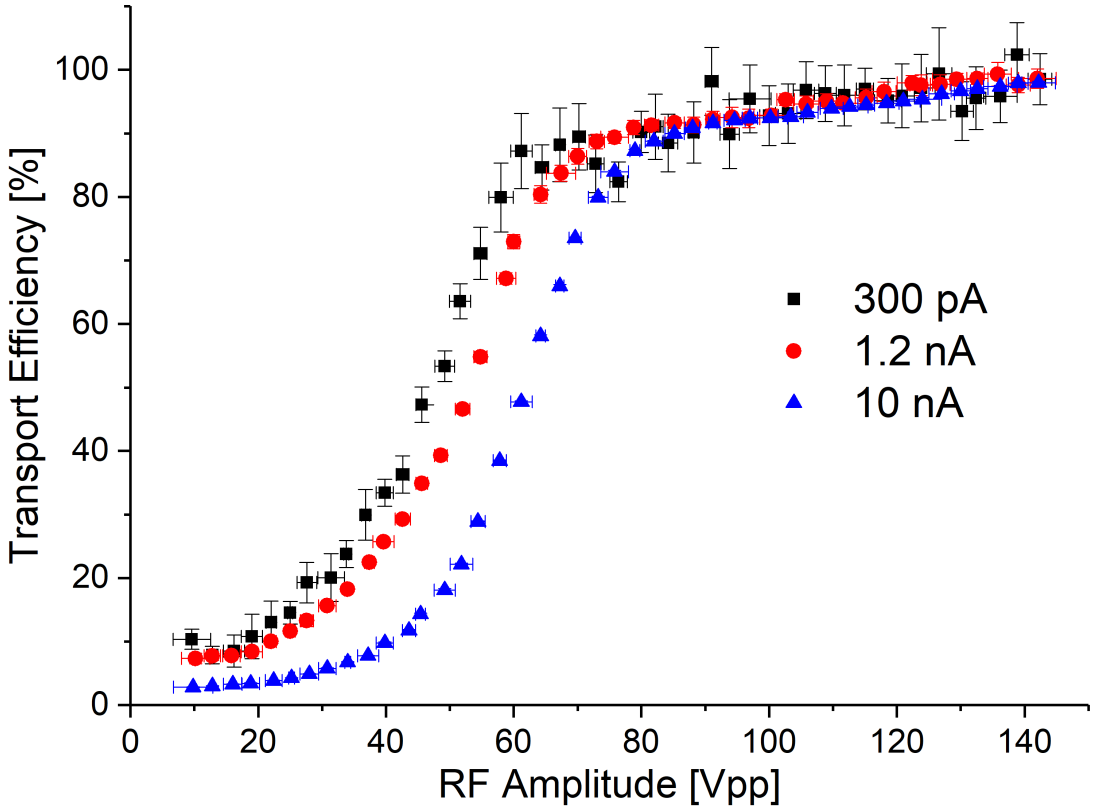

Figure 4.26: The transport efficiency as a function of RF amplitude for different incoming currents to investigate the role of space charge. The carpet was operated at 3 MHz at a pressure of 2.5 mbar. The offset observed at lower currents results from a measured current of ions that pass directly through the orifice without surfing.

charge has on ion surfing can be seen in Fig. 4.26 for the circular RF carpet. More RF was needed to drive the ions to the extraction orifice for higher extracted beam currents.

These initial measurements show that the RF carpet can be operated as expected, with the ions moving in slipping mode based on the speed which maximum transport efficiency is reached at the frequency these tests were performed at. The results obtained also show that higher RF amplitudes are necessary for the 2-phase RF 4-phase AF ion surfing method, confirming that the 4-phase RF ion surfing is more efficient.

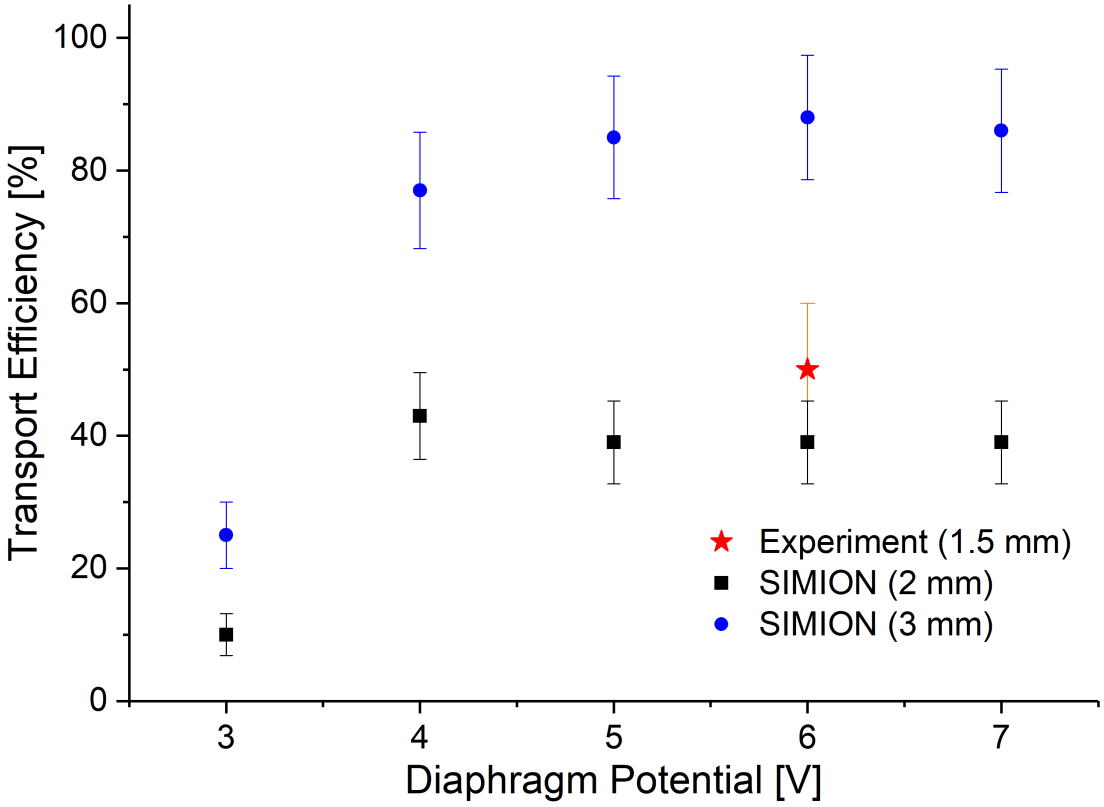

Figure 4.27: Diaphragm potential studies performed using $^{39}K^{+}$, with the RFQs operating at 1.2 MHz to understand the impact of the orifice diameter and diaphragm potential on ion transport. Good agreement between experimental data and simulated results was observed.

4.5.2 RFQ Ion Guide Characterization

Potassium ions were extracted from the RF carpet and transported along both RFQs to characterize the parameters needed to optimize transport through the diffusion pumping diaphragm. The RF amplitude was adjusted for optimal stability in-flight, with the first RFQ frequency set to 1.185 MHz at an amplitude of 130 Vpp. The second RFQ resonant frequency was found at 1.263 MHz at 150 Vpp. The results were compared to experimental data that was collected for an orifice potential where good transport was observed using an alkali ion source as described in the next section. The results of these diaphragm simulations and their comparison to experiment can be found in Fig. 4.27.

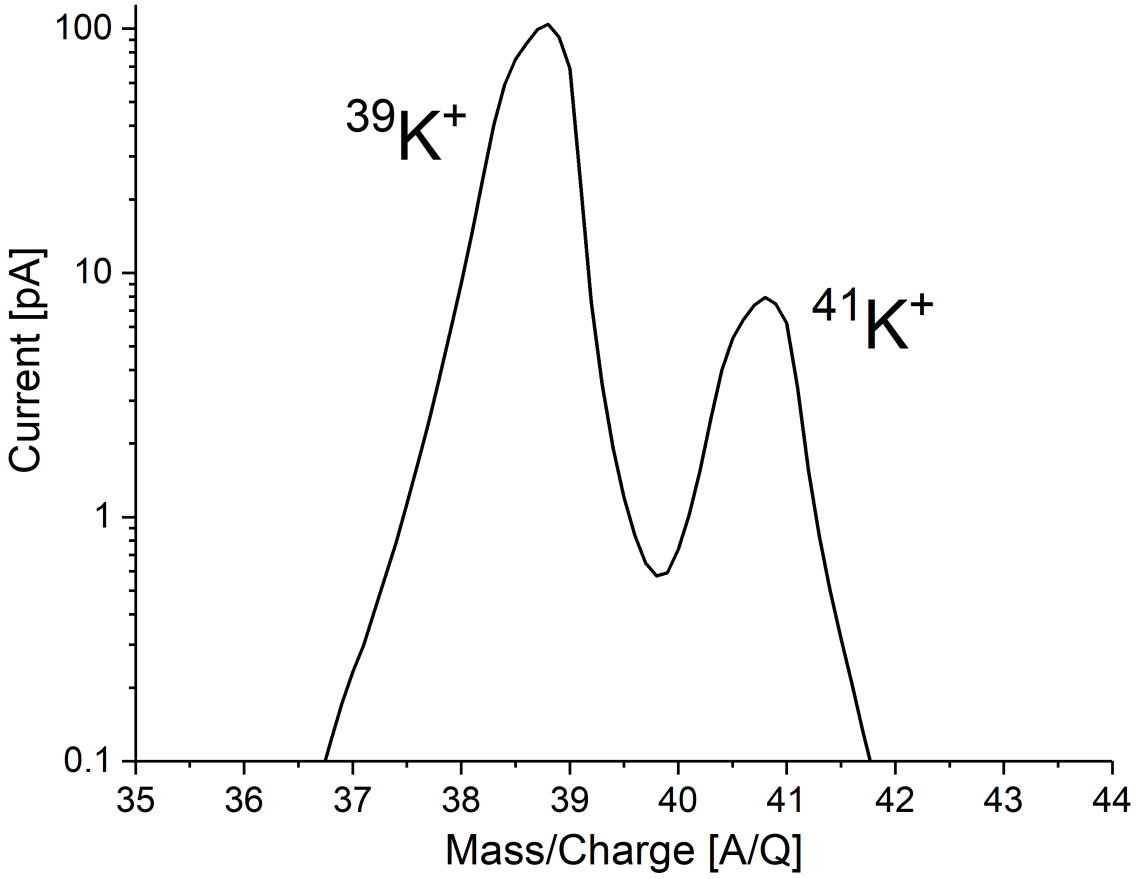

Figure 4.28: The spectrum produced using the RGA in the mass filtering mode. Both peaks for the isotopes of Potassium can be found, and the results match the natural abundance ratio observed in the spectrum. The RGA was operated at $1 \times 10^{-}3$ mbar with the gas cell at 2.5 mbar.

4.5.3 Measurements with the RGA

Following extraction through the RF carpet and transport through the RFQ ion guides, the ion source was characterized in the RGA. The ion transport to the RGA through the RFQs was tuned using the RGA as a single gas monitor and optimized for transport through both the RFQs and the diaphragm. The Mathieu parameter q_z was also calculated to confirm that the RF amplitudes and frequencies of the ion guides were optimized. Afterward, the RGA was operated as a mass filter confirming that the two naturally occurring isotopes of

potassium are successfully transported to the end of the CIDGC. An example of this plot can be seen in Fig. 4.28.

4.6 Online Measurements and discussion of results

Measurements were taken with beam from the ANL gas cell using the sparker and from BMIS. The different species that were delivered to the CIDGC were NO, ^{61}Ni, and ^{39}K. The beam was delivered to the CIDGC area at 30 keV. Current measurements inside the gas cell showed evidence of ions transmitting through the membrane and creating He^+/e^- pairs.

The biggest challenge was transporting detectable amounts of current out of the gas catcher and through the RFQ ion guides. This process involved testing out different inductors on the RFQ driver circuit in Fig. 4.10 and measuring the current on the diaphragm. With the optimized inductors installed, The RFQs were operated at a resonant frequency between 1.2-1.4 MHz at an RF amplitude of 90 Vpp. Several hundreds of pA of beam were able to transport to the diaphragm, and injected into the RGA. When performing measurements using a $^{39}K^+$ beam from BMIS, there was no sign of ^{39}K ions extracted out of the gas cell. Water and other contaminant ions were observed at low currents at the RGA instead. The spectrum can be seen in Fig. 4.29. More time working with externally provided ion beams will be required in order to fully troubleshoot the system.

One effect that could have impacted the results is the possibility of neutralization during transmission through the Si_3N_4 membrane. Neutralization isn't expected since the incoming beam would collide with He atoms following transmission. However, studies [141] with singly charged ions transmitted through graphene foils showed that they were neutralized. Another

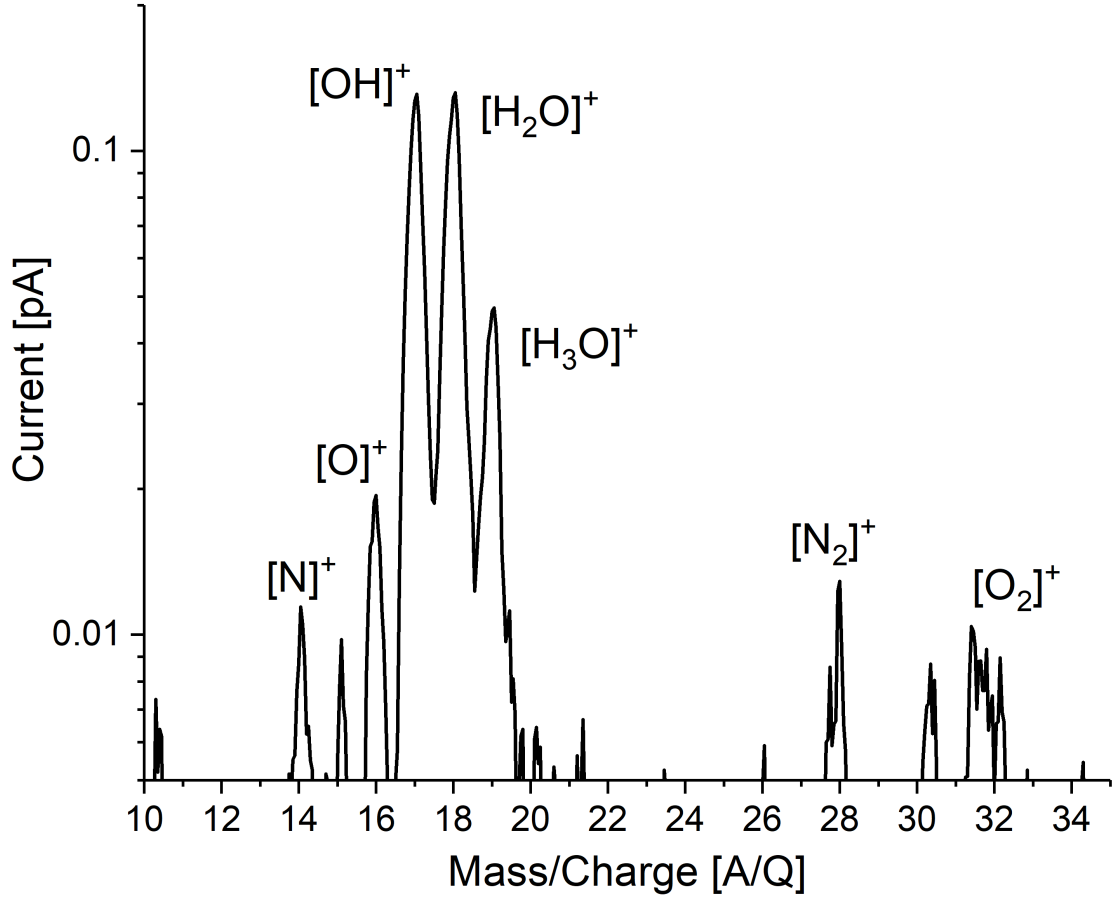

Figure 4.29: Mass spectrum of ions extracted from the stopping cell measured in the RGA with online $^{39}K^{+}$ beam from BMIS injected into CIDGC. Only major contaminants could be observed, such as water, oxygen and nitrogen.

group at Argonne National Laboratory measured similar results while investigating their usage as an entrance membrane for a low-energy gas catcher [142]. Similar measurements should be performed to study the role Si_3N_4 have on generating different charge states following transmission. This information would provide a necessary constraint on whether or not this gas catcher is feasible.

Assuming that neutralization isn't happening, several improvements can be made in future iterations of the CIDGC. Due to the large losses observed for low-mass species in the SRIM simulations, RF strips can be installed on the inside of the gas catcher to prevent ions from striking the walls. Losses on the vacuum chamber due to the spacing between the ring electrodes can be mitigated by decreasing the spacing between the electrodes and the RF strips on the inner lining.

Eventually, the CIDGC could be scaled up to be installed following the beam stopping facility to provide cleaner stopped beams to precision areas like LEBIT and BECOLA. With the FRIB online, sensitive experiments will need contaminants removed from the beam and molecular ions converted back to their atomic species. For mass measurements, this will reduce the need to clean out contaminants in future experiments.

Chapter 5

Summary and Outlook

The first direct mass measurement of ^{24}Si was performed at the LEBIT facility, using PTMS. This measurement agreed with the value reported in the AME2020 [8] and the mass uncertainty was reduced by a factor of 5. The improved mass value constrains the $^{23}\mathrm{Al}(p,\gamma)$ reaction and no longer contributes to the reaction rate uncertainty. This work also informs computational modeling for Type-1 X-ray burst simulations. The ^{24}Si mass measurement also completes the latest isobar quintet at $A = 22$, where ^{24}Si has an isospin projection $T_z = -2$. Measurements like this are critical for both areas of nuclear astrophysics and nuclear structure.

This measurement also highlighted that high-precision mass measurements are subject to large concentrations of contaminants from the beam stopping facility. At best this requires additional time to prepare the beam before a successful measurement can be performed. At worst it could cause an experiment to fail. This challenge motivated the development of a gas catcher that is dedicated to performing CID. CID uses the kinetic energy of incoming molecular ions and contaminants and converts it to internal energy to dissociate the molecules. This project is of interest for several facilities around the world, including FRIB. The CIDGC prototype uses a Si_3N_4 membrane as both a gas barrier and CID mechanism. The ions are then transported across the cell using a ring electrode system to the other side where an RF carpet is located. The RF carpet then transports ions to the extraction orifice

and guided through RFQs. The ions are then injected into an RGA for identification.

Simulations have been performed to understand ion transport in the CIDGC. The information computed by SRIM, such as stopping efficiencies and final 3D positions, was used to inform how the ions transport in the main gas cell in SIMION. The transport and injection are then modeled using SIMION to understand the impact of the diffusion diaphragm diameter. The RF carpet was characterized using a potassium ion source and subsequently identified in the RGA. During online measurements, injection into the gas cell and extraction with ion surfing was observed. The ion current was successfully transported through the RFQ ion guides and ionized residual gases were observed in the RGA spectrum. However, there was no signature of the ions delivered from the beam stopping area observed and future characterizations will be needed to understand the full capabilities of such a device in an online setting.

BIBLIOGRAPHY

BIBLIOGRAPHY

[1] C. Wolf, C. Langer, F. Montes, J. Pereira, W.-J. Ong, T. Poxon-Pearson, S. Ahn, S. Ayoub, T. Baumann, D. Bazin, P. C. Bender, B. A. Brown, J. Browne, H. Crawford, R. H. Cyburt, E. Deleeuw, B. Elman, S. Fiebiger, A. Gade, P. Gastis, S. Lipschutz, B. Longfellow, Z. Meisel, F. M. Nunes, G. Perdikakis, R. Reifarth, W. A. Richter, H. Schatz, K. Schmidt, J. Schmitt, C. Sullivan, R. Titus, D. Weisshaar, P. J. Woods, J. C. Zamora, and R. G. T. Zegers. Constraining the neutron star compactness: Extraction of the $^{23}\mathrm{Al}(p,\gamma)$ reaction rate for the *rp* process. *Phys. Rev. Lett.*, 122:232701, Jun 2019.

[2] B. A. Brown and W. D. M. Rae. The Shell-Model Code NuShellX@MSU. *Nuclear Data Sheets*, 120:115–118, Jun 2014.

[3] J. Henderson and S. R. Stroberg. Examination of the inversion of isobaric analogue states in mirror nuclei. *Phys. Rev. C*, 102:031303, Sep 2020.

[4] D. Puentes, Z. Meisel, G. Bollen, A. Hamaker, C. Langer, E. Leistenschneider, C. Nicoloff, W.-J. Ong, M. Redshaw, R. Ringle, C. S. Sumithrarachchi, J. Surbrook, A. A. Valverde, and I. T. Yandow. High-precision mass measurement of ^{24}Si and a refined determination of the *rp* process at the $A = 22$ waiting point. *Phys. Rev. C*, 106:L012801, Jul 2022.

[5] Roberto Fernández-Maestre, Charles Steve Harden, Robert Gordon Ewing, Christina Lynn Crawford, and Herbert Henderson Hill. Chemical standards in ion mobility spectrometry. *The Analyst*, 135(6):1433, 2010.

[6] Larry A. Viehland. Zero-field mobilities in helium: highly accurate values for use in ion mobility spectrometry. *International Journal for Ion Mobility Spectrometry*, 15(1):21–29, Mar 2012.

[7] Larry A. Viehland, Tamar Skaist, Chetana Adhikari, and William F. Siems. Accurate zero-field mobilities of atomic ions in the rare gases for calibration of ion mobility spectrometers. *International Journal for Ion Mobility Spectrometry*, 20(1):1–9, Jun 2017.

[8] W.J. Huang, Meng Wang, F.G. Kondev, G. Audi, and S. Naimi. The AME 2020 atomic mass evaluation (I). evaluation of input data, and adjustment procedures. *Chinese Physics C*, 45(3):030002, Mar 2021.

[9] Ryan Ringle, Stefan Schwarz, and Georg Bollen. Penning trap mass spectrometry of rare isotopes produced via projectile fragmentation at the LEBIT facility. *Inter-*

national Journal of Mass Spectrometry, 349-350:87–93, Sep 2013. 100 years of Mass Spectrometry.

[10] A. A. Valverde, G. Bollen, K. Cooper, M. Eibach, K. Gulyuz, C. Izzo, D. J. Morrissey, R. Ringle, R. Sandler, S. Schwarz, C. S. Sumithrarachchi, and A. C. C. Villari. Penning trap mass measurement of ^{72}Br. *Phys. Rev. C*, 91:037301, Mar 2015.

[11] A. A. Valverde, G. Bollen, M. Brodeur, R. A. Bryce, K. Cooper, M. Eibach, K. Gulyuz, C. Izzo, D. J. Morrissey, M. Redshaw, R. Ringle, R. Sandler, S. Schwarz, C. S. Sumithrarachchi, and A. C. C. Villari. First Direct Determination of the Superallowed β-Decay Q_{EC} Value for ^{14}O. *Phys. Rev. Lett.*, 114:232502, Jun 2015.

[12] M. Eibach, G. Bollen, M. Brodeur, K. Cooper, K. Gulyuz, C. Izzo, D. J. Morrissey, M. Redshaw, R. Ringle, R. Sandler, S. Schwarz, C. S. Sumithrarachchi, A. A. Valverde, and A. C. C. Villari. Determination of the Q_{ec} values of the $T = 1/2$ mirror nuclei ^{21}Na and ^{29}P at LEBIT. *Phys. Rev. C*, 92:045502, Oct 2015.

[13] K. Gulyuz, G. Bollen, M. Brodeur, R. A. Bryce, K. Cooper, M. Eibach, C. Izzo, E. Kwan, K. Manukyan, D. J. Morrissey, O. Naviliat-Cuncic, M. Redshaw, R. Ringle, R. Sandler, S. Schwarz, C. S. Sumithrarachchi, A. A. Valverde, and A. C. C. Villari. High Precision Determination of the β Decay Q_{EC} Value of ^{11}C and Implications on the Tests of the Standard Model. *Phys. Rev. Lett.*, 116:012501, Jan 2016.

[14] C. Izzo, G. Bollen, M. Brodeur, M. Eibach, K. Gulyuz, J. D. Holt, J. M. Kelly, M. Redshaw, R. Ringle, R. Sandler, S. Schwarz, S. R. Stroberg, C. S. Sumithrarachchi, A. A. Valverde, and A. C. C. Villari. Precision mass measurements of neutron-rich Co isotopes beyond $N = 40$. *Phys. Rev. C*, 97:014309, Jan 2018.

[15] A. A. Valverde, M. Brodeur, G. Bollen, M. Eibach, K. Gulyuz, A. Hamaker, C. Izzo, W.-J. Ong, D. Puentes, M. Redshaw, R. Ringle, R. Sandler, S. Schwarz, C. S. Sumithrarachchi, J. Surbrook, A. C. C. Villari, and I. T. Yandow. High-Precision Mass Measurement of ^{56}Cu and the Redirection of the *rp*-Process Flow. *Phys. Rev. Lett.*, 120:032701, Jan 2018.

[16] W.-J. Ong, A. A. Valverde, M. Brodeur, G. Bollen, M. Eibach, K. Gulyuz, A. Hamaker, C. Izzo, D. Puentes, M. Redshaw, R. Ringle, R. Sandler, S. Schwarz, C. S. Sumithrarachchi, J. Surbrook, A. C. C. Villari, and I. T. Yandow. Mass measurement of ^{51}Fe for the determination of the $^{51}\mathrm{Fe}(p,\gamma)^{52}$Co reaction rate. *Phys. Rev. C*, 98:065803, Dec 2018.

[17] D. Puentes, G. Bollen, M. Brodeur, M. Eibach, K. Gulyuz, A. Hamaker, C. Izzo, S. M. Lenzi, M. MacCormick, M. Redshaw, R. Ringle, R. Sandler, S. Schwarz, P. Schury, N. A. Smirnova, J. Surbrook, A. A. Valverde, A. C. C. Villari, and I. T. Yandow. High-precision mass measurements of the isomeric and ground states of ^{44}V: Improving

constraints on the isobaric multiplet mass equation parameters of the $A = 44$, 0^+ quintet. *Phys. Rev. C*, 101:064309, Jun 2020.

[18] E. Leistenschneider, E. Dunling, G. Bollen, B. A. Brown, J. Dilling, A. Hamaker, J. D. Holt, A. Jacobs, A. A. Kwiatkowski, T. Miyagi, W. S. Porter, D. Puentes, M. Redshaw, M. P. Reiter, R. Ringle, R. Sandler, C. S. Sumithrarachchi, A. A. Valverde, and I. T. Yandow. Precision Mass Measurements of Neutron-Rich Scandium Isotopes Refine the Evolution of $N = 32$ and $N = 34$ Shell Closures. *Phys. Rev. Lett.*, 126:042501, Jan 2021.

[19] J. Surbrook, G. Bollen, M. Brodeur, A. Hamaker, D. Pérez-Loureiro, D. Puentes, C. Nicoloff, M. Redshaw, R. Ringle, S. Schwarz, C. S. Sumithrarachchi, L. J. Sun, A. A. Valverde, A. C. C. Villari, C. Wrede, and I. T. Yandow. First penning trap mass measurement of ^{36}Ca. *Phys. Rev. C*, 103:014323, Jan 2021.

[20] A. Hamaker, E. Leistenschneider, R. Jain, G. Bollen, S. A. Giuliani, K. Lund, W. Nazarewicz, L. Neufcourt, C. R. Nicoloff, D. Puentes, R. Ringle, C. S. Sumithrarachchi, and I. T. Yandow. Precision mass measurement of lightweight self-conjugate nucleus ^{80}Zr. *Nature Physics*, 17(12):1408–1412, Dec 2021.

[21] Z. Meisel, A. Hamaker, G. Bollen, B. A. Brown, M. Eibach, K. Gulyuz, C. Izzo, C. Langer, F. Montes, W.-J Ong, D. Puentes, M. Redshaw, R. Ringle, R. Sandler, H. Schatz, S. Schwarz, C. S. Sumithrarachchi, A. A. Valverde, and I. T. Yandow. Improved nuclear physics near $a = 61$ refines urca neutrino luminosities in accreted neutron star crusts. *Phys. Rev. C*, 105:025804, Feb 2022.

[22] W. S. Porter, E. Dunling, E. Leistenschneider, J. Bergmann, G. Bollen, T. Dickel, K. A. Dietrich, A. Hamaker, Z. Hockenbery, C. Izzo, A. Jacobs, A. Javaji, B. Kootte, Y. Lan, I. Miskun, I. Mukul, T. Murböck, S. F. Paul, W. R. Plaß, D. Puentes, M. Redshaw, M. P. Reiter, R. Ringle, J. Ringuette, R. Sandler, C. Scheidenberger, R. Silwal, R. Simpson, C. S. Sumithrarachchi, A. Teigelhöfer, A. A. Valverde, R. Weil, I. T. Yandow, J. Dilling, and A. A. Kwiatkowski. Investigating nuclear structure near $N = 32$ and $N = 34$: Precision mass measurements of neutron-rich Ca, Ti, and V isotopes. *Phys. Rev. C*, 106:024312, Aug 2022.

[23] M. König, G. Bollen, H.-J. Kluge, T. Otto, and J. Szerypo. Quadrupole excitation of stored ion motion at the true cyclotron frequency. *International Journal of Mass Spectrometry and Ion Processes*, 142(1):95–116, Mar 1995.

[24] R. H. Cyburt, A. M. Amthor, A. Heger, E. Johnson, L. Keek, Z. Meisel, H. Schatz, and K. Smith. Dependence of X-ray burst models on nuclear reaction rates. *The Astrophysical Journal*, 830(2):55, Oct 2016.

[25] Martin Kretzschmar. The ramsey method in high-precision mass spectrometry with penning traps: Theoretical foundations. *International Journal of Mass Spectrometry*, 264(2):122–145, Jul 2007.

[26] G. R. Burleson, G. S. Blanpied, G. H. Daw, A. J. Viescas, C. L. Morris, H. A. Thiessen, S. J. Greene, W. J. Braithwaite, W. B. Cottingame, D. B. Holtkamp, I. B. Moore, and C. F. Moore. Isospin quintets in the $1p$ and $s-d$ shells. *Phys. Rev. C*, 22:1180–1183, Sep 1980.

[27] R. E. Tribble, D. M. Tanner, and A. F. Zeller. Mass of ^{24}Si. *Phys. Rev. C*, 22:17–20, Jul 1980.

[28] C. Iliadis, R. Longland, A. E. Champagne, A. Coc, and R. Fitzgerald. Charged-particle thermonuclear reaction rates: II. Tables and graphs of reaction rates and probability density functions. *Nuclear Physics A*, 841(1):31–250, 2010. The 2010 Evaluation of Monte Carlo based Thermonuclear Reaction Rates.

[29] J. S. Randhawa, Y. Ayyad, W. Mittig, Z. Meisel, T. Ahn, S. Aguilar, H. Alvarez-Pol, D. W. Bardayan, D. Bazin, S. Beceiro-Novo, D. Blankstein, L. Carpenter, M. Cortesi, D. Cortina-Gil, P. Gastis, M. Hall, S. Henderson, J. J. Kolata, T. Mijatovic, F. Ndayisabye, P. O'Malley, J. Pereira, A. Pierre, H. Robert, C. Santamaria, H. Schatz, J. Smith, N. Watwood, and J. C. Zamora. First direct measurement of $^{22}\mathrm{Mg}(\alpha,p)^{25}\mathrm{Al}$ and implications for X-ray burst model-observation comparisons. *Phys. Rev. Lett.*, 125:202701, Nov 2020.

[30] Chirashree Lahiri and G. Gangopadhyay. Importance of Q-values in astrophysical rapid proton capture process. *Modern Physics Letters A*, 28(17):1350076, 2013.

[31] E. Margaret Burbidge, G. R. Burbidge, William A. Fowler, and F. Hoyle. Synthesis of the elements in stars. *Rev. Mod. Phys.*, 29:547–650, Oct 1957.

[32] Wolfgang Hillebrandt. The rapid neutron-capture process and the synthesis of heavy and neutron-rich elements. *Space Science Reviews*, 21(6):639–702, Apr 1978.

[33] C. Fröhlich, G. Martínez-Pinedo, M. Liebendörfer, F.-K. Thielemann, E. Bravo, W. R. Hix, K. Langanke, and N. T. Zinner. Neutrino-Induced Nucleosynthesis of $A > 64$ Nuclei: The νp Process. *Phys. Rev. Lett.*, 96:142502, Apr 2006.

[34] H. Schatz. The importance of nuclear masses in the astrophysical rp-process. *International Journal of Mass Spectrometry*, 251(2):293–299, 2006. ULTRA-ACCURATE MASS SPECTROMETRY AND RELATED TOPICS Dedicated to H.-J. Kluge on the occasion of his 65th birthday anniversary.

[35] Iliadis Christian. *Nuclear Physics of Stars, 2nd, Revised and Enlarged Edition*. John Wiley & Sons Incorporated, June 2015.

[36] H. Schatz and W. J. Ong. Dependence of X-Ray Burst Models on Nuclear Masses. *The Astrophysical Journal*, 844(2):139, August 2017.

[37] P. Sarriguren, R. Álvarez-Rodrıguez, and E. Moya de Guerra. Half-lives of rp-process waiting point nuclei. *The European Physical Journal A - Hadrons and Nuclei*, 24(2):193–198, May 2005.

[38] M. Saxena, W. -J Ong, Z. Meisel, D.E.M. Hoff, N. Smirnova, P.C. Bender, S.P. Burcher, M.P. Carpenter, J.J. Carroll, A. Chester, C.J. Chiara, R. Conaway, P.A. Copp, B.P. Crider, J. Derkin, A. Estradé, G. Hamad, J.T. Harke, R. Jain, H. Jayatissa, S.N. Liddick, B. Longfellow, M. Mogannam, F. Montes, N. Nepal, T.H. Ogunbeku, A.L. Richard, H. Schatz, D. Soltesz, S.K. Subedi, I. Sultana, A.S. Tamashiro, V. Tripathi, Y. Xiao, and R. Zink. ^{57}Zn β-delayed proton emission establishes the ^{56}Ni rp-process waiting point bypass. *Physics Letters B*, 829:137059, 2022.

[39] D. Rodríguez, V. S. Kolhinen, G. Audi, J. Äystö, D. Beck, K. Blaum, G. Bollen, F. Herfurth, A. Jokinen, A. Kellerbauer, H. J. Kluge, M. Oinonen, H. Schatz, E. Sauvan, and S. Schwarz. Mass measurement on the *rp*-process waiting point ^{72}Kr. *Phys. Rev. Lett.*, 93:161104, Oct 2004.

[40] A. Jungclaus, L. Cáceres, M. Górska, M. Pfützner, S. Pietri, E. Werner-Malento, H. Grawe, K. Langanke, G. Martínez-Pinedo, F. Nowacki, A. Poves, J. J. Cuenca-García, D. Rudolph, Z. Podolyak, P. H. Regan, P. Detistov, S. Lalkovski, V. Modamio, J. Walker, P. Bednarczyk, P. Doornenbal, H. Geissel, J. Gerl, J. Grebosz, I. Kojouharov, N. Kurz, W. Prokopowicz, H. Schaffner, H. J. Wollersheim, K. Andgren, J. Benlliure, G. Benzoni, A. M. Bruce, E. Casarejos, B. Cederwall, F. C. L. Crespi, B. Hadinia, M. Hellström, R. Hoischen, G. Ilie, J. Jolie, A. Khaplanov, M. Kmiecik, R. Kumar, A. Maj, S. Mandal, F. Montes, S. Myalski, G. S. Simpson, S. J. Steer, S. Tashenov, and O. Wieland. Observation of isomeric decays in the *r*-process waiting-point nucleus ^{130}Cd$_{82}$. *Phys. Rev. Lett.*, 99:132501, Sep 2007.

[41] A. Parikh, J. José, G. Sala, and C. Iliadis. Nucleosynthesis in type I X-ray bursts. *Progress in Particle and Nuclear Physics*, 69:225–253, 2013.

[42] H. Schatz, S. Gupta, P. Möller, M. Beard, E. F. Brown, A. T. Deibel, L. R. Gasques, W. R. Hix, L. Keek, R. Lau, A. W. Steiner, and M. Wiescher. Strong neutrino cooling by cycles of electron capture and β^- decay in neutron star crusts. *Nature*, 505(7481):62–65, Jan 2014.

[43] K. Minamisono, P.F. Mantica, A. Klose, S. Vinnikova, A. Schneider, B. Johnson, and B.R. Barquest. Commissioning of the collinear laser spectroscopy system in the BECOLA facility at NSCL. *Nuclear Instruments and Methods in Physics Research Section A: Accelerators, Spectrometers, Detectors and Associated Equipment*, 709:85–94, 2013.

[44] A Lapierre, G Bollen, J R Crespo Lopez-Urrutia, M Doleans, S Geyer, O Kester, K Kittimanapun, M Portillo, and S Schwarz. The MSU EBIT at NSCL. *Journal of Instrumentation*, 5(07):c07001, jul 2010.

[45] K. Cooper, C.S. Sumithrarachchi, D.J. Morrissey, A. Levand, J.A. Rodriguez, G. Savard, S. Schwarz, and B. Zabransky. Extraction of thermalized projectile fragments from a large volume gas cell. *Nuclear Instruments and Methods in Physics Research Section A: Accelerators, Spectrometers, Detectors and Associated Equipment*, 763:543–546, 2014.

[46] C. S. Sumithrarachchi, D. J. Morrissey, S. Schwarz, K. Lund, G. Bollen, R. Ringle, G. Savard, and A. C. C. Villari. Beam thermalization in a large gas catcher. *Nuclear Instruments and Methods in Physics Research Section B: Beam Interactions with Materials and Atoms*, 463:305–309, Jan 2020.

[47] K.R. Lund, G. Bollen, D. Lawton, D.J. Morrissey, J. Ottarson, R. Ringle, S. Schwarz, C.S. Sumithrarachchi, A.C.C. Villari, and J. Yurkon. Online tests of the advanced cryogenic gas stopper at nscl. *Nuclear Instruments and Methods in Physics Research Section B: Beam Interactions with Materials and Atoms*, 463:378–381, 2020.

[48] A. C. C. Villari, B. Arend, G. Bollen, D. B. Crisp, K. D. Davidson, K. Fukushima, A. I. Henriques, K. Holland, S. H. Kim, A. Lapierre, T. Maruta, D. G. Morris, D. J. Morrissey, S. Nash, P. N. Ostroumov, A. S. Plastun, J. Priller, B. M. Sherrill, M. Steiner, R. Walker, T. Zhang, and Q. Zhao. ReAccelerator Upgrade, Commissioning and First Experiments at the National Superconducting Cyclotron Laboratory (NSCL) / Facility for Rare Isotope Beams (FRIB). In *Proc. 13th International Particle Accelerator Conference (IPAC'22)*, number 13 in International Particle Accelerator Conference, pages 101–103. JACoW Publishing, Geneva, Switzerland, July 2022.

[49] J. Mitchell Wells and Scott A. McLuckey. Collision-Induced Dissociation (CID) of Peptides and Proteins. In *Biological Mass Spectrometry*, volume 402 of *Methods in Enzymology*, pages 148–185. Academic Press, 2005.

[50] Lekha Sleno and Dietrich A. Volmer. Ion activation methods for tandem mass spectrometry. *Journal of Mass Spectrometry*, 39(10):1091–1112, 2004.

[51] Christopher John Izzo. *Mass Measurements of Neutron-Rich Cobalt Isotopes beyond N= 40 and the Development of a Single Ion Penning Trap Mass Spectrometer for Rare Isotopes*. Michigan State University, 2018.

[52] P. Schury, G. Bollen, M. Block, D. J. Morrissey, R. Ringle, A. Prinke, J. Savory, S. Schwarz, and T. Sun. Beam purification techniques for low energy rare isotope beams from a gas cell. *Hyperfine Interactions*, 173(1):165–170, Nov 2006.

[53] Manuel Vogel. A Bit of History and Context. In *Particle Confinement in Penning Traps: An Introduction*, pages 1–8. Springer International Publishing, Cham, 2018.

[54] G. Gabrielse, L. Haarsma, and S.L. Rolston. Open-endcap Penning traps for high precision experiments. *International Journal of Mass Spectrometry and Ion Processes*, 88(2):319–332, 1989.

[55] M Kretzschmar. Particle motion in a Penning trap. *European Journal of Physics*, 12(5):240, Sep 1991.

[56] G. Bollen, R. B. Moore, G. Savard, and H. Stolzenberg. The accuracy of heavy-ion mass measurements using time of flight-ion cyclotron resonance in a Penning trap. *Journal of Applied Physics*, 68(9):4355–4374, Jul 1990.

[57] Lowell S. Brown and Gerald Gabrielse. Geonium theory: Physics of a single electron or ion in a Penning trap. *Rev. Mod. Phys.*, 58:233–311, Jan 1986.

[58] G Bollen, S Becker, H.-J Kluge, M König, R.B Moore, T Otto, H Raimbault-Hartmann, G Savard, L Schweikhard, and H Stolzenberg. ISOLTRAP: a tandem Penning trap system for accurate on-line mass determination of short-lived isotopes. *Nuclear Instruments and Methods in Physics Research Section A: Accelerators, Spectrometers, Detectors and Associated Equipment*, 368(3):675–697, 1996.

[59] R. Ringle, G. Bollen, A. Prinke, J. Savory, P. Schury, S. Schwarz, and T. Sun. The LEBIT 9.4T Penning trap mass spectrometer. *Nuclear Instruments and Methods in Physics Research Section A: Accelerators, Spectrometers, Detectors and Associated Equipment*, 604(3):536–547, Jun 2009.

[60] Alan G. Marshall, Christopher L. Hendrickson, and George S. Jackson. Fourier transform ion cyclotron resonance mass spectrometry: A primer. *Mass Spectrometry Reviews*, 17(1):1–35, 1998.

[61] S. Eliseev, K. Blaum, M. Block, C. Droese, M. Goncharov, E. Minaya Ramirez, D. A. Nesterenko, Yu. N. Novikov, and L. Schweikhard. Phase-imaging ion-cyclotron-resonance measurements for short-lived nuclides. *Phys. Rev. Lett.*, 110:082501, Feb 2013.

[62] P. Duhamel and M. Vetterli. Fast fourier transforms: A tutorial review and a state of the art. *Signal Processing*, 19(4):259–299, 1990.

[63] Alec Hamaker, Georg Bollen, Martin Eibach, Christopher Izzo, Daniel Puentes, Matthew Redshaw, Ryan Ringle, Rachel Sandler, Stefan Schwarz, and Isaac Yandow. SIPT - An ultrasensitive mass spectrometer for rare isotopes. *Hyperfine Interactions*, 240(1):34, Apr 2019.

[64] Klaus Blaum. High-accuracy mass spectrometry with stored ions. *Physics Reports*, 425(1):1–78, 2006.

[65] R. Ringle, G. Bollen, A. Prinke, J. Savory, P. Schury, S. Schwarz, and T. Sun. A "Lorentz" steerer for ion injection into a Penning trap. *International Journal of Mass Spectrometry*, 263(1):38–44, May 2007.

[66] A. Gade and B. M. Sherrill. NSCL and FRIB at Michigan State University: Nuclear science at the limits of stability. *Physica Scripta*, 91(5):053003, apr 2016.

[67] G. Machicoane, D. Cole, J. Ottarson, J. Stetson, and P. Zavodszky. ARTEMIS-B: A room-temperature test electron cyclotron resonance ion source for the National Superconducting Cyclotron Laboratory at Michigan State University. *Review of Scientific Instruments*, 77(3):03A322, 2006.

[68] P. A. Závodszky, B. Arend, D. Cole, J. DeKamp, M. Doleans, G. Machicoane, F. Marti, P. Miller, J. Moskalik, W. Nurnberger, J. Ottarson, J. Vincent, X. Wu, and A. Zeller. Design, construction, and first commissioning results of superconducting source for ions at NSCL/MSU. *Review of Scientific Instruments*, 79(2):02A302, 2008.

[69] D. J. Morrissey, B. M. Sherrill, M. Steiner, A. Stolz, and I. Wiedenhoever. Commissioning the A1900 projectile fragment separator. *Nuclear Instruments and Methods in Physics Research Section B: Beam Interactions with Materials and Atoms*, 204:90–96, May 2003. 14th International Conference on Electromagnetic Isotope Separators and Techniques Related to their Applications.

[70] C. Izzo, G. Bollen, S. Bustabad, M. Eibach, K. Gulyuz, D.J. Morrissey, M. Redshaw, R. Ringle, R. Sandler, S. Schwarz, and A.A. Valverde. A laser ablation source for offline ion production at LEBIT. *Nuclear Instruments and Methods in Physics Research Section B: Beam Interactions with Materials and Atoms*, 376:60–63, 2016. Proceedings of the XVIIth International Conference on Electromagnetic Isotope Separators and Related Topics (EMIS2015), Grand Rapids, MI, U.S.A., 11-15 May 2015.

[71] S. Schwarz, G. Bollen, R. Ringle, J. Savory, and P. Schury. The LEBIT ion cooler and buncher. *Nuclear Instruments and Methods in Physics Research Section A: Accelerators, Spectrometers, Detectors and Associated Equipment*, 816:131–141, Apr 2016.

[72] Walter H. G. Lewin, Jan Van Paradijs, and Ronald E. Taam. X-ray bursts. *Space Science Reviews*, 62(3):223–389, Sep 1993.

[73] H. Schatz, A. Aprahamian, J. Görres, M. Wiescher, T. Rauscher, J.F. Rembges, F.-K. Thielemann, B. Pfeiffer, P. Möller, K.-L. Kratz, H. Herndl, B.A. Brown, and H. Rebel. rp-process nucleosynthesis at extreme temperature and density conditions. *Physics Reports*, 294(4):167–263, Feb 1998.

[74] R. K. Wallace and Stanley E. Woosley. Explosive hydrogen burning. *The Astrophysical Journal Supplement Series*, 45:389–420, Feb 1981.

[75] M. van der Klis and Walter H. G. Lewin. *Compact Stellar X-ray Sources.* Number Vol. 39 in Cambridge Astrophysics Series. Cambridge University Press, 2006.

[76] Peter Bult, Diego Altamirano, Zaven Arzoumanian, Anna V. Bilous, Deepto Chakrabarty, Keith C. Gendreau, Tolga Güver, Gaurava K. Jaisawal, Erik Kuulkers, Christian Malacaria, Mason Ng, Andrea Sanna, and Tod E. Strohmayer. The X-ray bursts of XTE J1739–285: A NICER sample. *The Astrophysical Journal*, 907(2):79, Feb 2021.

[77] Nevin N. Weinberg, Lars Bildsten, and Hendrik Schatz. Exposing the nuclear burning ashes of radius expansion type I X-ray bursts. *The Astrophysical Journal*, 639(2):1018–1032, mar 2006.

[78] Zach Meisel, Alex Deibel, Laurens Keek, Peter Shternin, and Justin Elfritz. Nuclear physics of the outer layers of accreting neutron stars. *Journal of Physics G: Nuclear and Particle Physics*, 45(9):093001, Jul 2018.

[79] H. Schatz, A. Aprahamian, V. Barnard, L. Bildsten, A. Cumming, M. Ouellette, T. Rauscher, F.-K. Thielemann, and M. Wiescher. End point of the *rp* process on accreting neutron stars. *Phys. Rev. Lett.*, 86:3471–3474, Apr 2001.

[80] Alexander Heger, Andrew Cumming, Duncan K. Galloway, and Stanford E. Woosley. Models of type I X-ray bursts from GS 1826-24: A probe of rp-process hydrogen burning. *The Astrophysical Journal*, 671(2):L141–L144, Nov 2007.

[81] Michael Zamfir, Andrew Cumming, and Duncan K. Galloway. Contraints on neutron star mass and radius in GS 1826–24 from sub-eddington X-ray bursts. *The Astrophysical Journal*, 749(1):69, Mar 2012.

[82] Anuj Parikh, Jordi José, Fermín Moreno, and Christian Iliadis. The effects of variations in nuclear processes on type I X-ray burst nucleosynthesis. *The Astrophysical Journal Supplement Series*, 178(1):110–136, Sep 2008.

[83] Zach Meisel, Grant Merz, and Sophia Medvid. Influence of nuclear reaction rate uncertainties on neutron star properties extracted from X-ray burst model–observation comparisons. *The Astrophysical Journal*, 872(1):84, Feb 2019.

[84] Zach Meisel. Consistent modeling of GS 1826-24 X-ray bursts for multiple accretion rates demonstrates the possibility of constraining rp-process reaction rates. *The Astrophysical Journal*, 860(2):147, Jun 2018.

[85] Jacob Lund Fisker, Friedrich-Karl Thielemann, and Michael Wiescher. The nuclear reaction waiting points: ^{22}Mg, ^{26}Si, ^{30}S, and ^{34}Ar and bolometrically double-peaked type I X-ray bursts. *The Astrophysical Journal*, 608(1):L61–L64, May 2004.

[86] L. Van Wormer, J. Görres, C. Iliadis, M. Wiescher, and F. K. Thielemann. Reaction rates and reaction sequences in the rp-process. *The Astrophysical Journal*, 432:326, Sep 1994.

[87] H. Schatz, J. Görres, H. Herndl, N. I. Kaloskamis, E. Stech, P. Tischhauser, M. Wiescher, A. Bacher, G. P. A. Berg, T. C. Black, S. Choi, C. C. Foster, K. Jiang, and E. J. Stephenson. First measurement of excited states in the very proton rich nucleus ^{24}Si and the consequences for ^{22}Na nucleosynthesis in novae. *Phys. Rev. Lett.*, 79:3845–3848, Nov 1997.

[88] K. Yoneda, A. Obertelli, A. Gade, D. Bazin, B. A. Brown, C. M. Campbell, J. M. Cook, P. D. Cottle, A. D. Davies, D.-C. Dinca, T. Glasmacher, P. G. Hansen, T. Hoagland, K. W. Kemper, J.-L. Lecouey, W. F. Mueller, R. R. Reynolds, B. T. Roeder, J. R. Terry, J. A. Tostevin, and H. Zwahlen. Two-neutron knockout from neutron-deficient ^{34}Ar, ^{30}S, and ^{26}Si. *Phys. Rev. C*, 74:021303, Aug 2006.

[89] Raymond T. Birge. The Calculation of Errors by the Method of Least Squares. *Phys. Rev.*, 40:207–227, Apr 1932.

[90] K. Gulyuz, J. Ariche, G. Bollen, S. Bustabad, M. Eibach, C. Izzo, S. J. Novario, M. Redshaw, R. Ringle, R. Sandler, S. Schwarz, and A. A. Valverde. Determination of the direct double-β-decay Q value of ^{96}Zr and atomic masses of $^{90-92,94,96}$Zr and $^{92,94-98,100}$Mo. *Phys. Rev. C*, 91:055501, May 2015.

[91] R. Ringle, T. Sun, G. Bollen, D. Davies, M. Facina, J. Huikari, E. Kwan, D. J. Morrissey, A. Prinke, J. Savory, P. Schury, S. Schwarz, and C. S. Sumithrarachchi. High-precision Penning trap mass measurements of ^{37,38}Ca and their contributions to conserved vector current and isobaric mass multiplet equation. *Phys. Rev. C*, 75:055503, May 2007.

[92] William A. Fowler, Georgeanne R. Caughlan, and Barbara A. Zimmerman. Thermonuclear Reaction Rates. *Annual Review of Astronomy and Astrophysics*, 5:525, Jan 1967.

[93] B. Longfellow, A. Gade, J. A. Tostevin, E. C. Simpson, B. A. Brown, A. Magilligan, D. Bazin, P. C. Bender, M. Bowry, B. Elman, E. Lunderberg, D. Rhodes, M. Spieker, D. Weisshaar, and S. J. Williams. Two-neutron knockout as a probe of the composition of states in ^{22}Mg, ^{23}Al, and ^{24}Si. *Phys. Rev. C*, 101:031303, Mar 2020.

[94] J. Humblet, W. A. Fowler, and B. A. Zimmerman. Approximate penetration factors for nuclear reactions of astrophysical interest. *Astronomy and Astrophysics*, 177(1-2):317–325, May 1987.

[95] R. Longland, C. Iliadis, A.E. Champagne, J.R. Newton, C. Ugalde, A. Coc, and R. Fitzgerald. Charged-particle thermonuclear reaction rates: I. Monte Carlo method and statistical distributions. *Nuclear Physics A*, 841(1):1–30, Oct 2010. The 2010 Evaluation of Monte Carlo based Thermonuclear Reaction Rates.

[96] W. A. Richter, B. A. Brown, R. Longland, C. Wrede, P. Denissenkov, C. Fry, F. Herwig, D. Kurtulgil, M. Pignatari, and R. Reifarth. Shell-model studies of the astrophysical *rp*-process reactions $^{34}\mathrm{S}(p,\gamma)^{35}\mathrm{Cl}$ and $^{34g,m}\mathrm{Cl}(p,\gamma)^{35}\mathrm{Ar}$. *Phys. Rev. C*, 102:025801, Aug 2020.

[97] A. Banu, F. Carstoiu, N. L. Achouri, W. N. Catford, M. Chartier, B. Fernández-Domínguez, M. Horoi, B. Laurent, N. A. Orr, S. Paschalis, N. Patterson, B. Pietras, B. T. Roeder, P. Roussel-Chomaz, J. S. Thomas, L. Trache, and R. E. Tribble. One-proton breakup of $^{24}\mathrm{Si}$ and the $^{23}\mathrm{Al}(p,\gamma)^{24}\mathrm{Si}$ reaction in type I X-ray bursts. *Phys. Rev. C*, 86:015806, Jul 2012.

[98] M. Shamsuzzoha Basunia. Nuclear data sheets for a = 22. *Nuclear Data Sheets*, 127:69–190, Jul–Aug 2015.

[99] Grant Merz and Zach Meisel. Urca nuclide production in Type-I X-ray bursts and implications for nuclear physics studies. *Monthly Notices of the Royal Astronomical Society*, 500(3):2958–2968, Jan 2021.

[100] E.F. Brown. *Stellar Astrophysics*. Open Astrophysics Bookshelf, 2015.

[101] Jacob Lund Fisker, Hendrik Schatz, and Friedrich-Karl Thielemann. Explosive hydrogen burning during type I X-ray bursts. *The Astrophysical Journal Supplement Series*, 174(1):261–276, Jan 2008.

[102] G. Lotay, J. Henderson, W.N. Catford, F.A. Ali, J. Berean, N. Bernier, S.S. Bhattacharjee, M. Bowry, R. Caballero-Folch, B. Davids, T.E. Drake, A.B. Garnsworthy, F. Ghazi Moradi, S.A. Gillespie, B. Greaves, G. Hackman, S. Hallam, D. Hymers, E. Kasanda, D. Levy, B.K. Luna, A. Mathews, Z. Meisel, M. Moukaddam, D. Muecher, B. Olaizola, N.A. Orr, H.P. Patel, M.M. Rajabali, Y. Saito, J. Smallcombe, M. Spencer, C.E. Svensson, K. Whitmore, and M. Williams. Single neutron transfer on $^{23}\mathrm{Ne}$ and its relevance for the pathway of nucleosynthesis in astrophysical X-ray bursts. *Physics Letters B*, 833:137361, 2022.

[103] Michiharu Wada, Yoshihisa Ishida, Takashi Nakamura, Yasunori Yamazaki, Tadashi Kambara, Hitoshi Ohyama, Yasushi Kanai, Takao M. Kojima, Youichi Nakai, Nagayasu Ohshima, Atsushi Yoshida, Toshiyuki Kubo, Yukari Matsuo, Yoshimitsu

Fukuyama, Kunihiro Okada, Tetsu Sonoda, Shunsuke Ohtani, Koji Noda, Hirokane Kawakami, and Ichiro Katayama. Slow RI-beams from projectile fragment separators. *Nuclear Instruments and Methods in Physics Research Section B: Beam Interactions with Materials and Atoms*, 204:570–581, 2003. 14th International Conference on Electromagnetic Isotope Separators and Techniques Related to their Applications.

[104] G. Savard, J. Clark, C. Boudreau, F. Buchinger, J.E. Crawford, H. Geissel, J.P. Greene, S. Gulick, A. Heinz, J.K.P. Lee, A. Levand, M. Maier, G. Münzenberg, C. Scheidenberger, D. Seweryniak, K.S. Sharma, G. Sprouse, J. Vaz, J.C. Wang, B.J. Zabransky, and Z. Zhou. Development and operation of gas catchers to thermalize fusion–evaporation and fragmentation products. *Nuclear Instruments and Methods in Physics Research Section B: Beam Interactions with Materials and Atoms*, 204:582–586, 2003. 14th International Conference on Electromagnetic Isotope Separators and Techniques Related to their Applications.

[105] J.B. Neumayr, L. Beck, D. Habs, S. Heinz, J. Szerypo, P.G. Thirolf, V. Varentsov, F. Voit, D. Ackermann, D. Beck, M. Block, Z. Di, S.A. Eliseev, H. Geissel, F. Herfurth, F.P. Heßberger, S. Hofmann, H.-J. Kluge, M. Mukherjee, G. Münzenberg, M. Petrick, W. Quint, S. Rahaman, C. Rauth, D. Rodríguez, C. Scheidenberger, G. Sikler, Z. Wang, C. Weber, W.R. Plaß, M. Breitenfeldt, A. Chaudhuri, G. Marx, L. Schweikhard, A.F. Dodonov, Y. Novikov, and M. Suhonen. The ion-catcher device for SHIPTRAP. *Nuclear Instruments and Methods in Physics Research Section B: Beam Interactions with Materials and Atoms*, 244(2):489–500, 2006.

[106] S.A. Eliseev, M. Block, A. Chaudhuri, Z. Di, D. Habs, F. Herfurth, H.-J. Kluge, J.B. Neumayr, W.R. Plaß, C. Rauth, P.G. Thirolf, G. Vorobjev, and Z. Wang. Extraction efficiency and extraction time of the SHIPTRAP gas-filled stopping cell. *Nuclear Instruments and Methods in Physics Research Section B: Beam Interactions with Materials and Atoms*, 258(2):479–484, 2007.

[107] S. Schwarz, G. Bollen, K. Lund, C. Magsig, D.J. Morrissey, J. Ottarson, C. Sumithrarachchi, and A.C.C. Villari. The NSCL cyclotron gas stopper – Preparing to go 'online'. *Nuclear Instruments and Methods in Physics Research Section B: Beam Interactions with Materials and Atoms*, 463:293–296, 2020.

[108] L. Weissman, D.J. Morrissey, G. Bollen, D.A. Davies, E. Kwan, P.A. Lofy, P. Schury, S. Schwarz, C. Sumithrarachchi, T. Sun, and R. Ringle. Conversion of 92 MeV/u ^{38}Ca/^{37}K projectile fragments into thermalized ion beams. *Nuclear Instruments and Methods in Physics Research Section A: Accelerators, Spectrometers, Detectors and Associated Equipment*, 540(2):245–258, 2005.

[109] A. Takamine, M. Wada, Y. Ishida, T. Nakamura, K. Okada, Y. Yamazaki, T. Kambara, Y. Kanai, T. M. Kojima, Y. Nakai, N. Oshima, A. Yoshida, T. Kubo, S. Ohtani, K. Noda, I. Katayama, P. Hostain, V. Varentsov, and H. Wollnik. Space-charge effects

in the catcher gas cell of a rf ion guide. *Review of Scientific Instruments*, 76(10):103503, 2005.

[110] M. Facina, G. Bollen, and D. J. Morrissey. Space charge effects on stopped projectile fragment drift in gas. *Hyperfine Interactions*, 174(1):21–26, Jan 2007.

[111] T. Porobić, M. Beck, M. Breitenfeldt, C. Couratin, P. Finlay, A. Knecht, X. Fabian, P. Friedag, X. Fléchard, E. Liénard, G. Ban, D. Zákoucký, G. Soti, S. Van Gorp, Ch. Weinheimer, E. Wursten, and N. Severijns. Space-charge effects in Penning ion traps. *Nuclear Instruments and Methods in Physics Research Section A: Accelerators, Spectrometers, Detectors and Associated Equipment*, 785:153–162, 2015.

[112] D.J. Morrissey, G. Bollen, M. Facina, and S. Schwarz. Pulsed extraction of ionization from helium buffer gas. *Nuclear Instruments and Methods in Physics Research Section B: Beam Interactions with Materials and Atoms*, 266(21):4822–4828, 2008.

[113] G. Bollen, D. Davies, M. Facina, J. Huikari, E. Kwan, P. A. Lofy, D. J. Morrissey, A. Prinke, R. Ringle, J. Savory, P. Schury, S. Schwarz, C. Sumithrarachchi, T. Sun, and L. Weissman. Experiments with Thermalized Rare Isotope Beams from Projectile Fragmentation: A Precision Mass Measurement of the Superallowed β Emitter ^{38}Ca. *Phys. Rev. Lett.*, 96:152501, Apr 2006.

[114] Verena Grill, Jianwei Shen, Chris Evans, and R. Graham Cooks. Collisions of ions with surfaces at chemically relevant energies: Instrumentation and phenomena. *Review of Scientific Instruments*, 72(8):3149–3179, 2001.

[115] Ashok R. Dongré, Árpád Somogyi, and Vicki H. Wysocki. Surface-induced Dissociation: An Effective Tool to Probe Structure, Energetics and Fragmentation Mechanisms of Protonated Peptides. *Journal of Mass Spectrometry*, 31(4):339–350, 1996.

[116] J. Jašík, J. Roithová, J. Žabka, A. Pysanenko, L. Feketeová, I. Ipolyi, T.D. Märk, and Z. Herman. Surface-induced dissociation and reactions of dications and cations: Collisions of dications $C_7H_8^{2+}$, $C_7H_7^{2+}$, and $C_7H_6^{2+}$ and a comparison with the respective cations $C_7D_8^+$ and $C_7H_7^+$. *International Journal of Mass Spectrometry*, 249-250:162–170, 2006. Chava Lifshitz Memorial Issue.

[117] Julia Laskin and Jean H. Futrell. New approach for studying slow fragmentation kinetics in FT-ICR: Surface-induced dissociation combined with resonant ejection. *International Journal of Mass Spectrometry*, 378:160–168, 2015. SI: Bierbaum 65th Birthday.

[118] Bogdan A. Budnik, Kim F. Haselmann, and Roman A. Zubarev. Electron detachment dissociation of peptide di-anions: an electron–hole recombination phenomenon. *Chemical Physics Letters*, 342(3):299–302, 2001.

[119] Roman A. Zubarev, David M. Horn, Einar K. Fridriksson, Neil L. Kelleher, Nathan A. Kruger, Mark A. Lewis, Barry K. Carpenter, and Fred W. McLafferty. Electron Capture Dissociation for Structural Characterization of Multiply Charged Protein Cations. *Analytical Chemistry*, 72(3):563–573, 2000. PMID: 10695143.

[120] Blas A. Cerda, David M. Horn, Kathrin Breuker, and Fred W. McLafferty. Sequencing of Specific Copolymer Oligomers by Electron-Capture-Dissociation Mass Spectrometry. *Journal of the American Chemical Society*, 124(31):9287–9291, 2002. PMID: 12149036.

[121] Jiong Yang and Kristina Håkansson. Characterization and optimization of electron detachment dissociation fourier transform ion cyclotron resonance mass spectrometry. *International Journal of Mass Spectrometry*, 276(2):144–148, 2008. Electron/Ion and Ion/Ion Interactions: Fundamentals, Applications, Tools and Methodologies Special Issue.

[122] Michael V Gorshkov, Christophe D Masselon, Eugene N Nikolaev, Harold R Udseth, Ljiljana Paša-Tolić, and Richard D Smith. Considerations for electron capture dissociation efficiency in FTICR mass spectrometry. *International Journal of Mass Spectrometry*, 234(1):131–136, 2004. Special Issue in Honour of Alan G. Marshall.

[123] Yulin Qi and Dietrich A. Volmer. Electron-based fragmentation methods in mass spectrometry: An overview. *Mass Spectrometry Reviews*, 36(1):4–15, 2017.

[124] Scott A. McLuckey. Principles of collisional activation in analytical mass spectrometry. *Journal of the American Society for Mass Spectrometry*, 3(6):599–614, 1992.

[125] Florian Greiner, Timo Dickel, Samuel Ayet San Andrés, Julian Bergmann, Paul Constantin, Jens Ebert, Hans Geissel, Emma Haettner, Christine Hornung, Ivan Miskun, Wayne Lippert, Israel Mardor, Iain Moore, Wolfgang R. Plaß, Sivaji Purushothaman, Ann-Kathrin Rink, Moritz P. Reiter, Christoph Scheidenberger, and Helmut Weick. Removal of molecular contamination in low-energy RIBs by the isolation-dissociation-isolation method. *Nuclear Instruments and Methods in Physics Research Section B: Beam Interactions with Materials and Atoms*, 463:324–326, 2020.

[126] A. Jacobs, C. Andreoiu, J. Bergmann, T. Brunner, T. Dickel, I. Dillmann, E. Dunling, J. Flowerdew, L. Graham, G. Gwinner, Z. Hockenbery, B. Kootte, Y. Lan, K.G. Leach, E. Leistenschneider, E.M. Lykiardopoulou, V. Monier, I. Mukul, S.F. Paul, W.R. Plaß, M.P. Reiter, C. Scheidenberger, R. Thompson, J.L. Tracy, C. Will, M.E. Wieser, M. Yavor, J. Dilling, and A.A. Kwiatkowski. Collision-Induced Dissociation at TRIUMF's Ion Trap for Atomic and Nuclear science. *International Journal of Mass Spectrometry*, 482:116931, 2022.

[127] R.A. Yost, C.G. Enke, D.C. McGilvery, D. Smith, and J.D. Morrison. High efficiency collision-induced dissociation in an RF-only quadrupole. *International Journal of Mass Spectrometry and Ion Physics*, 30(2):127–136, 1979.

[128] P. A. F. Anastasi and R. E. Burge. Preparation and Characterisation of Silicon Nitride Membranes for Soft X-Ray Microscopy. In Alan G. Michette, Graeme R. Morrison, and Chistopher J. Buckley, editors, *X-Ray Microscopy III*, pages 341–343, Berlin, Heidelberg, 1992. Springer Berlin Heidelberg.

[129] Precision Ceramics USA. Shapal Hi M Soft™ – Machinable Aluminum Nitride (AlN), URL: `https://precision-ceramics.com/materials/shapal/`, Oct 2021.

[130] G. Bollen. "Ion surfing" with radiofrequency carpets. *International Journal of Mass Spectrometry*, 299(2):131–138, 2011.

[131] Scott A. Shaffer, Keqi Tang, Gordon A. Anderson, David C. Prior, Harold R. Udseth, and Richard D. Smith. A novel ion funnel for focusing ions at elevated pressure using electrospray ionization mass spectrometry. *Rapid Communications in Mass Spectrometry*, 11(16):1813–1817, 1997.

[132] I. Katayama, M. Wada, H. Kawakami, J. Tanaka, and K. Noda. Cyclotron ion guide for energetic radioactive nuclear ions. *Hyperfine Interactions*, 115(1):165–170, Nov 1998.

[133] Raymond E. March. An Introduction to Quadrupole Ion Trap Mass Spectrometry. *Journal of Mass Spectrometry*, 32(4):351–369, 1997.

[134] James F. Ziegler and Jochen P. Biersack. The stopping and range of ions in matter. In D. Allan Bromley, editor, *Treatise on Heavy-Ion Science: Volume 6: Astrophysics, Chemistry, and Condensed Matter*, pages 93–129. Springer US, Boston, MA, 1985.

[135] James F. Ziegler, M.D. Ziegler, and J.P. Biersack. SRIM – The stopping and range of ions in matter (2010). *Nuclear Instruments and Methods in Physics Research Section B: Beam Interactions with Materials and Atoms*, 268(11):1818–1823, 2010. 19th International Conference on Ion Beam Analysis.

[136] David A Dahl. SIMION for the personal computer in reflection. *International Journal of Mass Spectrometry*, 200(1):3–25, 2000. Volume 200: The state of the field as we move into a new millenium.

[137] A.D. Appelhans and D.A. Dahl. Measurement of external ion injection and trapping efficiency in the ion trap mass spectrometer and comparison with a predictive model. *International Journal of Mass Spectrometry*, 216(3):269–284, 2002.

[138] Photonis. Channel electron multipliers, URL: `https://www.photonis.com/products/channeltron-electron-multipliers`, Sept 2021.

[139] Heatwave Labs. Alkali earths and Alkali metal, URL: `https://www.cathode.com/`, Feb 2023.

[140] G. Bollen, D.J. Morrissey, and S. Schwarz. A study of gas-stopping of intense energetic rare isotope beams. *Nuclear Instruments and Methods in Physics Research Section A: Accelerators, Spectrometers, Detectors and Associated Equipment*, 550(1):27–38, 2005.

[141] Frederic Allegrini, Robert W. Ebert, Stephen A. Fuselier, Georgios Nicolaou, Peter V. Bedworth, Steve W. Sinton, and Karlheinz J. Trattner. Charge state of ∼1 to 50 keV ions after passing through graphene and ultrathin carbon foils. *Optical Engineering*, 53(2):024101, 2014.

[142] P. Mueller, 2022. Private communication.